SOFT-SWITCHING ACTIVE-CLAMP FLYBACK MICROINVERTER FOR PV APPLICATIONS

RASEDUL HASAN

FACULTY OF ENGINEERING
UNIVERSITY OF MALAYA
KUALA LUMPUR

2017

SOFT-SWITCHING ACTIVE-CLAMP FLYBACK MICROINVERTER FOR PV APPLICATIONS

RASEDUL HASAN

DISSERTATION SUBMITTED IN FULFILMENT OF THE REQUIREMENTS FOR THE DEGREE OF MASTER OF ENGINEERING SCIENCE

FACULTY OF ENGINEERING
UNIVERSITY OF MALAYA
KUALA LUMPUR

2017

UNIVERSITY OF MALAYA

ORIGINAL LITERARY WORK DECLARATION

Name of Candidate: **Rasedul Hasan** (I.C/Passport No:

Matric No: **KGA140042**

Name of Degree: **Master of Engineering Science**

Title of Dissertation:

Soft-switching active-clamp flyback microinverter for PV applications

Field of Study: **Renewable Energy**

I do solemnly and sincerely declare that:

(1) I am the sole author/writer of this Work;
(2) This Work is original;
(3) Any use of any work in which copyright exists was done by way of fair dealing and for permitted purposes and any excerpt or extract from, or reference to or reproduction of any copyright work has been disclosed expressly and sufficiently and the title of the Work and its authorship have been acknowledged in this Work;
(4) I do not have any actual knowledge nor do I ought reasonably to know that the making of this work constitutes an infringement of any copyright work;
(5) I hereby assign all and every rights in the copyright to this Work to the University of Malaya ("UM"), who henceforth shall be owner of the copyright in this Work and that any reproduction or use in any form or by any means whatsoever is prohibited without the written consent of UM having been first had and obtained;
(6) I am fully aware that if in the course of making this Work I have infringed any copyright whether intentionally or otherwise, I may be subject to legal action or any other action as may be determined by UM.

Candidate's Signature Date:

Subscribed and solemnly declared before,

Witness's Signature Date:

Name:

Designation:

ABSTRACT

Grid-connected photovoltaic (PV) system has received a great attention due to the elimination of battery cost in distributed power generation system. The microinverter is superior to other technologies of PV converter in terms of obtaining the highest maximum power point tracking (MPPT) accuracy on each PV module. The microinverters can be classified into isolated and non-isolated type with respect to the presence of galvanic isolation. Isolated types are more preferable in terms of reliability and transferring higher quality of power to the grid. However, the efficiency of the isolated microinverters degrades due to high frequency transformer and high switching losses. Therefore, increasing the efficiency of the PV converter maintaining higher lifetime and lower cost is the most critical job to form a reliable microinverter. This study presents a single-stage and a double-stage active-clamp resonant flyback microinverter for grid-connected PV AC module system. The single-stage microinverter is operated with a hybrid operation of discontinuous conduction mode (DCM) and boundary conduction mode (BCM). The proposed modified hybrid method is based on different variable negative current references for DCM and BCM operation. Hence, the zero-voltage and zero-current switching (ZVZCS) turn-on of the high frequency main switch is achieved by allowing a negative current through the resonant circuit in both conduction modes. A small capacitor is inserted across the primary switch to achieve zero voltage switching (ZVS) turn-off operation. The energy stored in the leakage inductance of the transformer is also recycled and voltage stress of the main switch is reduced. It enables the use of lower voltage rating MOSFET and reduces the switch conduction loss. The mathematical analysis of the proposed hybrid operation modes in different resonant condition is provided for the modelling of the proposed system. The double-stage microinverter is composed of a DC-DC flyback converter with a resonant full-bridge inverter. The flyback converter contains a resonant active-clamp circuit that

limits the voltage stress and provides soft-switching operation. Therefore, the switching losses of the high frequency primary switches are negligible. A resonant full-bridge inverter with ZVS of the high frequency switches is adopted that make the overall efficiency high. Moreover, using a film capacitor in the DC link, the lifespan of the microinverter is increased. A 250W prototype of the proposed microinverter has been implemented and the peak efficiencies are found to be 97.1% and 96.5% for the single- and double-stage microinverter respectively. Hence, the proposed active-clamp flyback microinverter confirms the superiority compare to existing topologies.

ABSTRAK

Sistem penyambungan photovoltaik (PV) ke grid telah menerima perhatian yang besar disebabkan oleh penghapusan kos bateri dalam sistem penjanaan kuasa. Penyongsang mikro ini adalah yang terbaik dalam teknologi penukar PV dari segi ketepatan kebolehan mendapatkan titik pengesanan kuasa maksimum (MPPT) di setiap modul PV. Penyongsang mikro boleh dikelaskan kepada jenis dengan pengasing dan tanpa pengasing dengan penggunaan pengasing galvanik. Jenis penyongsang dengan pengasing adalah lebih lebih baik dari segi kebolehpercayaan dan memindahkan kualiti kuasa yang lebih tinggi kepada grid. Walau bagaimanapun, kecekapan penyongsang mikro ini berkurang disebabkan oleh pengubah berfrekuensi tinggi dan kehilangan semasa pensuisan yang tinggi. Oleh itu, peningkatkan kecekapan penukar PV mengekalkan jangka hayat yang lebih tinggi dan kos yang lebih rendah adalah tugas yang paling kritikal untuk membentuk penyongsang mikro yang boleh dipercayai. Kajian ini membentangkan aktif-pengapit salunan micro-penyongsang flyback satu-peringkat dan dua-peringkat untuk modul sistem PV AC grid yang berkaitan. Micro-penyongsang satu-peringkat dikendalikan dengan operasi mod hibrid pengaliran tidak berterusan (DCM) dan mod pengaliran sempadan (BCM). Kaedah hybrid yang diubahsuai dicadangkan berdasarkan kepada rujukan pembolehubah yang berbeza arus negatif untuk DCM dan operasi BCM. Oleh itu, pensuisan voltan sifar dan arus sifar (ZVZCS) saling bertukar suis utama frekuensi tinggi dicapai dengan membenarkan arus negatif melalui litar salunan dalam kedua-dua mod pengaliran. Kapasitor kecil dimasukkan ke seluruh suis utama untuk mencapai operasi pensuisan voltan sifar (ZVS) semasa keadaan tutup. Tenaga yang disimpan dalam pengubah peraruh bocoran juga dikitar semula dan tekanan voltan pensuisan utama dikurangkan. Ia membolehkan penggunaan voltan yang lebih rendah pada MOSFET dan mengurangkan kehilangan suis pengaliran. Analisis matematik mod operasi hibrid yang dicadangkan dalam

keadaan salunan yang berbeza disediakan untuk pemodelan sistem yang dicadangkan. Micro-penyongsang dua-peringkat terdiri daripada penukar flyback DC-DC dengan salunan penuh titi penyongsang. Penukar flyback mengandungi pengapit salunan litar aktif yang menghadkan tekanan voltan dan menyediakan operasi yang penukar lembut. Oleh itu, kehilangan pensuisan suis utama berfrekuensi tinggi boleh diabaikan. Salunan penuh titi penyongsang dengan pensuisan ZVS berfrekuensi tinggi diguna pakai untuk meningkatkan kecekapan keseluruhan lebih tinggi. Selain itu, dengan menggunakan kapasitor filem di rangkaian DC, jangka hayat micro-penyongsang akan bertambah. Satu prototaip 250W daripada micro-penyongsang yang dicadangkan telah dilaksanakan dan kecekapan puncak didapati masing-masing adalah 97.1% dan 96.5% untuk micro-penyongsang satu dan dua peringkat. Oleh itu, aktif-pengapit micro-penyongsang flyback yang dicadangkan mengesahkan keunggulannya berbanding dengan topologi-topologi yang sedia ada.

ACKNOWLEDGEMENTS

First and foremost, all praise to Allah, the Almighty, the greatest of all, on whom ultimately we depend for sustenance and guidance. I would like to thank Almighty Allah for giving me opportunity, determination and strength to do my research. His continuous grace and mercy was with me throughout my life and ever more during the tenure of my research. I do believe sincerely that without the help and blessing of Allah the achievement of this dissertation will not be possible.

I would like to thank and express my deep and sincere gratitude to my supervisor Prof. Dr. Saad Mekhilef for his continuous support, guidance and encouragement during my research in Power Electronics and Renewable Energy Research Laboratory (PEARL). In addition to being an excellent supervisor, he is a man of principles and has immense knowledge of research. I appreciate all his contributions of time, support and ideas. I also would like to acknowledge the Ministry of Higher Education, Malaysia and University of Malaya for providing financial support through my research period.

My sincere gratitude also goes out to all the past and present members of the Power Electronics and Renewable Energy Research Laboratory (PEARL). Special mention of appreciation goes to Md. Didarul Islam, Mohammad Aamir and Md. Tofael Ahmed for their invaluable advice and spiritual support throughout the study. I would like to thank my respected brothers Raza Moshwan and Rubel Bashar for their cordial help and encouragement throughout my staying in Malaysia.

Last but not least, I would like to dedicate this work to my sincere and generous father Abdul Bari, and my loving mother Rahima Khatun, this is my precious gift to you for all your sacrifice to give me this life. To my lovely wife for her patience, assistance, continuous support and understanding in everything I done. Also would like to dedicate to my loving son Abdullah Saad.

TABLE OF CONTENTS

LIST OF FIGURES

LIST OF TABLES

LIST OF SYMBOLS AND ABBREVIATIONS

A_c	:	Cross-sectional area of the ferrite core of flyback converter
BCM	:	Boundary conduction mode
BCMVNC	:	BCM with variable negative current
CCM	:	Continuous conduction mode
CEC		California Energy Commission
C_c	:	Clamp-capacitor of the flyback converter
C_{ca}	:	Auxiliary clamp-capacitor of the auxiliary branch of H-bridge inverter
C_{dc}	:	DC link capacitor
C_f	:	Filter capacitor
C_{oss_sm}	:	MOSFET output capacitance
C_r	:	Resonant capacitor of the single-stage flyback converter
C_{r1}	:	Resonant capacitor of the DC-DC flyback converter of double-stage microinverter
C_{r2}	:	Resonant capacitor of the auxiliary branch of H-bridge inverter
C_1-C_4	:	Small capacitors across the switches of H-bridge inverter
DCM	:	Discontinuous conduction mode
DCMVNC	:	DCM with variable negative current
D_1 & D_2	:	Rectifier diodes
D	:	Duty cycle
D_{min}	:	Minimum duty cycle
D_{max}	:	Maximum duty cycle
D_w	:	Dwell time duty ratio
E_{clamp}	:	Energy stored in the clamp-capacitor

E_{Lm}	:	Energy stored in the magnetizing inductance
i_c	:	Clamp-switch current of flyback converter
i_{D1}	:	Diode current
i_{Lm}	:	Magnetizing current
$i_{Lm\text{-}pk}$	:	Peak value of the magnetizing current
i_{Lr}	:	Resonant inductor current of the single-stage flyback converter
$i_{Lr\text{-}pk}$	:	Peak value of the resonant inductor current of the single-stage flyback converter
i_{Lr1}	:	Resonant inductor current of the DC-DC flyback converter
$i_{Lr1\text{-}pk}$	:	Peak value of the resonant inductor current of the DC-DC flyback converter
i_{Lr2}	:	Resonant inductor current of the auxiliary branch of H-bridge inverter
i_{ref} *(BCMVNC)*	:	Reference current for BCMVNC
i_{ref} *(DCMVNC)*	:	Reference current for DCMVNC
i_{Sm}	:	Main-switch current of the flyback converter
i_{Sm_pk}	:	Peak value of the primary switch current
i_{Sm_rms}	:	Root Mean Square (RMS) value of the primary switch current
i_{Sr}	:	Resonant switch current of the auxiliary branch of H-bridge inverter
i_{Ss1} & i_{Ss2}		Current through the unfolding switch
$i_{S1\text{-}S4}$	:	Switch current of H-bridge inverter
I_{PV}	:	DC current of PV module
k_{fe}	:	Constant proportionality of ferrite core
L_m	:	Magnetizing inductance
l_m		Magnetic path length of ferrite core

L_r	:	Resonant inductor of the single-stage flyback converter
L_{r1}	:	Resonant inductance of the DC-DC flyback converter
L_{r2}	:	Resonant inductor of the auxiliary branch of H-bridge inverter
L_f	:	Filter inductor
LLC		Inductor Inductor Capacitance
MPPT	:	Maximum power point tracking
N_p	:	No. Of primary turns in flyback converter
N_s	:	No. Of secondary turns in flyback converter
n	:	Turn's ratio
PLL	:	Phase-locked loop
PWM	:	Pulse width modulation
P_{PV}	:	PV power
P_{PV_max}	:	Maximum PV power
P_o	:	Output power of the microinverter
P_{core}	:	Core loss of the flyback converter
P_{copper}	:	Conduction loss of the flyback converter
P_{cond}	:	Conduction loss of MOSFET
P_{sw}	:	Switching loss of MOSFET
R_{ds_on}		Drain-source resistance of MOSFET
R_{wire}		Winding resistance of the flyback converter
S_c	:	Clamp-switch
S_m	:	Main-switch
S_r	:	Resonant switch
S_{s1} & S_{s2}	:	Unfolding switches of the single-stage microinverter
S_1-S_4	:	H-bridge switches of the double-stage microinverter
T_1	:	Flyback transformer

T_d	:	Dead time
T_s	:	Switching period
$T_{resonant}$	:	Resonant period
THD		Total Harmonic Distortion
t_{d_off}		Fall time delay of MOSFET
t_f	:	Fall time of MOSFET
V_{Cc}	:	Voltage across the clamp capacitor of the flyback converter
V_{Cc_max}	:	Maximum voltage across the clamp capacitor of the flyback converter
V_{dc}	:	DC link voltage
V_{D1}	:	Voltage across the rectifier diode
$V_{ds,Sm}$	:	Main switch drain-source voltage
$V_{ds,Sc}$	:	Clamp switch drain-source voltage
$V_{ds,Sr}$	:	Drain-source voltage of resonant switch of auxiliary branch of H-bridge inverter
$V_{ds,S1\text{-}S4}$	:	Drain-source voltage of the switches of H-bridge inverter
	:	
$V_{gs,Sm}$	:	Main switch gate-signal
$V_{gs,Sc}$	:	Clamp switch gate-signal
$V_{gs,Sr}$	:	Resonant switch gate-signal
$V_{gs,S1\text{-}S4}$	:	Bridge switches gate-signal
V_{grid}	:	Grid voltage
V_j	:	Winding voltage of the flyback converter
V_{Ss1_max}	:	Maximum voltage stress of unfolding switch
V_{Ss2_max}	:	Maximum voltage stress of unfolding switch
V_{PV}	:	PV voltage

V_{PV_min}	:	Minimum PV voltage
V_{pulse}	:	Short-circuit pulse of H-bridge inverter
V_{Sm_max}	:	Maximum voltage stress across the main switch of the flyback converter
V_{spike}	:	Spike voltage of MOSFET
V_e	:	Effective core volume of flyback converter
ZCS	:	Zero current switching
ZVS	:	Zero voltage switching
ZVZCS	:	Zero-voltage and zero-current switching
Z_i	:	Characteristic impedance
ω_r	:	Resonant frequency
ΔB		Peak AC flux density of ferrite core
Δv_{Cc}	:	Voltage ripple across the clamp capacitor of the auxiliary branch of H-bridge inverter

CHAPTER 1: INTRODUCTION

1.1 Background

According to the International Energy Agency (IEA) 2012 analysis, approximately 1.3 billion people (19% of the global population) lived without access to electricity in 2010, a number that is expected to decline to about 1 billion people (12% of the global population) by 2030 [1]. Renewable energy has become economically competitive with conventional fuels in the past five years, and the IEA says that 60% of new connections will need to come from decentralized micro-grids and off-grid installations, such as solar home systems [2]. The shortcomings of renewable energy sources with unpredictable output can be mitigated by adopting energy storage techniques [3-5]. To control the emissions of toxic gases and metals from fossil-fuel steam electric generators, the generation capacity of clean and non-toxic renewable energies must be extended. The U.S. Annual Energy Outlook 2014 (AEO, 2014) estimated that the total renewable generating capacity will grow by 52% from 2012 to 2040 in the United States alone, with solar power leading the growth in renewable capacity by increasing from less than 8 GW in 2012 to more than 48 GW in 2040 [6]. The German *Energiewende* aims to generate at least 35% of its electricity from green sources by 2020 and is expected to surpass 80% (approximately 488 billion kWh per year) by 2050 [4].

Among the renewable energy sources, photovoltaic (PV) energy is considered one of the most promising emerging technologies. Based on the roadmap envisioned by the IEA, PV's share of global electricity will rise to 16% by 2050. In the last six years, the cost of full PV systems has decreased to one-third with a reduction of 80% cost of the PV modules because of mass production [7]. Given the natural abundance of crystalline silicon semiconductor materials, 90% of the world's total PV cell production are based

on silicon technology at an average cost of 0.10 USD/kWh and have conversion efficiencies in the range of 17%–25% [8]. Next-generation nanostructured solar cells are expected to reduce the cost to 0.03 USD/kWh with a 33% maximum conversion efficiency [9, 10]. In addition, low-cost perovskite solar cells will cause PV technology to proliferate more rapidly in the near future [11-13].

PV systems connected with the AC grid are more cost effective and require less maintenance than standalone systems because they do not need batteries for storage purposes. Li-ion or lead-acid battery storage is commonly used in standalone systems, which increases overall cost and requires additional control for charging and discharging [14-16]. Therefore, grid-connected PV systems occupy 99% of the total installed capacity compared to 1% of the standalone systems [17]. The performances of grid-connected PV systems are investigated and analyzed in [18-20]. Power inverter is one of the key components for injecting PV power into the AC grid. Grid-connected PV systems can range from a single PV module of around 100 W to more than millions of modules for PV plants of 290 MW [21].

On the basis of the different arrangements of PV modules, the grid-connected PV inverter can be categorized into central inverters, string inverters, multistring inverters, and AC-module inverters or microinverters [7]. The microinverter or module-integrated converter is a low power rating converter of 150–400 W in which a dedicated grid-tied inverter is used for each PV module of the system. The compact design attached to the back of each PV module with the highest maximum power point tracking (MPPT) accuracy and the provision for further integration of PV modules introduce an opportunity to realize a true plug-and-play solar AC PV generation.

1.2 Research Motivation and Scope

The AC-module inverters require an additional DC–DC stage to boost the voltage with respect to the grid level because of the low voltage rating of PV modules (typically <60 V DC). The additional DC–DC stage is usually used with a high-frequency compact transformer that provides the galvanic isolation and improves the safety issue without using line-frequency bulky transformer in the AC grid side. Line frequency transformers are only applicable in case of a single-stage centralized PV inverter to increase the inverter voltage to grid level [22-24]. Non-isolated boost converters or transformerless topologies are also used in the DC–DC stage because of their higher efficiency, increased compactness, and lower cost compared with isolated topologies [25-29]. However, the presence of leakage ground currents, the requirement of dual grounding, and the low voltage gain make transformerless topologies inefficient with respect to isolated topologies.

The main technical challenges for isolated PV microinverters are to achieve high conversion efficiency, low manufacturing cost, and long lifespan. Given that isolated microinverters contain high-frequency transformers, core losses and switching losses are the major concerns to attaining improved efficiency. To achieve a reliable integrated unit with each PV panel, having a compact and long-lifespan microinverter is desired.

1.3 Problem Statement

Various microinverter topologies have been proposed in the literature to improve the power conversion efficiency, power quality, compactness, reliability, and cost [7, 17, 25, 30, 31]. The flyback type microinverter is one of the most effective solutions due to its simple circuit structure and control [32-35]. Moreover, the inherent galvanic isolation provides a higher degree of reliability. However, the switching losses associated with the hard-switched operation and the low utilization factor of flyback

converters is the major drawbacks to achieve a reliable grid-tied microinverter. The hard-switched flyback converters undergo substantial switching losses in the high-frequency switches and high current and voltage stresses on power devices [32, 33, 36]. The interleaved flyback converters can reduce the voltage and current stresses by splitting them into two phases and hence increase the efficiency [37-39]. However, the power density is reduced and the high value of electrolytic capacitors shortens the lifetime of the microinverters.

Therefore, the problem is how to minimize the switching losses of a microinverter? The zero voltage switching (ZVS) of the high frequency switches is a better option in reducing the switching losses of the microinverters. The bidirectional switches placing in the secondary [34], or the active clamp circuit in the primary can achieve ZVS operation of the high frequency switch [40, 41]. Active-clamp circuit is also applied in dc-dc forward converter of a microinverter to achieve ZVS operation in the high frequency primary switches [42, 43]. Although the forward converter has better transformer utilization factor compare to flyback converter, the extra output inductor, and freewheeling diodes increase the cost of DC-DC converter.

The operating modes of the flyback microinverter can be classified into continuous conduction mode (CCM), discontinuous conduction mode (DCM), and boundary conduction mode (BCM). Among the conduction modes, which one is best suited for flyback converter? A number of literature has been found based on this. A hybrid operation of the DCM and BCM is a very effective solution to obtain high efficiency in different level of power. The DCM operation is conducted at lower power region and BCM in higher power. A phase-synchronization control strategy with hybrid operation can be obtained to increase the efficiency [44], where the ZVS turn-on is assured at BCM region. The addition of an adaptive snubber capacitor across the main switch adds

an advantage of achieving ZVS and zero current switching (ZCS) turn-on at BCM region of a hybrid operated microinverter [45]. A hybrid operation of the DCM and CCM is also exists based on a proportional-resonant controller with the harmonic compensator to overcome the RHP zero in CCM transfer function [46].

The active-clamp flyback microinverter operated with conventional hybrid control techniques suffers from a switching loss in the DCM region due to the lack of proper soft switching operation. Consequently, the unavoidable lower PV irradiance levels will increase the DCM region and deteriorate the performance of the microinverter. Therefore, In this dissertation, a new active-clamp flyback topology with resonant operation and a new hybrid control strategy of the microinverter is presented, which increases the efficiency for both single-stage and double-stage microinverter operations.

1.4 Research Objectives

The aim of the research is to design a high efficiency active-clamp resonant flyback microinverter for grid-connected photovoltaic AC module system, focusing on the soft switching and hence achieving higher efficiency of the converter. The following objectives are set to achieve the pre-defined goal.

1. To develop a new active-clamp resonant flyback microinverter for PV application.
2. To model a hybrid mode of operation based on DCM and BCM techniques.
3. To implement the proposed topology of microinverter with real time controller.

1.5 Dissertation Outline

The dissertation is divided into five chapters and is organized as follows:

Chapter 1 presents the background of the research along with the field of study and its significance. It explains the research motivation and scope and states the research

problem. It also provides the research objectives and outline of the dissertation structure.

Chapter 2 provides detailed literature review of the study, which describes the evolution of today's microinverters from the beginning of the grid-tied inverter, the standards set by the utility grid authorities, the performance requirements for PV converters, and the critical review of the performance of the topologies and control arrangements of some existing grid-connected isolated microinverters.

Chapter 3 explains the design procedure of the proposed topology of single- and double-stage microinverter. The selection of the circuit parameters is explained in this section. Moreover, the control strategies of hybrid modes of operation and resonant modes are described in this chapter.

Chapter 4 presents the verification of proposed topology by simulation results and experimental prototype. The experimental results are presented and analyzed in this chapter.

Chapter 5 concludes the dissertation providing a clear direction for building a resonant microinverter with high conversion efficiency and suggests for future work.

CHAPTER 2: LITERATURE REVIEW

2.1 Introduction

In this chapter, different types of grid-connected PV inverters are briefly discussed and the superiority of the microinverter over the other types of PV technologies is explained. The standards provided by the grid authorities and the microinverter performance criteria are described to set the benchmarks. This is followed by a critical review of existing single-stage and multi-stage microinverter topologies. The chapter also contains the different control techniques of microinverter and provides a comparative analysis among them. Finally, the comparison of the topologies with respect to the predefined benchmark is discussed and analyzed to build an efficient, reliable and low cost microinverter.

2.2 Types of Grid-Connected PV Inverter

The grid-connected PV inverter system was first introduced in the mid-1970s, when the direct coupling technology of solar cell arrays to electric power networks was introduced [47]. Subsequently, several designs of standalone and grid-interfacing systems were analyzed in the early 1980s to improve the power quality [48, 49]. These types of centralized inverters, as shown in Figure 2.1(a), were quite popular toward the end of the 1980s and brought about a number of projects in the USA [50, 51]. It is one of the best solutions for large-scale PV plants because of its simple structure and low cost. However, the main limitation of this PV system based on centralized inverter was the absence of a maximum power point operation for each module because of the shading and clouding effects. Moreover, the presence of high-voltage DC cables and the lack of flexibility to expand the system led researchers to invent different technologies for the interconnections of the PV modules. The recently developed multi-central

inverter, as shown in Figure 2.1(b), is a large-capacity inverter system that was realized through the parallel connection of the output from a number of central inverters [52].

String inverters can solve the central inverter's limitation partially. A single string of a sufficient number of PV modules or few PV modules with DC–DC stage are connected to the inverter to adapt with the grid voltage, as shown in Figure 2.1(c). Thus, a string inverter provides a more accurate MPPT and, hence, higher efficiency than a centralized inverter during partial shading and clouding effects [53]. The automatic fault diagnosis in distributed PV systems also ensures optimal energy harvesting and reliable power production [54, 55]. Employing these types of inverters in small- and medium-scale PV systems is common practice because of their low cost per watt and relatively high efficiency.

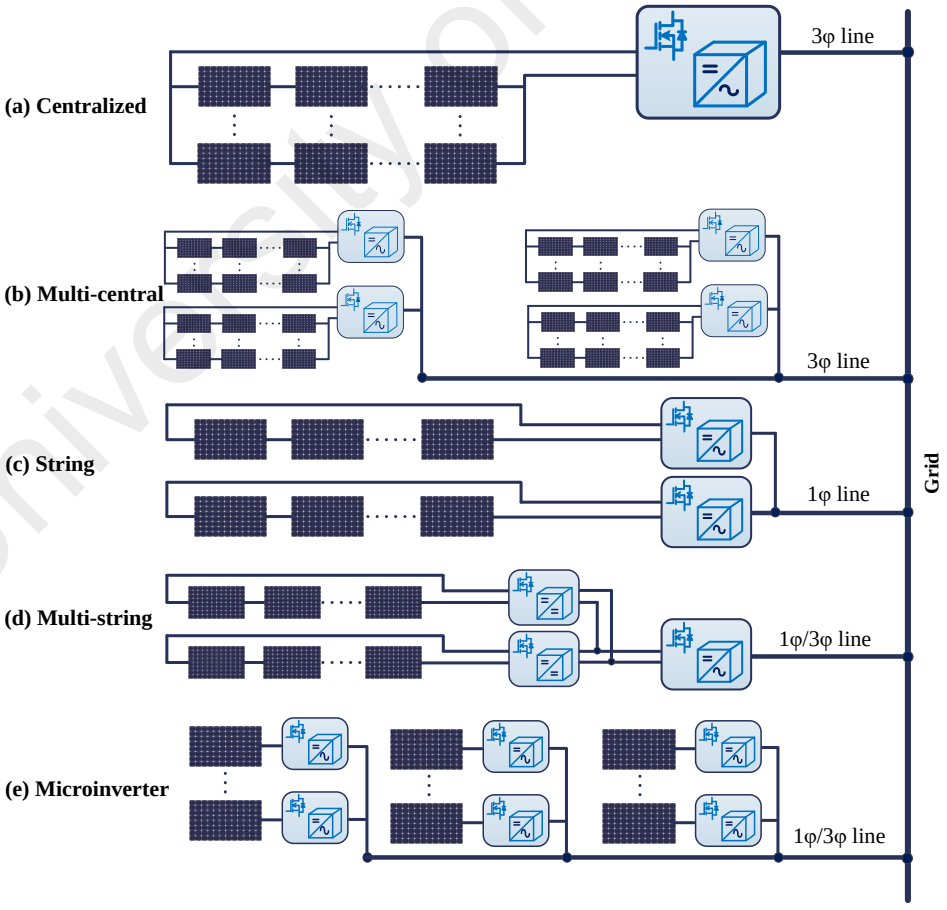

Figure 2.1: Grid-connected PV technologies

The multi-string concept, as shown in Figure 2.1(d), where several strings are interfaced with independent MPPT DC–DC stages to a common grid-tied inverter, has been developed to increase the MPPT accuracy and achieve flexibility [56]. This multi-string technology is suitable for both rooftop PV systems and medium- and large-scale power plants because of their flexible design with provision for enlargements.

Microinverter technology is the recent development to mitigate the problems that have arisen to obtain the MPP. The concept of an AC PV module was introduced in the 1990s to obtain a simple and more efficient PV system [57, 58]. The microinverter provides a dedicated grid-tied inverter for each PV module, as shown in Figure 2.1(e). Thus, it eliminates the mismatch losses between the PV modules and provides the highest MPPT accuracy with the dedicated power converter. It is also more suitable for places where the presence of partial shading is significant or for developing a small multi-rooftop PV system [59]. The microinverter provides the highest flexibility, including the provision, for enlarging PV systems with the simplest modular structure. Additional voltage amplification is necessary in an AC module inverter because of the low voltage rating (usually 30–45 V). Avoiding the bulky and costly low-frequency power transformer for amplifying the voltage up to the grid level is a general practice. An additional DC–DC stage is usually provided with either an isolated high-frequency transformer or a non-isolated boost converter. The voltage amplification stage may reduce the overall system efficiency, and the dedicated inverter for each module may increase the cost per watt. Attaching the inverter on the back of the PV module is possible because of the converter's small size, which creates a very compact design. IGBT or MOSFET provides the high power quality of the inverters in compliance with the specifications and standards of the PV system. The mass production of microinverters may lower manufacturing cost, and hence reduce the inverter cost per watt power generation.

2.3 Standards and Requirements for PV Converters

To ensure better system reliability, the interfacing of the microinverter with both the PV module and the grid should fulfill the standards of the PV systems. The main responsibilities of the microinverter are to extract the available maximum power at the PV module and inject sinusoidal current in the grid. The standards set by grid authorities for PV installations and performance requirements of PV converters are discussed in this section.

2.3.1 Standards of PV Systems

International codes and standards for grid connections are continuously being defined because of the rapid growth of PV applications. These standards are normally imposed by both national and international committees. International standards of the IEEE and the International Electrotechnical Commission (IEC) are worth considering. The European Committee for Electrotechnical Standardization (CENELEC) and the Association for Electrical, Electronic, and Information Technologies (VDE) are commonly accepted European regional standards organizations, whereas the National Electrical Code (NEC) is followed in the United States. A summary of the main features of these standards is presented in Table 2.1 [60-64].

2.3.1.1 Galvanic isolation

Galvanic isolation is one of the most important requirements for PV systems because of safety issues. The high parasitic capacitance between the PV cells and the grounded metallic frame causes the leakage ground current because of the absence of galvanic isolation. Despite some drawbacks of transformers, such as additional cost and reduced efficiency, the use of a transformer reduces leakage currents by providing galvanic isolation between the grid and the PV modules. The NEC 690.35 and 690.41 standards

demand that all PV sources and output circuits be provided with a ground-fault protection device or that one conductor of a two-wire PV system be solidly grounded when the output voltage of the PV modules exceeds 50 V. The limitations of the leakage ground current are defined by the VDE 0126-1-1 for both average and peak values, as shown in Table 2.1.

Table 2.1: Standards of the grid-connected PV system.

<table>
<tr><td>STANDARDS</td><td>IEEE1547.2</td><td>IEC 61727</td><td>U.S. NEC (NFPA 70)</td><td colspan="2">VDE 0126-1-1 & VDE-AR-N 4105</td></tr>
<tr><td>Galvanic isolation or System grounding</td><td>-</td><td>-</td><td>Compulsory with PV system above 50V</td><td colspan="2">-</td></tr>
<tr><td rowspan="4">Leakage ground current</td><td rowspan="4">-</td><td rowspan="4">-</td><td rowspan="4">-</td><td>average current (mA)</td><td>time (s)</td></tr>
<tr><td>30</td><td>0.30</td></tr>
<tr><td>100</td><td>0.04</td></tr>
<tr><td>300 (peak)</td><td>0.30</td></tr>
<tr><td>Anti-Islanding detection</td><td>Detection and Isolation within 2s</td><td>Disconnect within 2s</td><td>-</td><td colspan="2">Disconnect within 5s</td></tr>
<tr><td>Total Harmonic Distortion (THD)</td><td>Less than 5%</td><td>Less than 5%</td><td>-</td><td colspan="2">-</td></tr>
<tr><td>DC current injection</td><td>< 0.5% of rated output current</td><td>< 1% of rated output current</td><td>-</td><td colspan="2">< 1AMax disc. time: 0.2s</td></tr>
<tr><td>Operating voltage range</td><td>88% to 110%
Disc. time: 0.05-2s</td><td>85% to 110%
Disc. time: 0.16- 2s</td><td>-</td><td colspan="2">80% to 110%

Disc. time: 0.2s</td></tr>
<tr><td>Frequency range</td><td>59.3 to 60.5 Hz
Disc. time: 0.13s</td><td>49 to 51 Hz
Disc. time: 0.2s</td><td>-</td><td colspan="2">47.5 to 51.5 Hz
Disc. time: < 0.1 s</td></tr>
</table>

2.3.1.2 Anti-islanding detection

Anti-islanding detection is important for interrupting the PV inverter from providing power when the grid trips. Without recognizing the islanding operation, hazardous situations can arise for both humans and equipment. The IEEE 1547 and IEC 61727 standards specifically state that the Distributed Resources with Electric Power Systems will not allow the islanding condition, which should be detected and isolated within 2 s. The islanding detection techniques of distributed generation were presented in [65-69].

2.3.1.3 Total harmonic distortion

The harmonic content of the injected current should be minimized, and the THD should not be more than 5% according to the standards of IEEE 1547 and IEC 61727. These standards provide a maximum limit of 1% of DC current injection, whereas the VDE V 0126-1-1 allows a maximum DC current of 1 A. The THD of the injected current to the grid can be reduced by adopting a power conditioner parallel to the PV plant or by employing soft computing methods to improve the switching modulation technique for harmonics elimination [70-73].

2.3.1.4 Reactive power control

The monitoring of phase shifts or reactive power is extremely important for the PV systems that feed into the grid at medium- and low-voltage levels because the feeding of active power will lead to a voltage increase in the grid. According to the medium-voltage guidelines of the German Federal Association of the Energy and Water Industry, grid operators will be able to demand that inductive or capacitive reactive power be fed into the grid with a shift factor of 0.95. For the low-voltage grid, a shift factor of 0.90 is to be maintained for the power provided by the PV system. Various reactive power control schemes were presented and evaluated in [74-76].

2.3.2 Performance Requirements of PV Converters

The microinverter must assure the maximum power operation of the PV module accomplished with a maximum power point (MPP) tracker. It must be capable of maintaining a sufficient level of efficiency over a wide range of voltage and power fluctuations, because these parameters continuously vary with respect to solar radiation and ambient temperature. It should likewise be highly reliable and have the lowest component count with a greater degree of compactness.

2.3.2.1 Efficiency

Efficiency is the key requirement in designing a microinverter. Usually, an isolated microinverter has less efficiency when compared with a non-isolated transformerless microinverter. The maximum efficiency reported for isolated topology is 96.2% [43], whereas a peak efficiency of 99.01% is claimed for a single-phase non-isolated transformerless inverter [77]. However, the microinverter does not operate always at their maximum efficiency. Therefore, the 'European Efficiency' and the 'California Energy Commission (CEC) Efficiency' are very important and can be found as [78]:

European Efficiency = 0.03 x Eff5% + 0.06 x Eff10% + 0.13 x Eff20% + 0.1 x Eff30% + 0.48 x Eff50% + 0.2 x Eff100%.

CEC Efficiency = 0.04 x Eff10% + 0.05 x Eff20% + 0.12 x Eff30% + 0.21 x Eff50% + 0.53 x Eff75%. + 0.05 x Eff100%

The power losses in the semiconductor devices and the core loss of the high-frequency transformer reduce the efficiency of isolated microinverters. Given that microinverters are operated at low power and high frequency, most topologies use MOSFET as a power semiconductor switch. The power losses in MOSFET devices can

be divided as conduction loss and switching loss. The conduction losses of the MOSFETs can be obtained using the following equation.

$$P_{cond} = E_{cond}.f = \left[\int_0^{t_{on}} v_{ds}(t).i_d(t)dt\right].f$$
$$= \left[\int_0^{t_{on}} R_{ds(ON)}.i_d(t)^2 dt\right].f \quad (2.1)$$

where $R_{ds(ON)}$ is the drain-to-source on-state resistance, and f is the switching frequency.

The switching losses of the MOSFETs are the combination of turn on and turn off energy losses i.e. $P_{sw} = P_{on} + P_{off}$.

Turn on loss $P_{on} = \left[\int_0^{t_{d(on)}+t_r} v_{ds\_on}(t).i_d(t)dt\right].f \quad (2.2)$

Turn off loss $P_{off} = \left[\int_0^{t_{d(off)}+t_f} v_{ds\_off}(t).i_d(t)dt\right].f \quad (2.3)$

The expressions in equations (2.1–2.3) show that the total losses of the power MOSFET depend on the drain-to-source voltage v_{ds} and drain current i_d when the switching frequency remains constant. Consequently, controlling these two parameters can minimize the losses of the power devices. Therefore, realizing zero voltage switching (ZVS) and zero current switching (ZCS) techniques in the power MOSFETs can increase efficiency. These soft-switching techniques are generally achieved by either an auxiliary snubber circuit or by providing a bidirectional current through the switches [79-81]. The switching losses can also be reduced by using GaN high-electron-mobility transistors or SiC MOSFETs because of their extremely fast switching speed [82-85].

Core losses are the dominant loss in high-frequency transformers. According to the improved generalized Steinmetz equation, the core losses of any arbitrary waveform during a switching period can be obtained by the following equation [86].

$$P_{core\_loss} = V_e \frac{k_f(\Delta B)^{\beta-\alpha}}{T} \sum_j \left|\frac{V_j(t_i)}{NA_c}\right|^{\alpha} (\Delta t_j) \quad (2.4)$$

where $k_f = \frac{k}{2^{\beta+1}\pi^{\alpha-1}\left(0.2761+\frac{1.7061}{\alpha+1.354}\right)}$, V_e is the effective core volume, A_c is the cross-sectional area of the core, V_j is the winding voltage, ΔB is the peak-to-peak flux of the loop, and N is the number of turns.

Therefore, by regulating the design of the core and controlling the ratio of the winding turn, core loss can be adjusted to an acceptable degree. An optimum design of the transformer aids in increasing the efficiency [71]. The use of primary-parallel secondary-series multicore transformers improves coupling and reduces losses [87].

2.3.2.2 Installation cost

The microinverter must be cost effective and highly reliable. The major components of the cost of a grid-connected PV system are the PV module and the converter system. Within the last decades, the cost of the PV modules has been reduced by 68%, and other ancillary costs, including planning and fees, labor and construction materials have been decreased by 56% [17]. Therefore, the cost reduction of the microinverter surely limits the expenditure of the PV system. The estimated cost of the microinverter was forecasted to be approximately 0.19 USD to 0.24 USD per watt for a production of 10,000 units per year [88]. The recent market price of the microinverter varied from 116–542 USD for a unit of 215–300 W [89]. In addition, the costs of land, labor charge, or other local factors may vary the overall system cost from one region to another.

2.3.2.3 Lifespan

The microinverter lifespan is an important criterion in terms of reliability issue, which depends on the value of the power balancing decoupling capacitor. The size of the power decoupling capacitor is determined as follows [31]:

$$C_D = \frac{P_{PV}}{\omega_o V_{DC} \Delta V} \tag{2.5}$$

where P_{PV} is the rated power of the PV panel, V_{DC} is the DC voltage level across the decoupling capacitor C_D, ΔV is the maximum allowable peak-to-peak voltage ripple, and ω_0 is the line frequency. The low-power density film capacitor has a longer lifespan than the high-power density electrolytic capacitor. Hence, the reliability of the microinverter can be increased by either placing the capacitor on a high voltage DC link or by adopting a decoupling circuit on the PV side. The use of a Li-ion ultra-capacitor on the PV side also enhances the microinverter lifespan [90].

2.3.2.4 Power density

The microinverter design must be compact so that the device can be fitted with each PV module. The isolated type inverter is usually less compact than the transformerless inverter. The compactness of isolated type microinverters can be increased by increasing the switching frequency that reduces the transformer and filtering inductor sizes. The highest power density that has been gained is 4.86 kW per unit volume at a switching frequency of 80 kHz for a prototype of 400 W non-isolated inverter [91].

2.4 Topologies of Isolated Microinverters

Galvanic isolation exists between the grid and the PV modules in isolated microinverter types. The presence of a high-frequency transformer in the microinverter topology usually provides this isolation. The PV voltage level's boost up and conversion into an AC voltage can be accomplished either by a single-stage or multi-stage conversion circuit.

A multi-stage topology is shown in Figure 2.2(a), where one or more stages are dedicated to boost the DC voltage level, and the inverter circuit is employed in the final stage. A high-frequency transformer in the DC–DC converter provides the galvanic

isolation. The DC–DC converter is also used for MPPT. The succeeding DC–AC inverter injects the current into the grid through the pulse width modulation (PWM) technique. The DC link between the stages provides a high voltage level, thus reducing the value of the power decoupling capacitor. In a single-stage topology, the center-tapped transformer itself can boost the voltage level at the primary end and generate the rectified AC at the secondary end, as shown in Figure 2.2(b). Both the power decoupling and MPPT are performed on the primary side. The rectified AC at the secondary side is then converted to an AC through an unfolder. Recently developed isolated microinverters were mainly based on center-tapped single or interleaved flyback converters in single-stage topology and DC–DC converters cascaded with half or full-bridge inverters in multi-stage topology. These converters are proposed to either increase the lifetime and efficiency or decrease the cost of components.

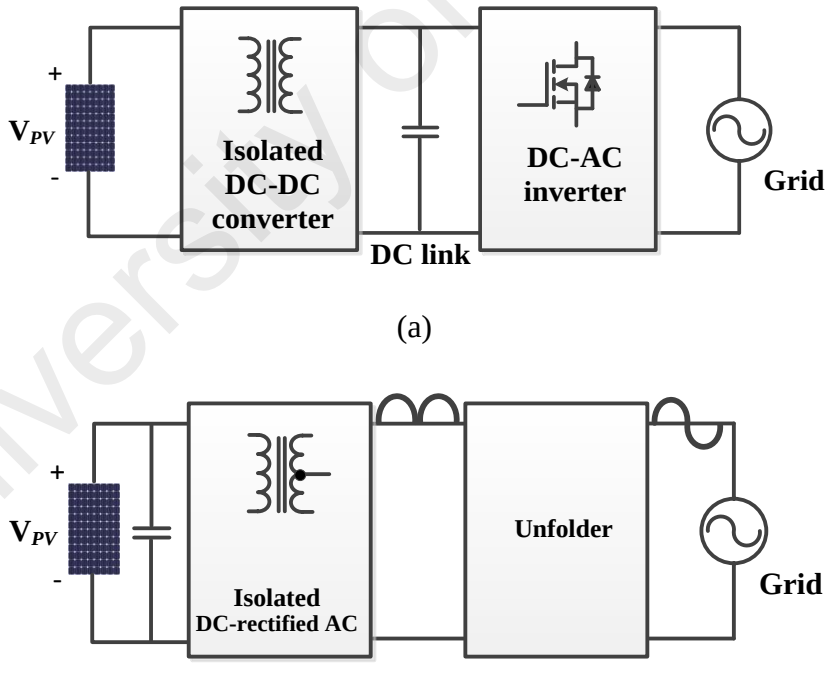

Figure 2.2: (a) Multistage isolated microinverter (b) Single-stage isolated microinverter

The microinverters are first classified into single- and multi-stage topologies. The single-stage topologies are further classified to single or interleaved flyback converter based on different auxiliary circuits and control techniques. The multi-stage topologies are mainly categorized with respect to different DC–DC converter circuits because DC–AC inverter circuits are almost the same in all topologies. The overviews of these recently proposed topologies are summarized in Figure 2.3. The analysis and discussion are detailed in this section.

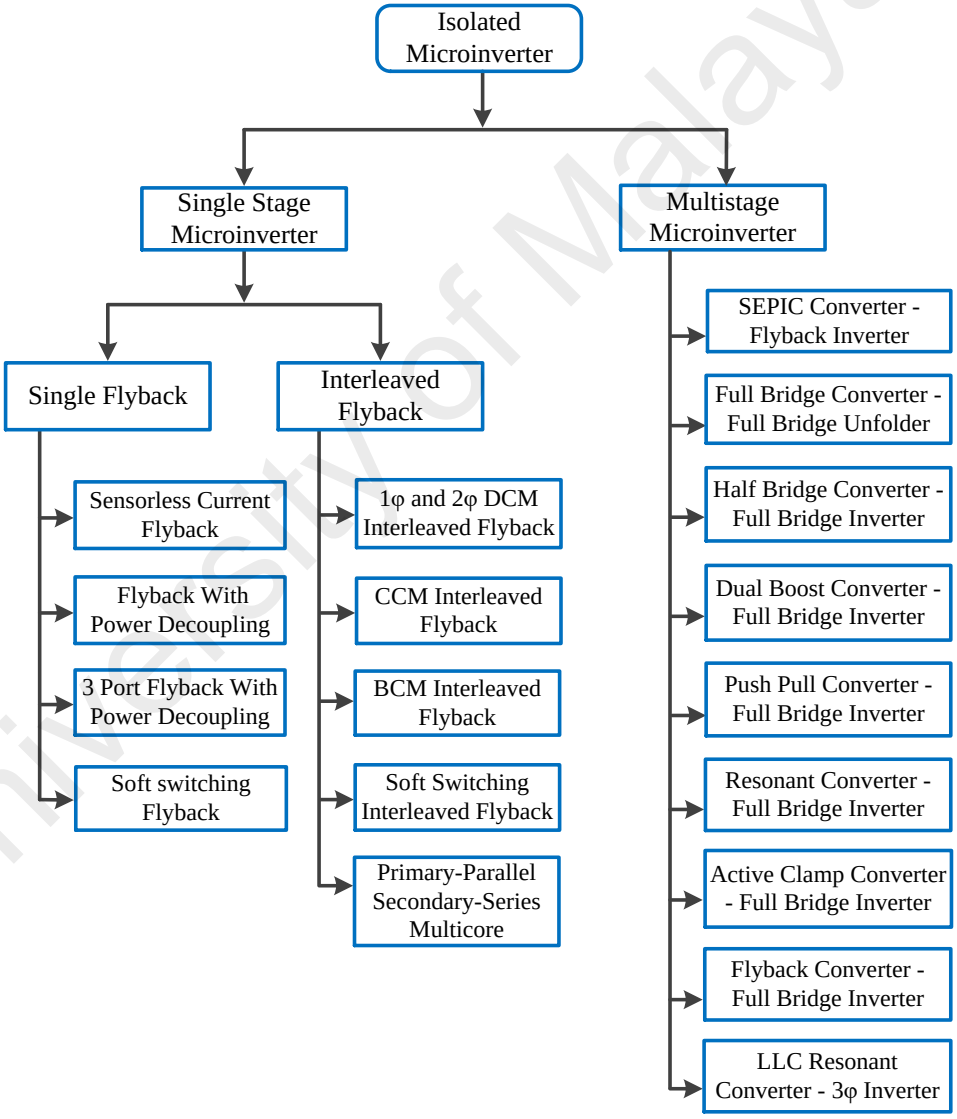

Figure 2.3: Topologies of isolated microinverter

2.4.1 Single-Stage Isolated Microinverter

A sensor-less current flyback inverter with center-tapped secondary winding was proposed in [92], as shown in Figure 2.4. Three PV panels are connected in parallel, and the MPPT operation is achieved by estimating the PV current from the PV voltage and, therefore, does not need any DC current sensor. Thus, the total system cost is reduced and less space is required. The use of a large capacitor (about 1.5 mF) for power decoupling decreases the reliability of the inverter. The projected efficiency is reported at 89% at a switching frequency of 9.6 kHz. However, the low switching frequency operation requires a bulky output filter to ensure the injection of high-quality current into the utility grid.

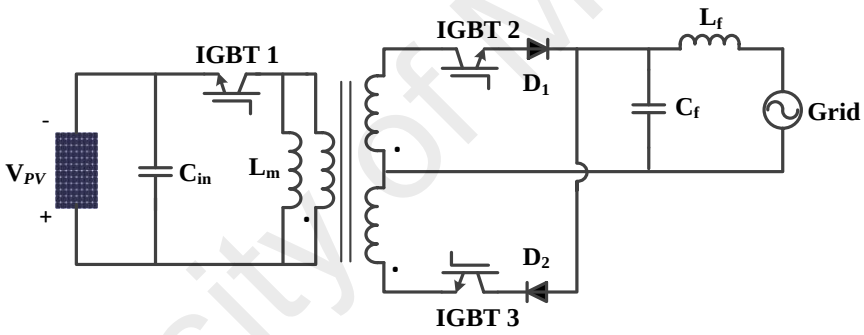

Figure 2.4: Single-stage single flyback inverter [92]

A discontinuous current mode (DCM) control flyback type single-stage microinverter was presented in [32], as shown in Figure 2.5, in which the decoupling of power pulsation is achieved by an additional circuit. The additional switch S_2 is controlled to release the energy of the primary winding to the decoupling capacitor C_D. The stored energy of the decoupling capacitor is then fed to the grid through secondary winding. Thus, the additional circuit enables the replacement of the short lifetime electrolytic capacitors with film capacitors of small capacitance. The maximum reported efficiency is only 70% because of the double conversion of energy and power loss on the MOSFET.

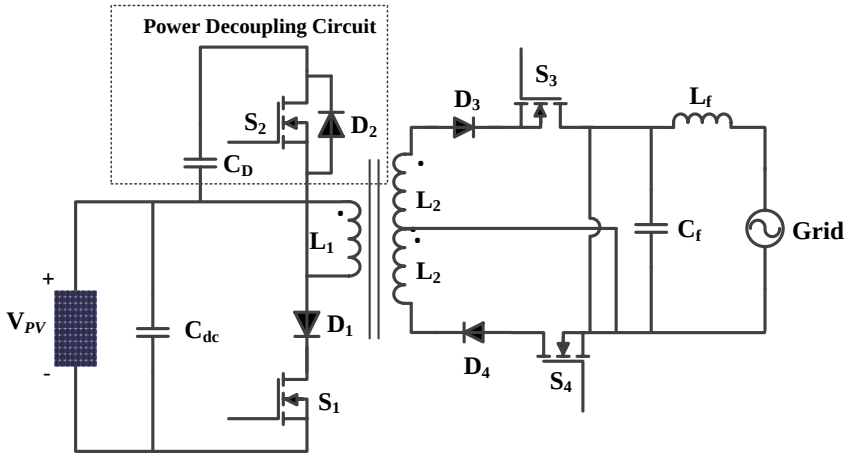

Figure 2.5: Flyback inverter with power decoupling circuit [32]

A three-port flyback converter was proposed in [33] and [36], as shown in Figure 2.6 and Figure 2.7, where the third port is dedicated for power decoupling using an extra switch. When the PV power is more than the output power to the grid, the surplus power is stored in the decoupling capacitor and then sent to the transformer magnetizing inductance to compensate for the deficit power with respect to the grid. The value of the decoupling capacitor is reduced by the presence of the high voltage and voltage ripples across its terminals. Hence, long lifespan, low power density film capacitors can be utilized instead of short lifetime electrolytic capacitors. However, the estimated peak efficiency is around 90.6% because of the large switching losses in the primary switches and the conduction losses in the diodes.

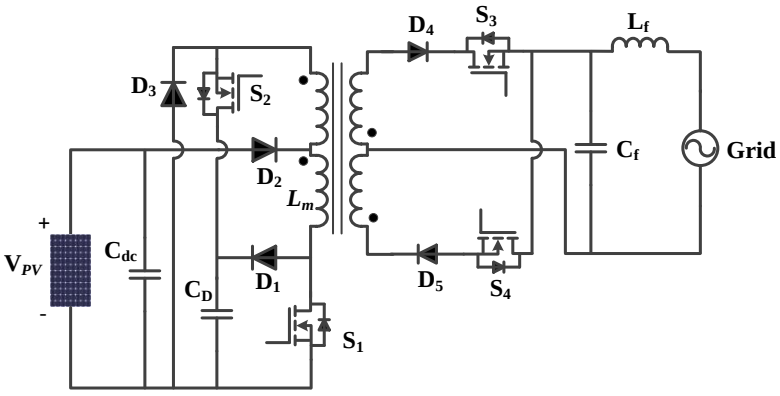

Figure 2.6: Three-port flyback inverter with power decoupling circuit-1 [33]

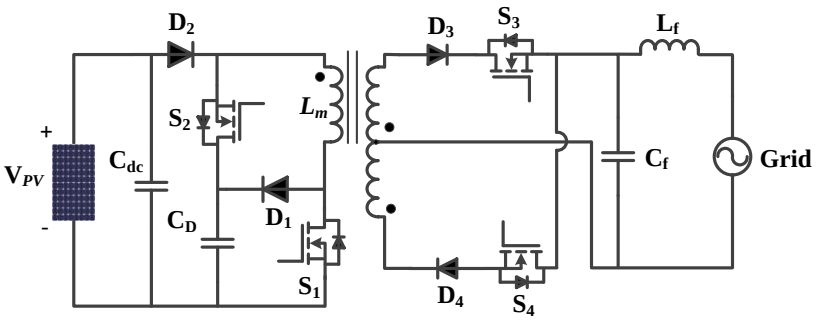

Figure 2.7: Three port flyback inverter with power decoupling circuit-2 [36]

Sukesh et el. presented a soft-switching approach in a single-stage flyback inverter [34], as shown in Figure 2.8. The two bidirectional switches placed at the secondary side of the transformer provide negative current to the primary switch from the grid side. The negative current discharges the output capacitor of the MOSFETs through the primary switch and attains ZVS. Hence, the efficiency is increased up to 94% with a minimum number of components, while the use of a large input capacitor decreases the lifetime of the converter.

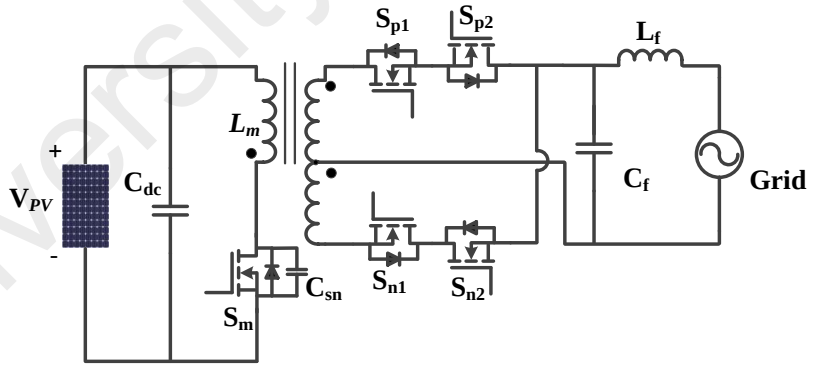

Figure 2.8: Single flyback inverter with soft switching [34]

An interleaved flyback microinverter was proposed by Zhang et al. [37] to improve the efficiency adopting a hybrid control of 2Φ DCM and 1Φ DCM, as shown in Figure 2.9. At heavy-load conditions, the 2Φ DCM operation shares the current and reduces the current stress between two interleaved phases. Thus, it reduces the conduction and turn off losses of the power MOSFETs and diodes, as well as the copper loss of the transformer. At light-load conditions, the 1Φ DCM operation sheds the additional phase of the microinverter, which minimizes the gate driving loss of the power MOSFETs and the core loss of the transformer. The peak efficiency attained is about 94.1%, taking the advantages of 2Φ DCM and 1Φ DCM. The use of a large electrolytic capacitor of about 6.37 mF for power decoupling will shorten the longevity of the PV inverter.

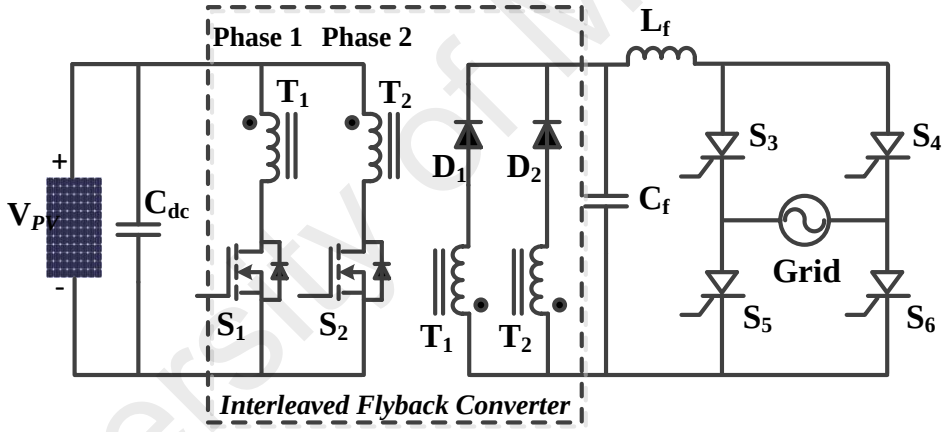

Figure 2.9: 1Φ and 2Φ DCM control interleaved flyback inverter [37]

In [38], the efficiency of the interleaved flyback microinverter (shown in Figure 2.10) is further increased to 95.7% by operating the converter in continuous conduction mode (CCM). A fourth-order system modeling is proposed to show the resonant peak introduced by the CL filter at the grid side. A proportional–integral controller followed by a lag term is then appended to mitigate the resonant peak's effect. The CCM operation has the advantages of high power density, low voltage and current stresses, and low electromagnetic interference, but it is more difficult to be controlled than the DCM.

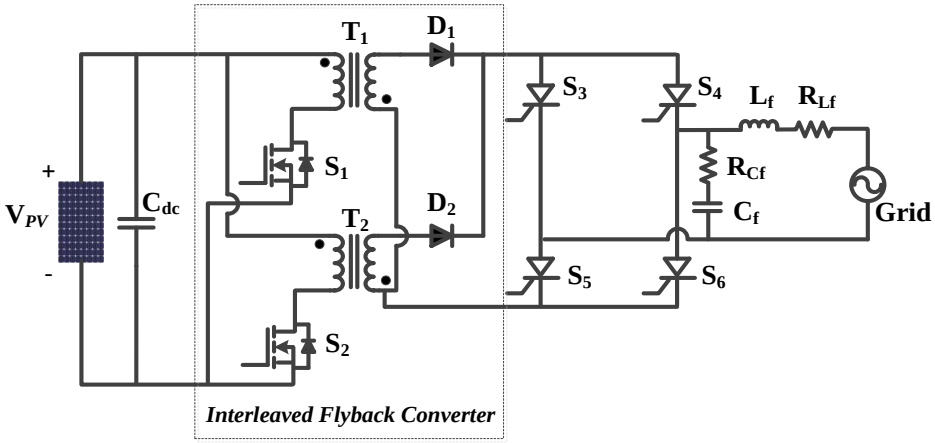

Figure 2.10: CCM control interleaved flyback inverter [38]

Gao et el. presented an interleaved flyback inverter in a boundary conduction mode (BCM) operation, as shown in Figure 2.11, which guarantees an efficiency of more than 94% at higher load conditions and a THD of only 2.459% [39]. Between the two flyback converters, one converter is operated alone up to a half-load condition, whereas both are operated in the interleaved mode at higher loads. Thus, the efficiency obtained is more than 93% even in a one-third full load. The switching loss is higher and efficiency is less than that of the other control strategy of interleaved flyback topology because of higher switching frequency (250-600 kHz) of the flyback converter.

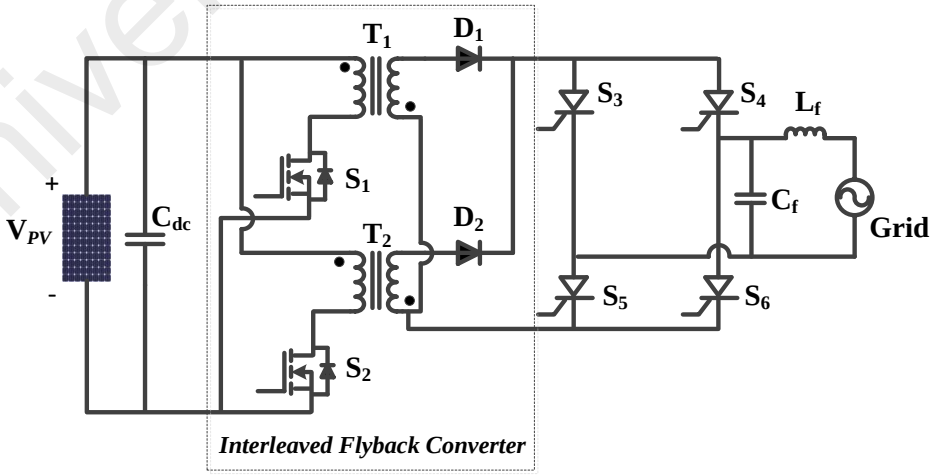

Figure 2.11: BCM control interleaved flyback inverter [39]

An interleaved flyback microinverter with an active clamp circuit on each phase was presented in [40]. The proposed circuit (shown in Figure 2.12) has three modes of operation. The first phase converter only operates without its clamping circuit when the PV output power is less than half of the PV module's maximum power and the voltage spike across the main switch S_1 is smaller. If the voltage spike across the main switch S_1 is higher, the clamping circuit of the first phase converter operates to reduce the spike. The two phase converters operate simultaneously with their active clamp circuit if the output power of the PV module is larger than half of the PV module's maximum power. The maximum efficiency is about 95.11%. This microinverter circuit suffers from the same shortcomings when a large decoupling capacitor (about 11 mF) is used similar to the former interleaved topology.

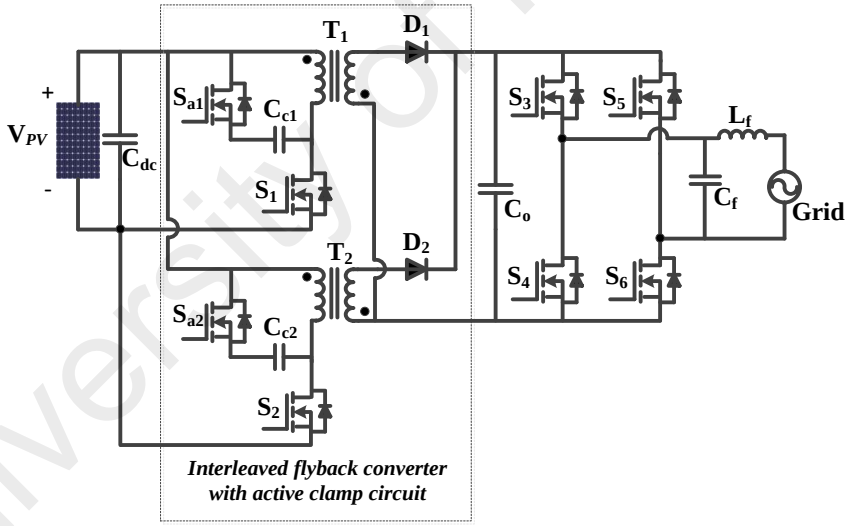

Figure 2.12: Interleaved flyback inverter with soft switching [40]

A closed-loop interleaving phase synchronization control method was proposed for the BCM/DCM hybrid-modulated flyback inverter [44]. The mismatch of magnetizing inductances between the two interleaved converters may create current oscillation and increase switching losses. By estimating the sub-converters' magnetizing inductance ratio, the slave converter's reference is obtained by multiplying the master's reference with the inductance ratio. Thus, the switching period of the slave will be equal to the

master without any switching phase error. The maximum efficiency improvement was reported to be about 0.58% with respect to the open loop system.

Parallel-connected primary cores and series-connected secondary cores of a multicore transformer were presented in [93]. The current stress of the primary switches is reduced because of the parallel connection of the primary windings, as shown in Figure 2.13. The grid voltage is easily achieved by the series connection of the secondary windings with a lower turn's ratio. Hence, the primary to secondary coupling at each transformer is improved and the leakage inductance is reduced. Low-profile ceramic capacitors can be easily utilized instead of the electrolytic capacitors because of the input decoupling capacitance's distribution among paralleled primaries. The peak efficiency of the multicore transformer inverter reported is only 92.4% because of the hard switching of the converter and a significant loss in the large number of transformers.

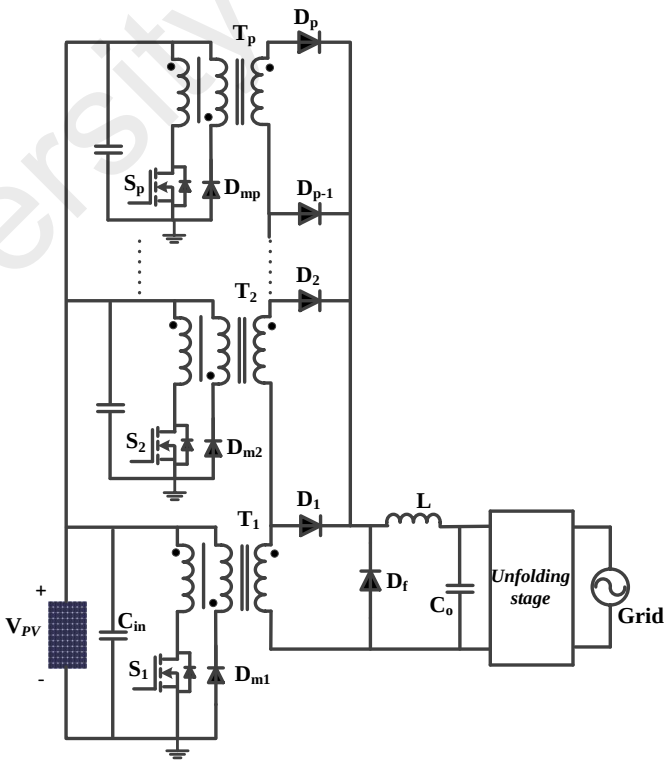

Figure 2.13: Primary-parallel secondary-series multicore inverter [93]

2.4.2 Multi-Stage Isolated Microinverter

In [94], a double-stage flyback type inverter was proposed with soft switching and enhanced power decoupling with a smaller capacitance. The first stage is employed to boost the DC voltage level and the second stage to pump a sinusoidal output current into the AC grid. The proposed topology is illustrated in Figure 2.14. The stored energy in the decoupling capacitor C2 is released to primary winding through switch S2 and then delivered to the grid from the secondary winding. A high voltage level caused by the raised DC voltage level at the first stage is presented at the terminals of the decoupling capacitor C2, which reduces the value of the capacitor. Soft switching (ZCS and ZVS) for the high-frequency switches S1 and S2 is achieved by an additional capacitor C_s that increases the efficiency up to 85.30%.

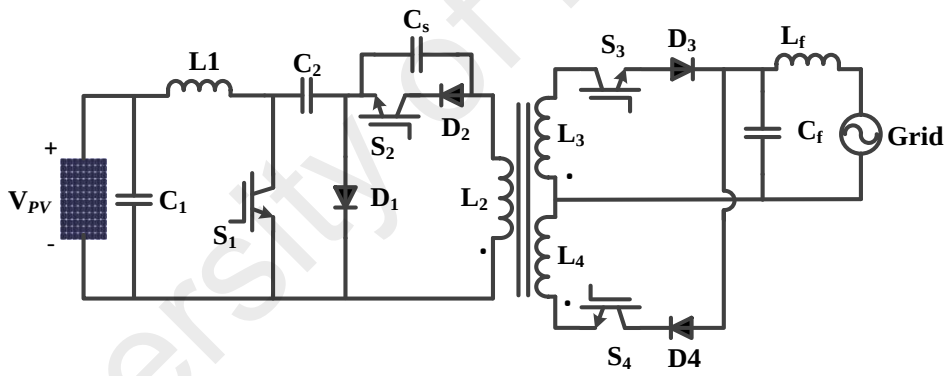

Figure 2.14: Double-stage flyback inverter with soft switching [94]

A three-stage power inverter was proposed in [95], as shown in Figure 2.15. In this topology, a full bridge converter is cascaded with a buck converter through a high-frequency transformer. The buck converter is assigned to shape the grid current injection in the inverter into a rectified sine wave. The unfolding stage then injects the current into the grid. The ZVS that minimizes the switching losses is attained by the phase-shift PWM controller at the first stage. The high-voltage DC link allows the replacement of non-reliable aluminum electrolytic capacitors with long-lifespan film capacitors. The overall efficiency is reported as 89% with a MPPT efficiency of 99%.

The major limitation of this topology is it has more components and hence costs more. In addition, a hindrance to form a compact design of microinverter integrated with the AC module arises because of the volume of two high-flux toroid inductors.

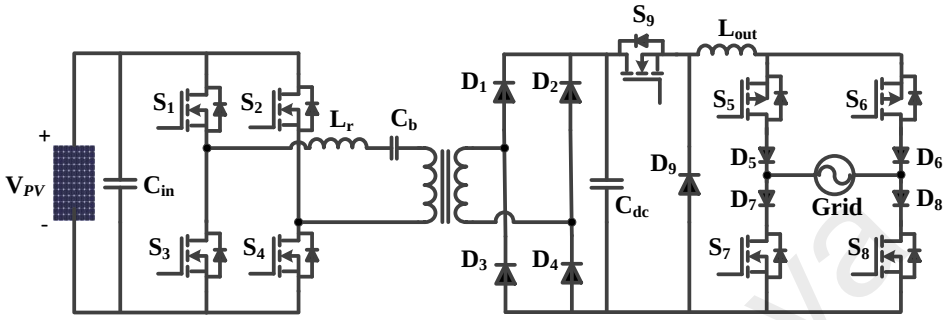

Figure 2.15: Three stage inverter with soft switching [95]

The authors in [96] proposed a microinverter of higher MPPT efficiency, as shown in Figure 2.16, in which a boost half-bridge DC–DC converter is cascaded with a full-bridge pulse-width modulated inverter. A plug-in repetitive current controller based on a fourth-order linear phase IIR filter is realized to obtain the high-power factor and low THD of voltage and current. Although the peak conversion efficiency of the DC–DC converter is reported to be 97.0%–98.2%, the overall efficiency of the microinverter will certainly decrease because of the switching losses at the full bridge inverter.

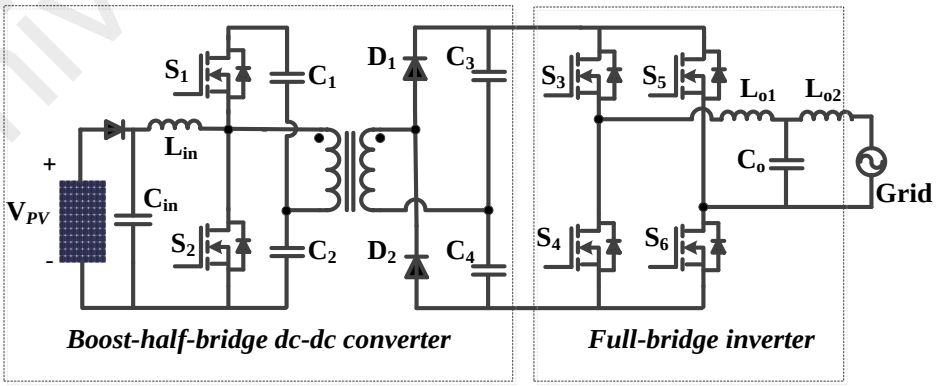

Figure 2.16: Boost half-bridge converter with full-bridge inverter [96]

A solar microinverter with a pseudo DC link was presented in [97], in which an inverse-buck current-fed dual boost converter with voltage-doubler capacitors at the secondary of a high-frequency transformer is cascaded with a full bridge inverter, as shown in Figure 2.17. The PV panel voltage is fed directly to the input of the interleaved dual boost circuit when the AC grid voltage is higher than a predefined boundary voltage. Solar energy is first stored into the input inductors L1 and L2 and then released to the voltage-doubler capacitors via a transformer. Solar energy is stored into the buck inductor L_b and then released via diode D_b when the AC grid voltage is smaller. The lifespan of the inverter is enhanced by placing the low-valued film capacitors. The conversion efficiency is reported as 93% with an MPPT accuracy of 0.98. However, such efficiency compensates for the high cost because of the large number of components used in this topology.

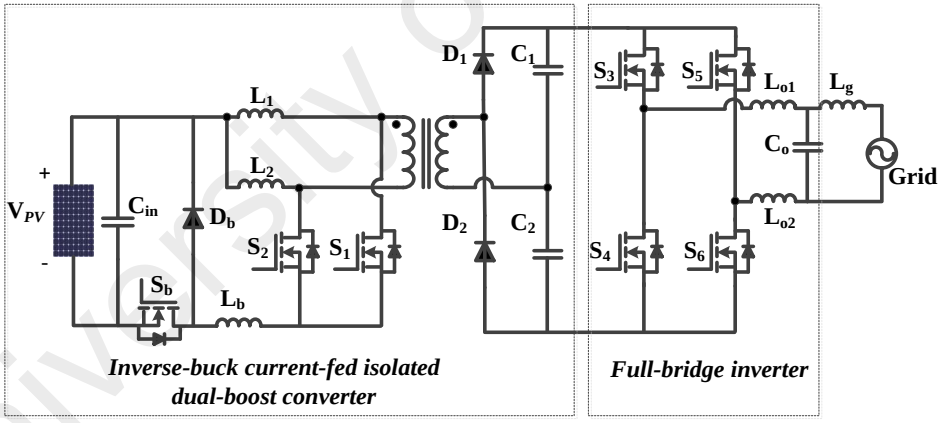

Figure 2.17: Dual boost converter with full-bridge inverter [97]

A soft-switching current fed push-pull converter with cascaded full-bridge inverter was proposed in [98], as shown in Figure 2.18. The transformer's secondary leakage reactance and the parallel capacitor form a LC resonant circuit. Soft switching of the primary switches is achieved by ZVS turn-ON and ZCS turn-OFF, with the leakage current provided by the LC tank circuit. The maximum efficiency of the proposed DC–DC converter is reported to be 96.6%. The overall efficiency of the microinverter is not mentioned, but it will certainly be reduced because of the cascaded DC–AC inverter.

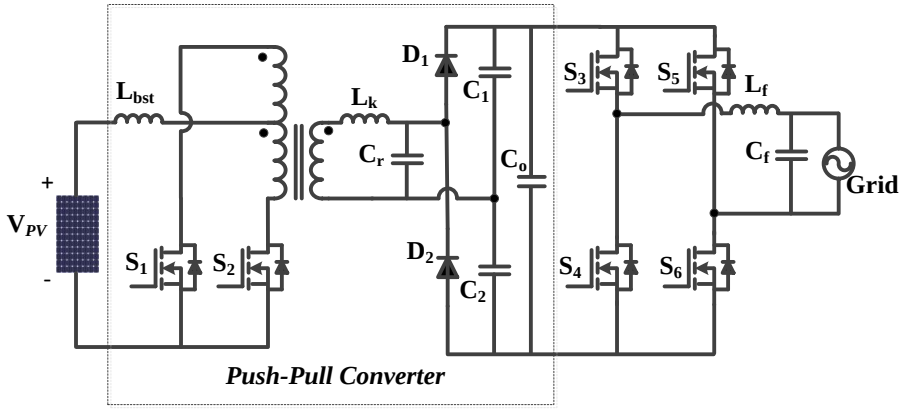

Figure 2.18: Current-fed push-pull converter with full-bridge inverter [98]

Another hybrid resonant DC–DC converter with a bidirectional GaN switch parallel to the secondary of the high-frequency transformer was presented in [99], as shown in Figure 2.19. The converter runs with three operating modes, namely, pure, buck, and boost series resonant modes. The output diodes D_1 and D_2 achieve ZCS, ensuring that the inductor current reaches zero at all operating modes. The primary side of MOSFETs can achieve ZVS and near to ZCS with the proper design of the transformer magnetizing inductance L_m and for certain operating conditions. Thus, the proposed DC–DC converter shows a high power conversion efficiency of 97.5%.

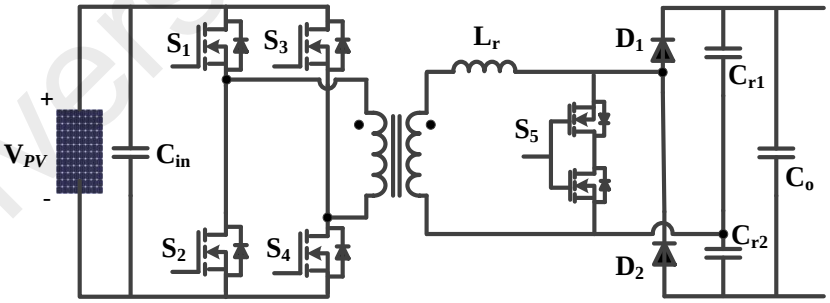

Figure 2.19: Hybrid resonant dc-dc converter with soft switching [99]

An active clamp circuit parallel to the primary switch is proposed in [43], as shown in Figure 2.20, which achieves ZVS by recycling the energy stored in the leakage inductance of the transformer. A series-resonant voltage doubler at the secondary of the transformer also achieves ZCS turn-off of the rectifier diodes and the reverse recovery loss is eliminated. A high efficiency and reliability of the inverter is assured because a

single switch is modulated at the switching frequency. The maximum efficiency is reported to be 96.2% with a THD of 3.8%.

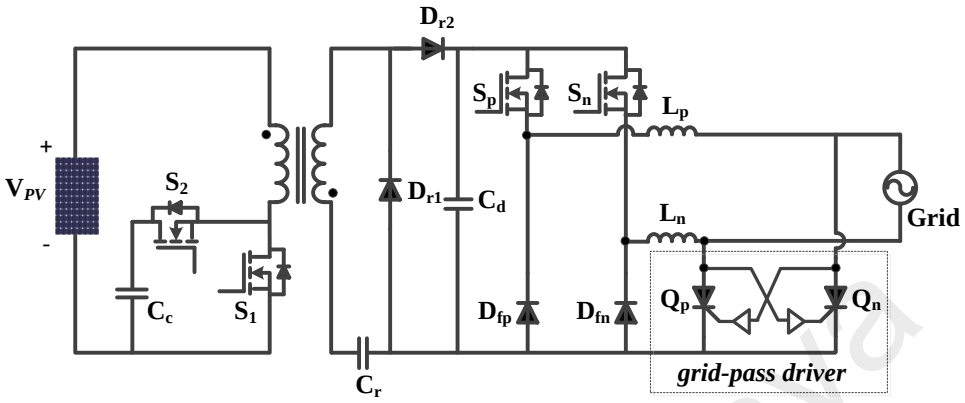

Figure 2.20: Active clamp dc-dc converter with single switch modulated inverter [43]

Korosec et al. proposed a flyback-based microinverter with a high-frequency AC (HFAC) link [100], as shown in Figure 2.21. An active decoupling circuit, which replaces the electrolytic capacitor with a long lifespan film capacitor, is proposed. The proposed sinusoidal pulse-density modulation technique achieves the ZCS of the transistors in the decoupling circuit and in the output stage of the converter. The hard-switched primary in the input stage and the additional flyback in the decoupling circuit might reduce the overall performance of the proposed converter.

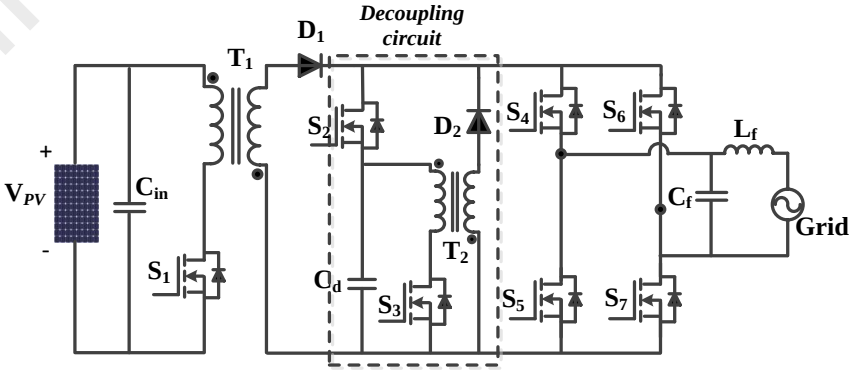

Figure 2.21: Flyback inverter with HFAC-link and active decoupling circuit [100]

The authors in [101] and [70] proposed a three-phase microinverter that allows soft switching in the converter circuit. As shown in Figure 2.22, a two-stage microinverter is proposed in [101], where the first stage is a full-bridge LLC resonant DC–DC converter dedicated to the MPPT operation and to provide a high-voltage DC link. In the second stage, the body capacitor of each MOSFET and the output inductor forms a resonant circuit. Thus, the ZVS is achieved through the bidirectional inductor current, and the converter does not require any auxiliary components for soft switching. The high efficiency of the converter (about 96%) and the use of a long lifespan DC link film capacitor makes this topology a potential candidate for three-phase PV solar farms. In [70], a triple-loop controller is designed for the inverter stage of the topology shown in Figure 2.22. A variable-frequency bidirectional current mode controller is presented for the inner current loop control of the inverter-side inductor that achieves ZVS in the inverter stage. A second current control loop is employed by detecting the injected grid current to achieve high loop gain at the harmonic frequency, and thus improves the stability of the system. The third voltage control loop is implemented to regulate the outer bus voltage at the reference value by changing the injected grid current.

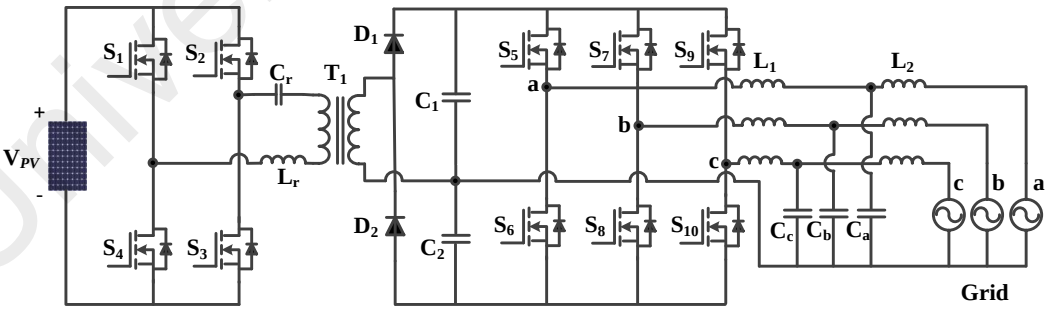

Figure 2.22: Full-bridge LLC resonant converter with three-phase inverter [70, 101]

2.4.3 Comparison of Microinverter Topologies

The key components of the single- and double-stage isolated PV microinverters are summarized in Tables 2.2 and 2.3 respectively. Isolated microinverters provide high-quality power by reducing the harmonics in the injected grid current. The galvanic isolation provided by high-frequency transformers also aids in ground fault protection. Therefore, most grid standards for distributed power generation systems are fulfilled by isolated microinverters. Tables 2.2 and 2.3 shows that almost all single- and multi-stage microinverter topologies have low THD in the output AC current, which ensures better power quality than the transformerless topology. A large valued electrolytic decoupling capacitor is placed on the PV side in most single-stage microinverter cases to balance the constant PV power with the time varying grid power. This electrolytic capacitor reduces the lifespan of the converter. Low-valued film capacitor is used in the DC link in most multi-stage microinverters. However, multi-stage topologies have more components because of the additional DC–DC converter stage. In this section, a comparison of the both single- and double-stage isolated PV microinverter topologies is presented.

Table 2.2: Comparison of single-stage isolated PV microinverters

	Performance requirements								Grid requirements	
Fig. [Ref.]	Power rating (W)	Decoupling capacitor	No. of power switches	Switching technique	Operating mode	Peak Effi-ciency	Lifetime	Cost	Galvanic isolation	THD
2.4 [92]	300	1500 µF (Electrolytic)	3	Hard switching	DCM	89%	Short	Low	Yes	-
2.5 [32]	100	40 µF (Film)	4	Hard switching	DCM	70%	Long	Medium	Yes	-
2.6 [33]	100	46 µF (Film)	4	Hard switching	DCM	90.6%	Long	Medium	Yes	< 1.7%
2.7 [36]	100	46 µF (Film)	4	Hard switching	DCM	90.23%	Long	Medium	Yes	< 1.9%
2.8 [34]	250	5000 µF (Electrolytic)	3	Soft Switching	Modified BCM	94%	Short	Low	Yes	-
2.9 [37]	200	6370 µF (Electrolytic)	6	Hard switching	2Φ and 1Φ DCM	94.1%	Short	Medium	Yes	< 3.79%
2.10 [38]	200	5600 µF (Electrolytic)	6	Hard switching	CCM	95.7%	Short	Medium	Yes	< 4%
2.11 [39]	200	8800 µF (Electrolytic)	6	Hard switching	BCM	94%	Short	Medium	Yes	< 2.46%
2.12 [40]	250	11000 µF (Electrolytic)	8	Soft Switching	DCM	95.11%	Short	Medium	Yes	-
2.13 [93]	120	250 µF (Film)	12	Hard switching	BCM and DCM	92.4%	Long	High	Yes	< 5%

Table 2.3: Comparison of multi-stage isolated PV microinverters

Fig. [Ref.]	Performance requirements								Grid requirements	
	Power rating (W)	Decoupling capacitor	No. of power switches	Switching technique	Operating mode	Peak Effi-ciency	Lifetime	Cost	Galvanic isolation	THD
2.14 [94]	500	70 µF (Film)	4	Soft Switching	DCM	85.30%	Long	Medium	Yes	< 2.5%
2.15 [95]	150	8.2 µF (Film)	9	Soft switching	-	89%	Long	High	Yes	< 5%
2.16 [96]	210	18 µF (Film)	6	Hard switching	-	-	Long	High	Yes	0.9% – 2.87%
2.17 [97]	250	31 µF (Film)	7	Hard switching	-	93%	Long	High	Yes	-
2.18 [98]	250	-	6	Soft Switching	-	-	Long	High	Yes	-
2.20 [43]	400	36 µF (Film)	6	Soft Switching	-	96.2%	Long	High	Yes	3.8 %
2.21 [100]	100	25 µF (Film)	6	Mixed	-	-	Long	High	Yes	-
2.22 [101]	400	35.3 µF (Film)	10	Soft Switching	Modified BCM	96%	Long	High	Yes	< 2.5%

2.5 Control Techniques of Microinverters

The flyback micro-inverter can be operated with its magnetizing current in continuous conduction mode (CCM), discontinuous conduction mode (DCM), or boundary conduction mode (BCM) [102, 103]. When the converter is operated in CCM with continuous magnetizing current, as shown in Figure 2.23, the primary peak current is lower than that when the converter is operating in DCM or BCM so that converter turn-off losses are lower as well. The control of the output current, however, is difficult as the converter has a right-hand plane (RHP) zero in its transfer function when it is operated in CCM. As a result, the converter needs to be implemented with a complex control scheme to avoid having a distorted output current, which makes CCM operation unsuitable for low cost PV micro-inverters [104, 105].

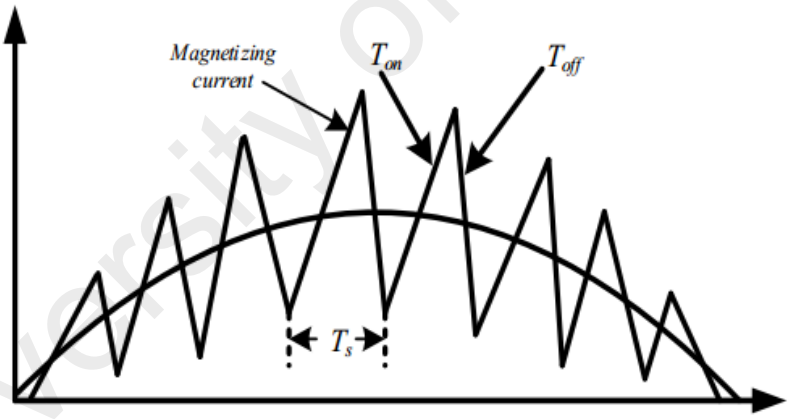

Figure 2.23: Continuous conduction mode (CCM) of magnetizing current

Discontinuous conduction mode (DCM) operation is preferred for flyback microinverter [102, 103], which is shown in the Figure 2.24. When a flyback micro-inverter is operated in DCM, its transformer is completely discharged by the end of each switching cycle and its current is a train of triangular pulses whose peaks are bounded by a sinusoidal reference envelope.

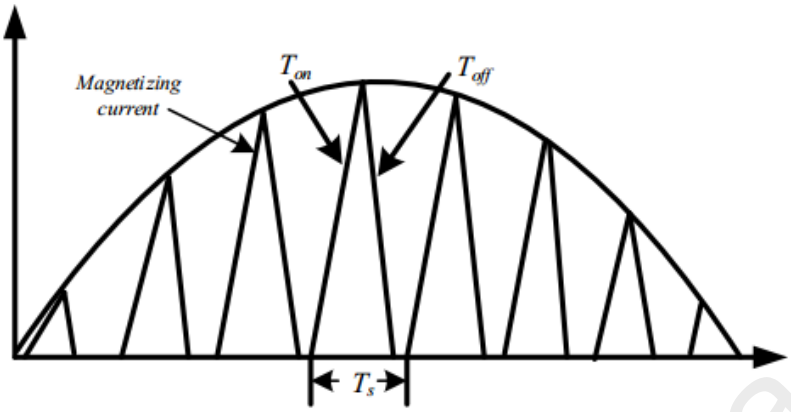

Figure 2.24: Discontinuous conduction mode (DCM) of magnetizing current

These current peaks, however, can be high; one way to reduce these current peaks is to operate the converter in BCM, as shown in Figure 2.25. With BCM, the switch is turned on as soon as the magnetizing current falls to zero, after the transformer has been fully demagnetized, so that this current is at the boundary of CCM and DCM. The main drawback with BCM is that the converter must be operated with variable frequency control as the length of the switching cycle must vary throughout the AC grid voltage line cycle. As a result, the control scheme required to implement the converter in BCM is more sophisticated than what is required for DCM, but it is not as sophisticated as what is required for CCM. Moreover, the switching frequency may become very high for certain applications especially when the converter must operate over a wide input voltage range and load range and this can create switching losses that can reduce the converter efficiency.

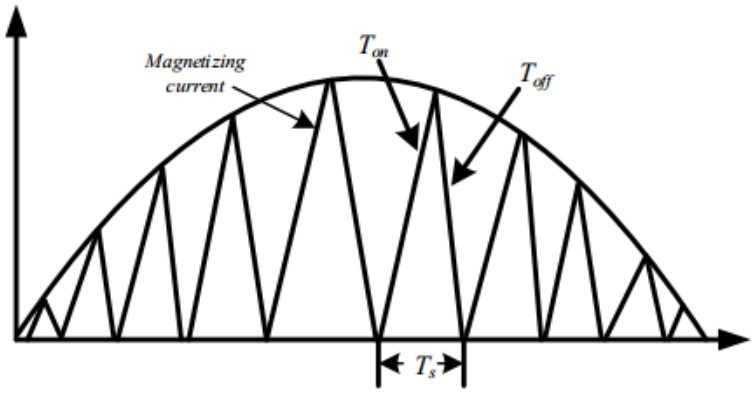

Figure 2.25: Boundary conduction mode (BCM) of magnetizing current

As a result, some authors [37, 102] have proposed the use of hybrid schemes (i.e. combination of DCM and BCM) where the converter is made to operate with a combination of DCM and BCM, depending on the operating conditions. For example, the converter is designed to operate with a certain maximum frequency with BCM; as the load is decreased, then the switching frequency is decreased too. For lighter loads, when the switching frequency can become so low that it enters the audible range, the converter is made to operate with DCM with a fixed switching frequency that is just above this range.

2.5.1 Comparison of Microinverter Control Techniques

The single flyback microinverters presented in [32, 33, 36, 92] are designed to operate in DCM because they have simple control loops and achieve higher efficiency over the BCM in low-power PV application. However, the DCM cannot maintain good performance in relatively high-power inverters. The 2Φ DCM and 1Φ DCM controls for interleaved flyback inverters improve efficiency by reducing both the switching and core losses by splitting the phase with respect to the light and heavy load conditions, which are presented in [37]. The flyback converter operated in CCM has lower peak currents and hence higher efficiencies with respect to the DCM and BCM. However, the

right half plane (RHP) zero in the control to output the current transfer function in a flyback CCM converter causes difficulty in controlling the output current of the converter effectively. The widely varying RHP zero in the CCM operation results in poor tracking performance when the operation changes to DCM at low instantaneous AC voltages and deteriorates the output power quality. This problem can be solved by employing the average current mode control for the primary current control loop [106], in which the primary switch current is sensed and controlled directly rather than the output current. However, the average current mode control scheme may cause sub-harmonic oscillations that will lead to higher distortion in the current waveform.

BCM is a feasible solution for high power levels with a reduction of the transformer volume to 50% and presents a smaller THD than DCM. The BCM for flyback inverter presented in [102] has a very high-power factor regulation with very low total harmonic distortion. The inverter efficiency is also higher after a certain power level. Although the control loop and filter design in BCM are more complicated, the shortest possible volume with higher efficiency establishes this scheme as one of the most appropriate mode for PV applications. The modified BCM control with the charging of the transformer magnetizing inductance in the reverse direction of the power flow is applied in the single flyback topology, shown in [34], that provides a reactive current for soft switching. BCM is also preferable in interleaved flyback inverter shown in [39], in which higher efficiency and lower THD is maintained at the cost of a more complicated control because of the variable switching frequency.

A hybrid operation of BCM and DCM can also be applied for multicore inverter shown in [93], where an optimization is carried out to select either the DCM or BCM with respect to the low level or high level of power respectively. A phase-synchronization control strategy with hybrid operation can be obtained to increase the

efficiency [44], or to improve the output power quality and converter efficiency for a wider power range [35]. A hybrid operation of the DCM and CCM is also exists based on a proportional-resonant controller with the harmonic compensator to overcome the RHP zero in CCM transfer function [46].

2.6 Performance Comparison of the Microinverters

The performance requirements of the PV converters were specified previously. This section discusses the fulfillment of these requirements by the isolated microinverter topologies presented previously.

2.6.1 Switching Loss and Conduction Loss of MOSFET

The aforementioned topologies review shows that the efficiency of an isolated microinverter is mostly reduced by the power loss in the semiconductor devices. Microinverters are designed for different power ratings. The power losses of the hard-switched single-stage flyback topologies presented in [32, 33, 36, 92] are more than those of the soft-switched topologies. The major part of these losses is the switching losses because of the high-frequency primary switches. The switching losses in the secondary circuit are comparatively less because they are operated at the grid frequency. The multi-stage isolated topologies shown in [95-97] also have high power losses because of the full-bridge converter; boost DC–DC converter, or full-bridge inverter. The efficiency can be improved by reducing the switching frequency, but low switching frequency will increase the size of the transformer and filter inductor.

Hence, soft-switching technique is one of the best solutions to reduce semiconductor losses, especially the switching losses of the power MOSFET. In the single flyback topology, ZVS can be achieved by employing a bidirectional switch on the secondary, as shown in [34]. The employment of active clamp switching in the interleaved flyback

or in the multi-stage topology reduces the power loss by achieving ZVS, as shown in [40, 43]. The LC resonant tank circuit is also a good technique to achieve soft switching without any of the additional switching components as well as to achieve less power losses in the inverter [98, 101]. ZVS is usually desired for the soft switching of microinverters because it can prevent both the diode reverse recovery and semiconductor output capacitance from inducing switching losses in MOSFETs.

2.6.2 Core Loss of High-Frequency Transformers

A high-frequency transformer is inserted in the inverter circuit for isolation. Flyback, push-pull, and full-bridge or half-bridge boost converters are usually utilized in the DC–DC converter stage. Equation (2.4) shows that a larger core size increases the cross-sectional core area and hence decreases the core loss. However, using a large transformer for isolated microinverter is not feasible. Therefore, the core loss is reduced by either splitting the phase, as shown in [37], or adopting a multicore topology, as shown in [93]. However, both increase the overall system cost with the reduction of core loss. The variation of flux density because of the high peak-to-peak ripple inductor current at the primary also reduces the efficiency of the transformer. Therefore, the proper selection of core materials and design aids to reduce the core loss.

2.6.3 Lifetime of Microinverters

The selection of input or decoupling capacitor is very important because the reliability of an AC module system depends upon it. The value of the decoupling capacitor with respect to the different PV voltage levels and power rating of the single and interleaved flyback microinverters is presented in Figure 2.26. The maximum allowable ripple voltage is assumed in the range of 2–3 V. The figure shows that the range of the capacitor lies between 5000 and 11000 μF for different types of flyback

topologies. Therefore, these types of high-density electrolytic capacitors have very limited lifespans with respect to the film capacitor.

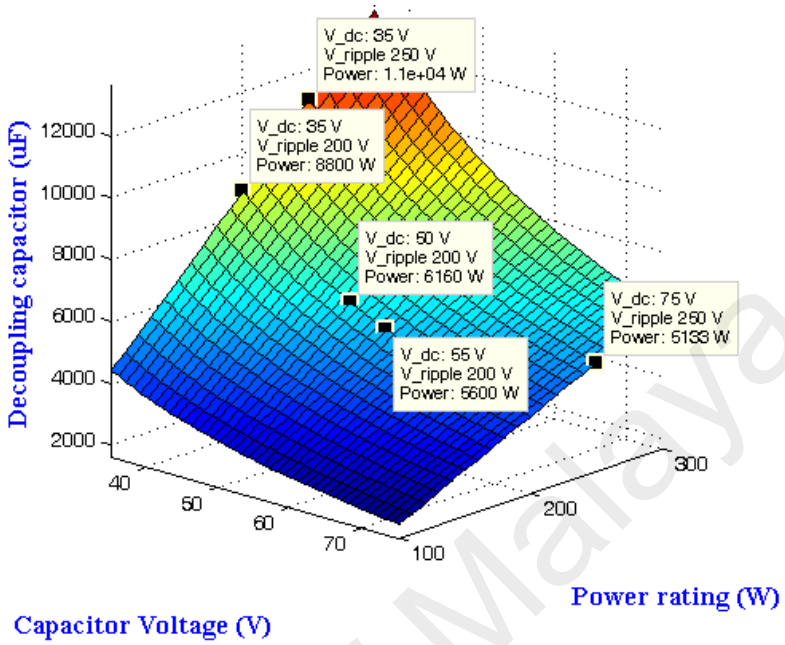

Figure 2.26: Selection of decoupling capacitor in single-stage flyback topology

The voltage across the capacitor is increased in the flyback topologies presented in [32, 33, 36] by employing a power decoupling circuit. The multi-stage microinverters include a DC–DC converter stage that provides a high-voltage DC link, which allows the provision of placing the decoupling capacitor. Therefore, the high-voltage DC link and the scope of increasing the allowable ripple voltage across the capacitor reduce the capacitor value, as shown in Figure 2.27. Thus, long lifespan low power-density film capacitors can be employed for the abovementioned multi-stage topology and the flyback converter with a decoupling circuit.

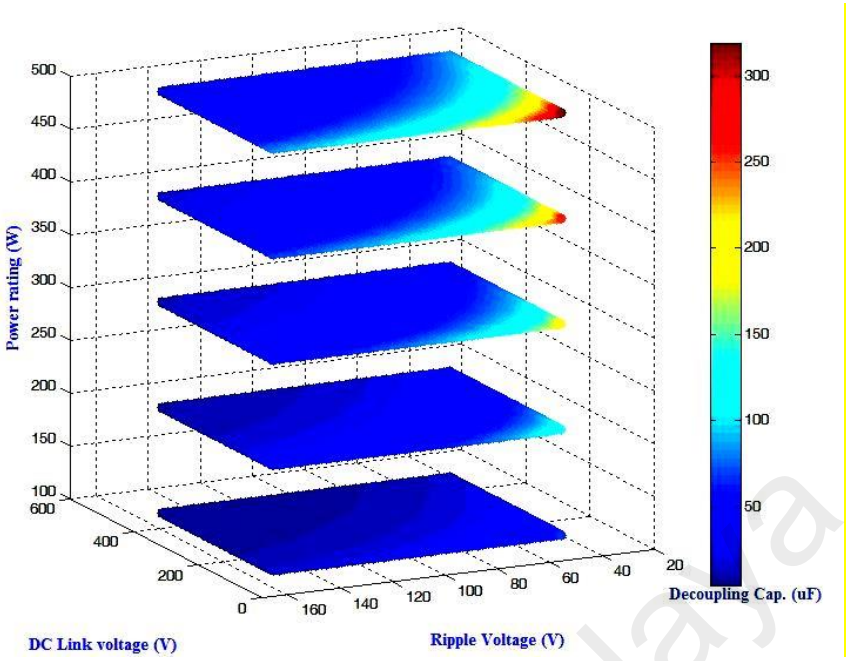

Figure 2.27: Selection of decoupling capacitor allowing high DC voltage across capacitor

2.6.4 Cost of Microinverters

The single-stage single flyback topology is less expensive because of the component count reduction for the DC–DC conversion stage. However, the voltage and current stress in the power semiconductor devices are high. The interleaved flyback topology is more costly than the single flyback, but the voltage and current stress are reduced in the power devices. The multi-stage topologies containing a DC–DC conversion stage are relatively more costly because they need additional components to boost the voltage at the grid level. However, the extended lifespan removes the recurring cost for the replacement of inverter units after their short lifespan.

2.6.5 Connecting With the Grid

The reactive power control is a vital issue in maintaining the voltage level of the grid. The injection of the reactive power maintaining MPPT at daytime and operation in compensation mode at nighttime surely increase the utilization of grid-tie PV microinverters. In a single-stage topology, the d-axis current can be controlled to vary

the PV voltage to achieve an MPP and the q-axis current can be controlled to inject the reactive power. In a multi-stage topology, the active power can be controlled in the DC–DC stage to obtain MPP, and the reactive power can be injected by controlling the q-axis current in the inverter stage.

PV systems have little impact on instantaneous voltage change because the fluctuations in the power output are comparatively slow. Only the unintended islanding function caused by the high sensitivity of the microinverters may experience instantaneous voltage change by the simultaneous disconnection of the PV systems. The harmonics generated in the output current of the isolated microinverter is not a matter of big concern because the topologies achieve less THD with a higher quality of power employing a proper control algorithm with the LC- or LCL-type grid filter.

2.7 Summary

This chapter firstly addressed the existing PV inverter topologies and mentioned the advantages of microinverter. Various types of single-stage and multi-stage microinverters have been scrutinized with respect to the predefined grid standards and performance criteria.

It has been found that the most of the existing hard-switched topologies suffers from poor efficiency performance. The topologies that use soft-switching mechanism are found to be more efficient as they have less power losses in the semiconductor devices. In particular, the flyback topologies with active-clamp techniques have been found to be a potential candidate for the PV microinverter.

The DCM and BCM control approaches is mainly adopted in most of the reviewed topologies. The CCM operation is not found to be a widespread control technique due to its control complexity. The hybrid operation of DCM and BCM operation is the recent

development in increasing the efficiency and reducing the control complexity of the microinverters.

However, the proper soft switching in active-clamp flyback circuit with hybrid operation is still a challenging task for the microinverters. This will reduce the switching losses and increases the efficiency. Hence, soft switching of active-clamp flyback topology with an advance hybrid-control operation is considered for the grid-tied PV system in this study.

CHAPTER 3: DESIGN OF THE PROPOSED TOPOLOGY

3.1 Introduction

In this dissertation, a new topology based on the flyback converter is proposed for the PV microinverter where an extra resonant inductor is inserted with the active clamp circuit, which ensures ZVS of the switches. The resonant capacitor across the main switch and the resonant inductor form a resonant circuit and the dead time between the switches can be varied to achieve the soft switching accurately. The active clamp circuit recycles the surge energy and reduces the voltage stress of the main switch. The auxiliary switch is also turned on at ZVS and therefore no extra switching losses occur due to the clamp circuit. The detailed steady-state analysis and mathematical modelling of the proposed single and double-stage microinverter is provided in the following sections. The chapter also explains the design considerations and proposed control algorithm based on the modelling of the microinverter. The loss breakdown of each component of the microinverter is provided to proof the achievability of the proposed design.

3.2 Single-Stage Microinverter

Figure 3.1 shows the circuit configuration of the proposed active-clamp resonant flyback microinverter. The circuit consists of a center-tapped flyback converter, an unfolding circuit, and an output filter. The proposed hybrid mode consists of DCM with variable negative current (DCMVNC) and BCM with variable negative current (BCMVNC) operation. The active clamp circuit is formed with a clamp switch S_c and a clamp capacitor C_c. A resonant inductor L_r is inserted in the converter to achieve ZVZCS operation in BCMVNC. C_r is the small capacitor added across the main switch that will decrease the rising slope of the drain-source voltage and attain the ZVS turn-

off of the switches. S_{s1} and S_{s2} do the unfolding operation and inject sinusoidal ac current in the grid.

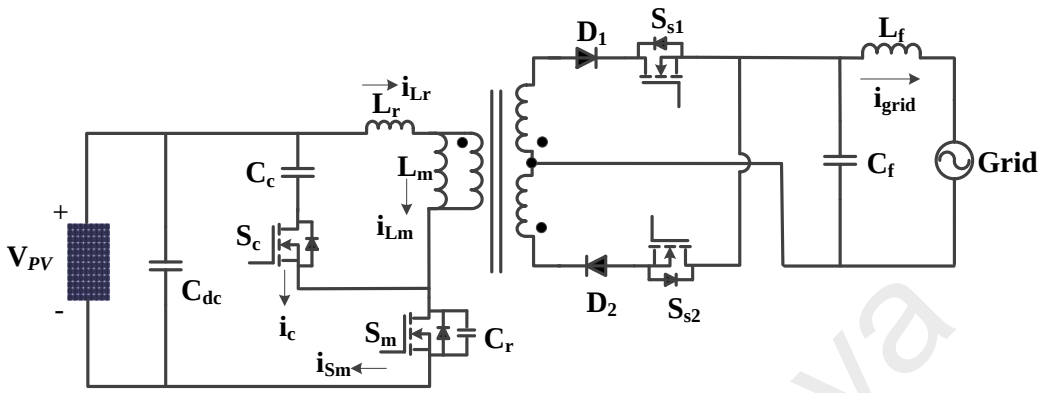

Figure 3.1: Circuit diagram of the proposed single-stage microinverter

3.2.1 Conventional and Proposed Hybrid Mode of Operation

Figure 3.2 illustrates the DCM and BCM region of a conventional hybrid mode operation of a flyback microinverter. The flyback converter is operated in DCM region in low power level and in BCM region for high power level. The main switch is only attaining the ZVS turn-on in the BCM region, but still cannot remove the voltage overshoot entirely. The switching operation in DCM region generates a high voltage and current stress, and increases the switching losses. The worst case arisen when the PV power level is reduced and consequently the DCM region is increased. Therefore, the microinverter operating in conventional hybrid mode shows the poor performance in low power operation.

The proposed hybrid operation is based on a modified DCM and BCM operation as shown in Figure 3.3. The proposed DCMVNC and BCMVNC operation achieve the ZVZCS turn-on and clamp the voltage overshoot of the main switch. Hence, the converter can be designed for high switching frequency operation with minimized switching losses.

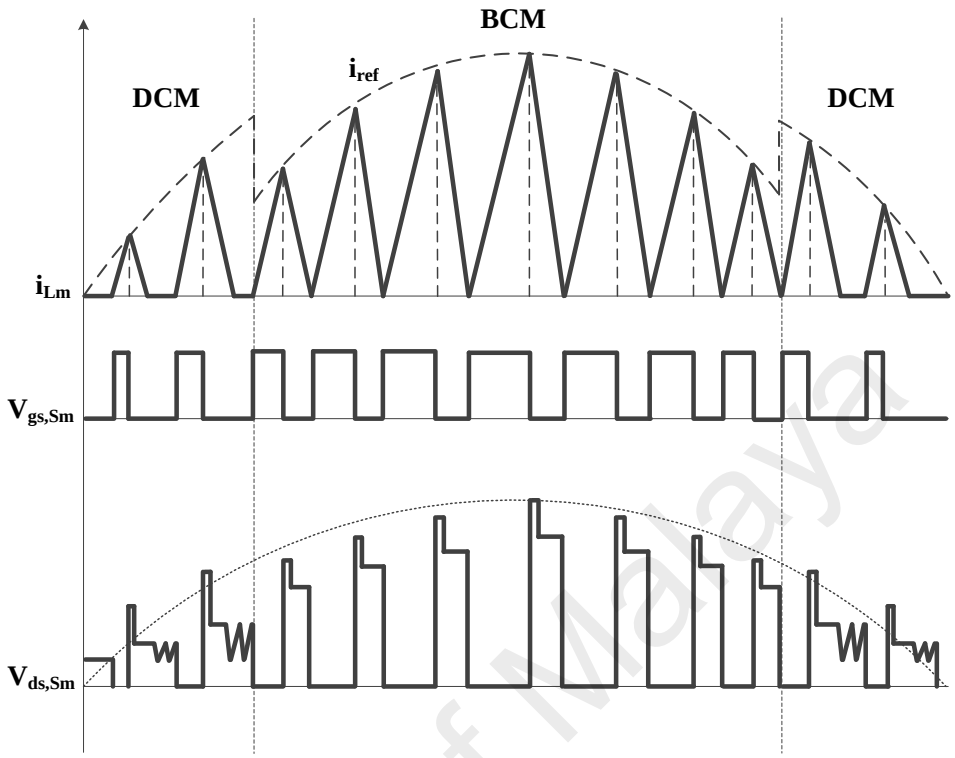

Figure 3.2: DCM and BCM region of a conventional hybrid mode operation

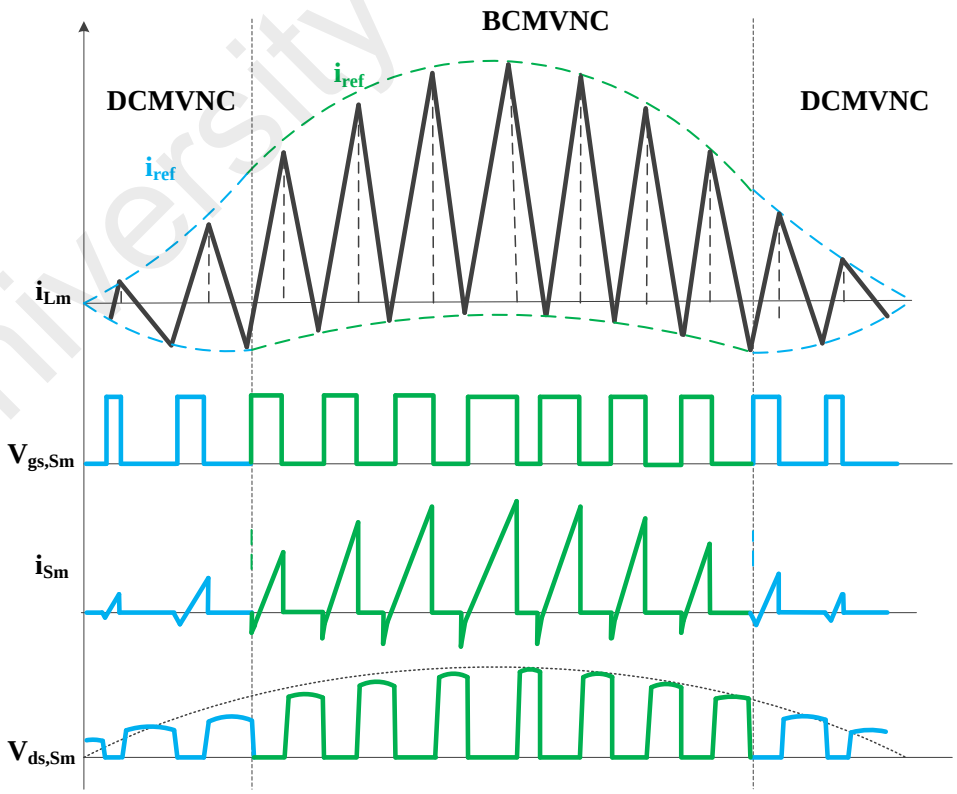

Figure 3.3: Proposed DCMVNC and BCMVNC hybrid operation

The reference signal $i_{ref}\ (\omega t)$ is to be designed for the implementation of proposed DCMVNC and BCMVNC operation. The reference signal controls the positive and negative peaks of the transformer magnetizing current by changing the duty cycle of the main switch of the converter. The current reference for conventional hybrid DCM and BCM operation is explained in [44] and the expression for the upper and lower limit for BCM is illustrated in [107]. The proposed hybrid operation combines these two features together and the upper and lower boundaries of the reference signal of DCMVNC and BCMVNC operation, $i_{ref\ (DCMVNC)}$ and $i_{ref\ (BCMVNC)}$, can be expressed as:

$$i_{ref}(\omega t) = \begin{cases} i_{ref\ (DCMVNC,\ Upper)} = \frac{2}{3}\sqrt{\frac{2P_oT_s}{L_m+L_r}}.Sin\ \omega t \\ i_{ref\ (DCMVNC,\ Lower)} = -\frac{1}{6}\sqrt{\frac{2P_oT_s}{L_m+L_r}}.Sin\ \omega t \\ i_{ref\ (BCMVNC,\ Upper)} = \frac{2}{3}\sqrt{\frac{2P_oT_s}{L_m+L_r}}.Sin\ \omega t \\ i_{ref\ (BCMVNC,\ Lower)} = -\frac{1}{6}\sqrt{\frac{2P_oT_s}{L_m+L_r}}.(\sqrt{2}-Sin\ \omega t) \end{cases} \quad (3.1)$$

3.2.2 Steady State Analysis of the Resonant Modes

The proposed hybrid strategy is operated with three resonant modes in a single switching cycle while achieving the ZVZCS turn-on and ZVS turn-off of the high frequency switch. The magnetizing inductance L_m is larger than the resonant inductance L_r and the energy stored in L_r is greater than the energy stored in C_r to ensure the soft-switching operation for both S_m and S_c. Since the switching frequency of the flyback converter is much higher than the line frequency, the grid voltage and current are assumed constant in a switching cycle. The equivalent circuits and the key waveforms of the resonant modes in a single switching cycle of the proposed microinverter are illustrated in Figure 3.4 and Figure 3.5 respectively. The steady state analysis of the modes of operation is described in the following.

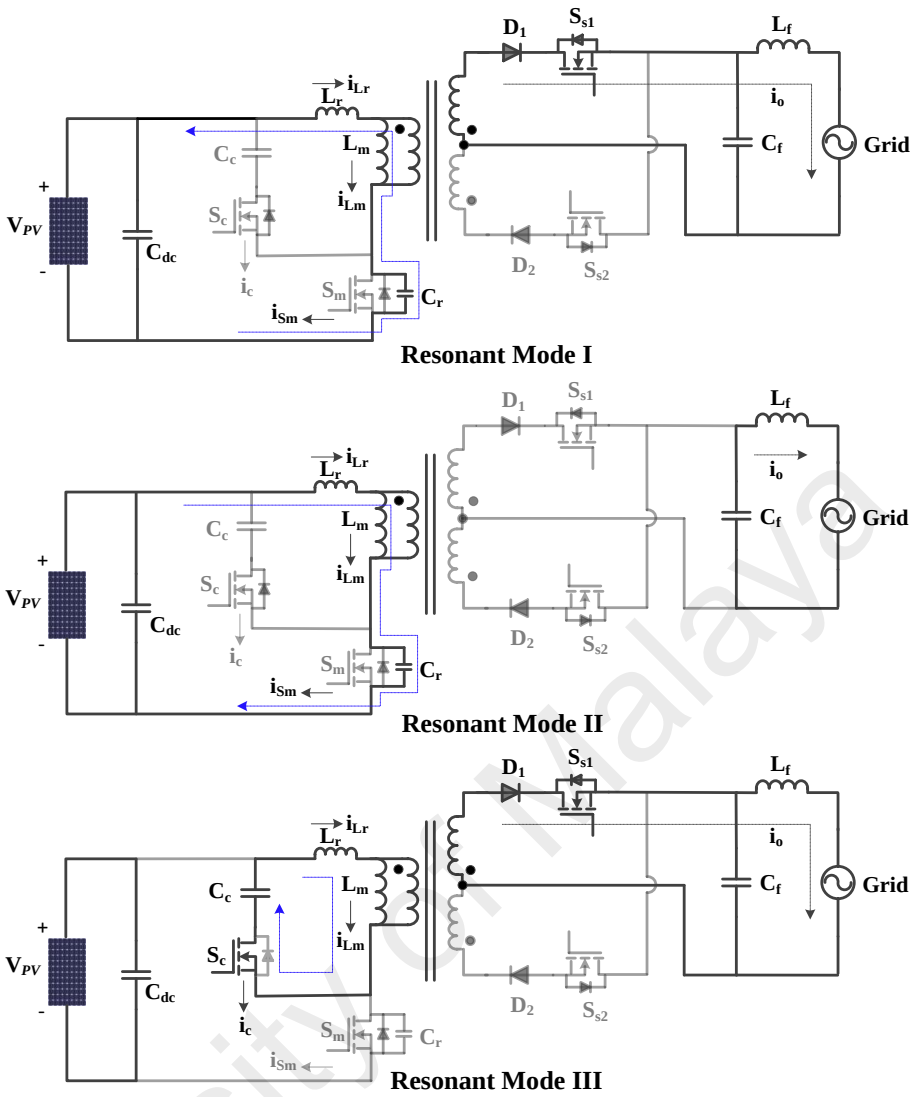

Figure 3.4: Equivalent circuit of the resonant modes

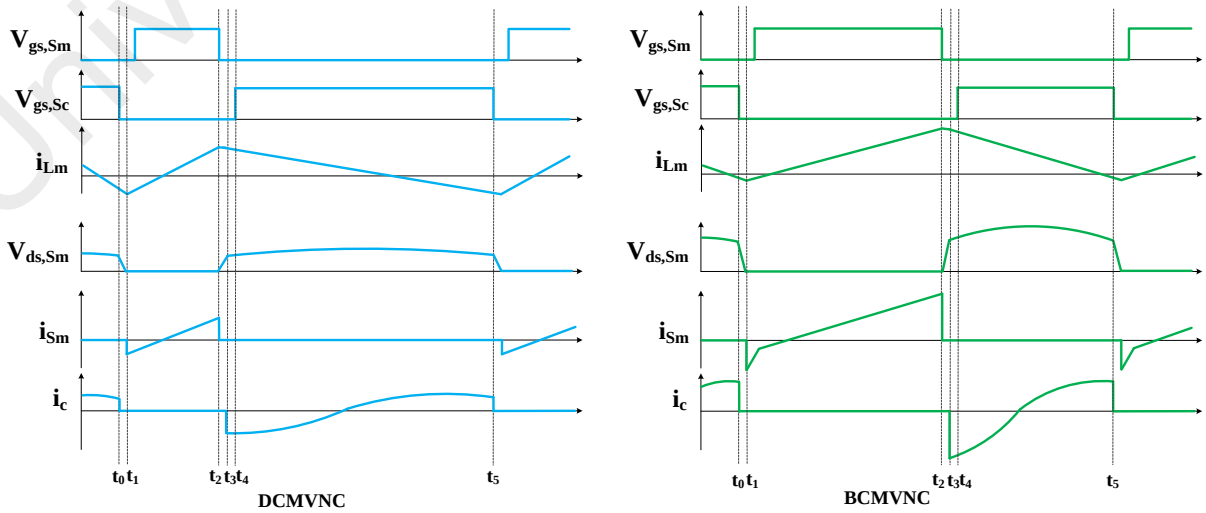

Figure 3.5: Key waveforms of the resonant modes

Resonant Mode I [t_0-t_1]: The first resonant operation occurs before the turn-on of the main switch. This mode creates a platform in achieving ZVZCS turn-on of the main switch. At the beginning of this interval, the clamp switch S_c is turned off and the resonant current flows through the parasitic capacitance of the main switch S_m. The negative resonant current i_{Lr} discharges the resonant capacitor C_r. The drain-source voltage $V_{ds,Sm}$ of the main switch and resonant inductor current i_{Lr} are expressed as

$$V_{ds,Sm}(t) = V_{PV} + V_{grid}/n + (V_{Cr}(t_0) - V_{PV} - V_{grid}/n)\, cos(\omega_{r1}(t - t_0)) + i_{Lr}(t_0) Z_{i1} \sin(\omega_{r1}(t - t_0)) \quad (3.2)$$

$$i_{Lr}(t) = i_{Lr}(t_0) \cos\big(\omega_{r1}(t - t_0)\big) + \frac{(V_{Cr}(t_0) - V_{PV} - V_{grid}/n)}{Z_{i1}} sin(\omega_{r1}(t - t_0)) \quad (3.3)$$

Where resonant frequency, $\omega_{r1} = 1/\sqrt{C_r L_r)}$ and characteristic impedance, $Z_{i1} = \sqrt{L_r/C_r}$

The time interval of this stage is very small. Therefore, the voltage and current can be expressed as

$$V_{ds,Sm}(t) \approx V_{Cr}(t_0) + \frac{i_{Lr}(t_0)}{C_r}(t - t_0)) \quad (3.4)$$

$$i_{Lr}(t) \approx i_{Lr}(t_0) - \frac{V_{Cr}(t_0) - (V_{PV} + V_{grid}/n)}{L_r}(t - t_0) \quad (3.5)$$

To ensure the ZVZCS turn-on of the main switch S_m, the drain-source voltage $V_{ds,Sm}$ should reach zero at the end of this stage. Therefore, the energy stored in the resonant capacitor C_r must be less than the energy stored in resonant inductor L_r. The following condition must hold

$$\frac{1}{2} C_r (V_{PV} + V_{grid}/n)^2 \leq \frac{1}{2} {i_{Lr\_pk}}^2 L_r \quad (3.6)$$

This interval ends when $V_{ds,Sm} = 0$ and the main switch is turned on at the next stage at ZVZCS condition.

Resonant Mode II [t_2-t_3]: The second resonant mode starts at time $t=t_2$, when the main switch S_m is turned off. The magnetizing current flowing through the primary side charges the resonant capacitor C_r. The ZVS turn-off of the main switch is achieved and the drain-source voltage $V_{ds,Sm}$ rises slowly due to the charging of the resonant capacitor. The circuit composed of L_r, L_m and C_r forms a LLC resonant tank. The voltage across the main switch and the current through the LLC tank circuit are expressed as

$$V_{ds,Sm}(t) = V_{PV}(1 - \cos(\omega_{r2}(t - t_2))) + i_{Lr}(t_2)Z_{i2}\sin(\omega_{r2}(t - t_2)) \quad (3.7)$$

$$i_{Lr}(t) = i_{Lm}(t) = i_{Lm}(t_2)\cos(\omega_{r2}(t - t_2)) + \frac{V_{PV}}{Z_{i2}}\sin(\omega_{r2}(t - t_2)) \quad (3.8)$$

where resonant frequency, $\omega_{r2} = 1/\sqrt{C_r(L_m + L_r)}$, and characteristic impedance, $Z_{i2} = \sqrt{(L_m + L_r)/C_r}$

Since the resonant capacitor C_r is very small, it is charged quickly and the time interval is also very short. This mode ends at time t_3, when the voltage across the resonant capacitor reaches to its maximum value $V_{PV} + V_{grid}/n$. The resonant capacitor voltage and the primary current at the end of this mode can be approximately given as

$$V_{ds,Sm}(t_3) \approx i_{Lr}(t_2)Z_{i2}.\omega_{r1}(t_3 - t_2) = i_{Lr}(t_2)(t_3 - t_2)/C_r = V_{PV} + V_{grid}/n \quad (3.9)$$

$$i_{Lr}(t_3) = i_{Lm}(t_3) \approx i_{Lm}(t_2).1 + \frac{V_{PV}}{Z_{i2}}.\omega_{r2}(t_3 - t_2) \approx i_{Lm}(t_2) \quad (3.10)$$

Resonant Mode III [t_4-t_5]: At time $t=t_4$, the clamp switch S_c is turned on. To achieve ZVS, the clamp switch is turned on before the resonant current changes its direction. The energy stored in the magnetizing inductance is transferred to the grid through the secondary switch. The resonant current and magnetizing current is given as

$$i_{Lr}(t) = i_{Lr}(t_4)\cos\big(\omega_{r3}(t - t_4)\big) - \frac{V_{Cc}(t_4) - V_{grid}/n}{Z_{i3}}\sin(\omega_{r3}(t - t_4))$$

$$\approx i_{Lr}(t_4)\cos\big(\omega_{r3}(t - t_4)\big) - \frac{V_{grid}\sqrt{L_r C_c}}{nL_m}\sin(\omega_{r3}(t - t_4)) \quad (3.11)$$

$$i_{Lm}(t) = i_{Lm}(t_4) - \frac{V_{grid}}{nL_m}(t - t_4) \quad (3.12)$$

where, resonant frequency, $\omega_{r3} = 1/\sqrt{L_r C_c}$ and characteristic impedance, $Z_{i3} = \sqrt{L_r/C_c}$

3.2.3 Design Consideration

This section provides the guidelines based on the analysis of the steady state operation to make the design procedure more clear. These are the selection of the transformer magnetizing inductance, the resonant components, the power devices, and the control issues.

3.2.3.1 Magnetizing inductance of flyback converter (L_m)

The power transfer capability of a flyback converter in a certain operating frequency depends on the value of the magnetizing inductance L_m. The design of the L_m is a very crucial part in the proposed hybrid mode of operation of the microinverter. A lower value of L_m will enter in the DCM region unnecessarily and a higher value would enter in the CCM region. The value of L_m should have a critical value so that the magnetizing current i_{Lm} becomes zero and reached the negative reference current in both modes within each switching period T_s. Therefore, the current and voltage stress is minimum throughout the line cycle. During the ON time of primary switch S_m, the energy E_{Lm} is stored in the magnetizing inductance and is expressed as

$$E_{Lm} = \frac{1}{2}L_m(i_{Lm\_pk})^2 = \frac{1}{2}L_m\left(\frac{V_{PV}}{L_m+L_r}(DT_s) - \frac{\sqrt{2}}{6}\sqrt{\frac{2P_oT_s}{L_m+L_r}}\right)^2 \quad (3.13)$$

For a lossless system, the averaged input power P_{PV} is equal to the averaged output power P_o.

$$P_{PV(average)} = V_{PV}I_{PV} = P_o \quad (3.14)$$

The averaged input DC photovoltaic current can be obtained as

$$I_{PV} = \frac{1}{2}\left(\frac{V_{PV}}{L_m+L_r}(DT_s) - \frac{\sqrt{2}}{6}\sqrt{\frac{2P_oT_s}{L_m+L_r}}\right)(DT_s)(\frac{1}{T_s}) \tag{3.15}$$

Now equating the PV power with the grid power

$$V_{PV}I_{PV} = \frac{1}{2}\left(\frac{{V_{PV}}^2T_s}{L_m+L_r}\left(\frac{V_{grid(pk)}}{nV_{PV}+V_{grid(pk)}}\right)^2 - \frac{\sqrt{2}V_{PV}.\ V_{grid(pk)}}{6\ (nV_{PV}+V_{grid(pk)})}\sqrt{\frac{2P_oT_s}{L_m+L_r}}\right) = P_o \tag{3.16}$$

From (3.16), the magnetizing inductance can be obtained as

$$L_m = \frac{A+\sqrt{A^2-B}}{8{P_o}^2} - L_r \tag{3.17}$$

where, $A = \frac{37}{9}\ P_o{V_{PV}}^2T_s\left(\frac{V_{grid(pk)}}{nV_{PV}+V_{grid(pk)}}\right)^2$ and $B = 16\ {P_o}^2\left[{V_{PV}}^2T_s\left(\frac{V_{grid(pk)}}{nV_{PV}+V_{grid(pk)}}\right)^2\right]^2$

The above equation clearly shows that the magnetizing inductance mainly depends on the switching frequency and no. of turn's ratio of the flyback converter. The value of the magnetizing inductance with different switching frequency and turn's ratio is presented in Figure 3.6. It has been observed that the magnetizing inductance of the flyback converter decreases with the increasing of switching frequency and no. of turn's ratio. However, there is a trade-off between the switching frequency and the turn-off losses of the switches of proposed microinverter. Although ZVS turn-on of the switches is achieved, the drain-source voltage and current are overlapped for a short duration during the turn-off delay time (t_{d_off}) of the MOSFET. Hence, the turn-off loss is increased with the increase of switching frequency. This loss is more for the switch that have more turn-off delay time, t_{d_off}. From Figure 3.6, the optimized switching frequency, at which the magnetizing inductance and the turn-off loss remains low, is chosen as 80 kHz and the turn's ratio is taken as n=3. Hence, the magnetizing inductance L_m is found to be 14µH for the proposed flyback converter.

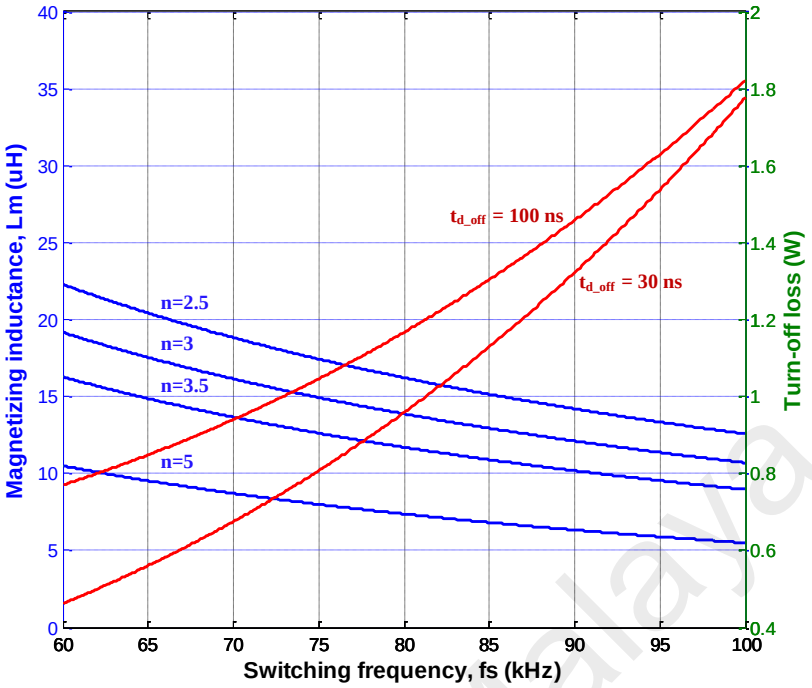

Figure 3.6: Selection of the magnetizing inductance of flyback converter

3.2.3.2 Resonant inductor and capacitor (L_r, C_r)

In order to turn-on the main switch S_m in zero voltage condition, the resonant capacitor should be discharged fully through the resonant circuit in the first resonant mode. Hence, the resonant inductor can be derived from equation (3.6) as

$$L_r > \frac{C_r(V_{PV}+V_{grid}/n)^2}{{i_{Lr\_pk}}^2} \tag{3.18}$$

The effect of the L_r to the envelope of magnetizing current is presented in Figure 3.7. It is shown that the variable negative current is minimum in the BCM region when $L_r=0$ and the current peak is high. The proper ZVZCS is not achieved in this region. The variable negative current increases with the increasing of resonant inductor L_r and soft switching can be achieved throughout the BCM region. Moreover, the envelope of the current peak is also decreased with the increase of resonant inductor.

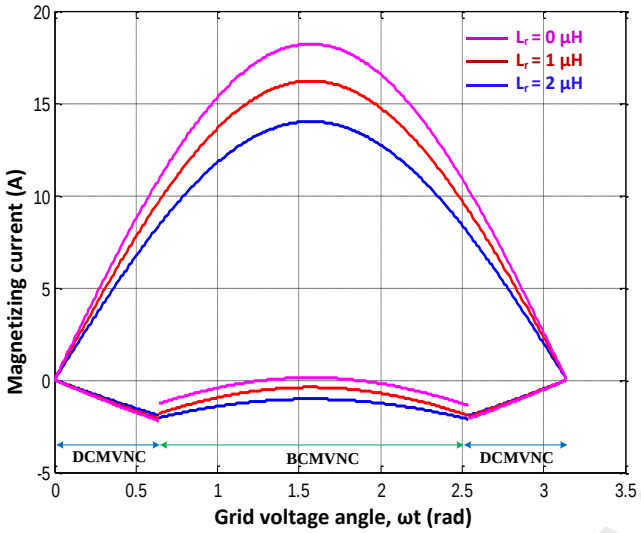

Figure 3.7: Envelope of magnetizing current with different value of L_r

Since the main switch S_m is operating in the reverse direction for a very short duration of time, the reverse conduction loss of the main switch is negligible as shown in Figure 3.8. However, the conduction loss of the resonant inductor L_r is increased with the increase of its value. The value of the resonant inductor is optimized among the switching and conduction loss of the main and clamp switch as well as the conduction loss of L_r. As shown in Figure 3.8, the loss is minimized for the higher value of resonant inductor (2µH to 4µH). Hence, 2µH is taken due to its robustness and low cost.

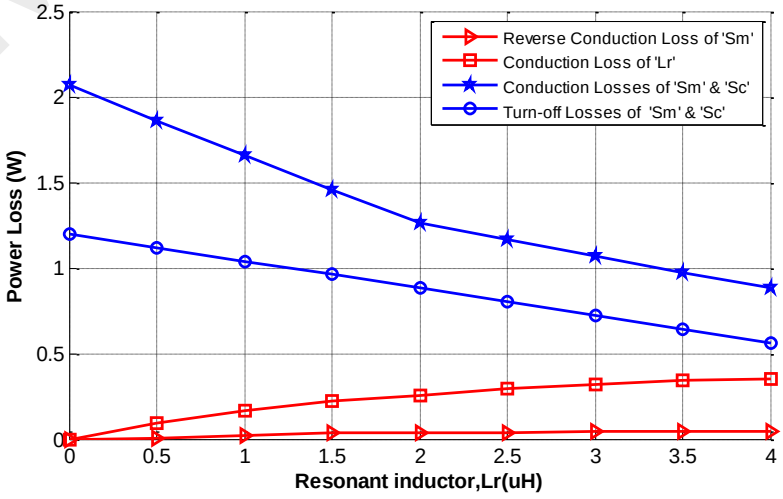

Figure 3.8: Selection of resonant inductor L_r

The total capacitance that forms across the main switch of the flyback converter is the parallel combination of the resonant capacitance C_r and MOSFET output capacitance C_{oss_sm}, and is given as

$$C_{total} = C_r \| C_{oss\_Sm} \tag{3.19}$$

The value of the total capacitance C_{total} depends on the maximum allowable dead time T_d and can be obtained as

$$C_{total} = \frac{4{T_d}^2}{\pi^2 L_r} \tag{3.20}$$

Hence, the resonant capacitor can be expressed as

$$C_r = \frac{4{T_d}^2}{\pi^2 L_r} - C_{oss\_Sm} \tag{3.21}$$

3.2.3.3 Active clamp capacitor (C_c)

The clamp capacitor C_c and resonant inductor L_r will resonane at the third resonant mode. This resonant period is approximately equal to the maximum turn-off time of the main switch.

$$2\pi\sqrt{L_r C_c} \approx (1 - D_{min})T_s \tag{3.22}$$

The clamp capacitance is obtained as,

$$C_c \approx \frac{((1-D_{min})T_s)^2}{4\pi^2 L_r} \tag{3.23}$$

The voltage stress on the clamp capacitor is maximum when the main switch is turned off and clamp switch is turned on, and the maximum stress is expressed as

$$V_{Cc\_max} = V_{PV}\frac{D_{max}}{1-D_{max}} \tag{3.24}$$

3.2.3.4 Power semiconductor devices

The voltage stress across the main switch S_m is less when active-clamp circuit is used. The energy in the leakage inductor or resonant inductor is absorbed by the clamp capacitor C_c. Hence, the voltage spike across S_m is reduced. The maximum voltage stress across the primary switch is given as

$$V_{Sm\_max} = V_{PV} + V_{Cc\_max} = \frac{V_{PV}}{1-D_{max}} = V_{PV} + \frac{V_{grid}}{n} + V_{spike} \tag{3.25}$$

where, the spike voltage V_{spike} can be expressed as

$$V_{spike} = i_{Sm\_pk}\sqrt{\frac{L_r}{C_r+\frac{C_c.C_r}{C_c+C_r}}} \tag{3.26}$$

From the above equation, it is clear that the presence of clamp capacitor reduced the voltage spike across the main switch S_m. The peak current of the main switch is given as

$$i_{Sm\_pk} = \frac{P_{PV\_max}}{V_{PV\_min}.D_{max}} \tag{3.27}$$

The root mean square (rms) current of S_m is

$$i_{Sm\_rms} = i_{Sm\_pk}\sqrt{D_{max}/3} \tag{3.28}$$

The voltage and current stress of the secondary switches are expressed as

$$V_{Ss1\_max} = V_{Ss2\_max} = nV_{PV} + V_{grid} \tag{3.29}$$

$$i_{Ss1\_max} = i_{Ss2\_max} = \frac{2P_o}{V_{grid}(1-D_{max})} \tag{3.30}$$

3.2.4 Proposed Control for single-stage microinverter

To inject a sinusoidal output current in the grid, the primary winding current needs to be controlled to follow the reference current of the proposed DCMVNC and BCMVNC hybrid operation. The main and clamp switch are driven in such a way that there should

be a dead time between the stages. The dead time must be less than the resonant period caused by the resonant inductor and capacitor so that the soft switching of the switches can be achieved. The control block of the proposed resonant microinverter is proposed in Figure 3.9. The duty cycles of the main switch and clamp switch are generated by comparing the main switch current with the reference signal.

As shown in the Figure 3.9, the reference current for the proposed DCMVNC and BCMVNC operation is generated from comparing the grid current envelope and the maximum power point voltage of the PV. The MPPT block provides the voltage and current V_{PV}^* and I_{PV}^*. The reference signal is produced comparing the power level of the PV panel. If the power level is low, the DCM region will increase with a variable negative current as derived in equation (3.1). If the power level is high, the BCM region will increase maintaining a variable negative current. Then the switch current is compared with the shaped reference signal and required duty cycle is generated for main- and clamp-switch.

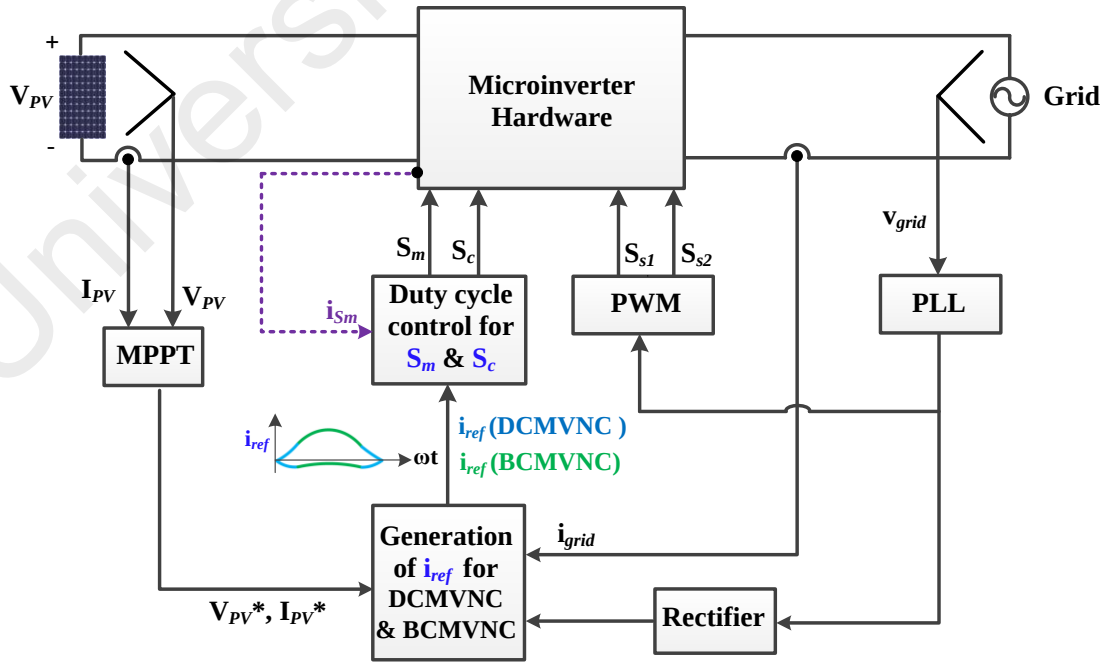

Figure 3.9: Control block diagram of the proposed single-stage microinverter

The flowchart of the controlling of duty cycle of main and clamp switch is illustrated in Figure 3.10. The selection of the DCMVNC or BCMVNC depends on the instantaneous power level. The change of the mode from one to another is related with critical main switch current i_{Sm_cri}. If the main switch current is less than the critical current, i.e. $i_{Sm} < i_{Sm\_cri}$ the mode is swapped to DCMVNC operation. Similarly, if the main switch current is greater than the critical current, i.e. $i_{Sm} \geq i_{Sm\_cri}$ the mode is swapped to BCMVNC operation. Then the increasing or decreasing of the duty cycle depends on the phase of the reference current. If the extant phase is less than the phase at peak magnitude of reference current, the duty cycle will be increased in the next step. Besides, while it reaches at the phase on peak reference current the duty cycle will be decreased. The secondary side switches are controlled to operate at same frequency of grid current.

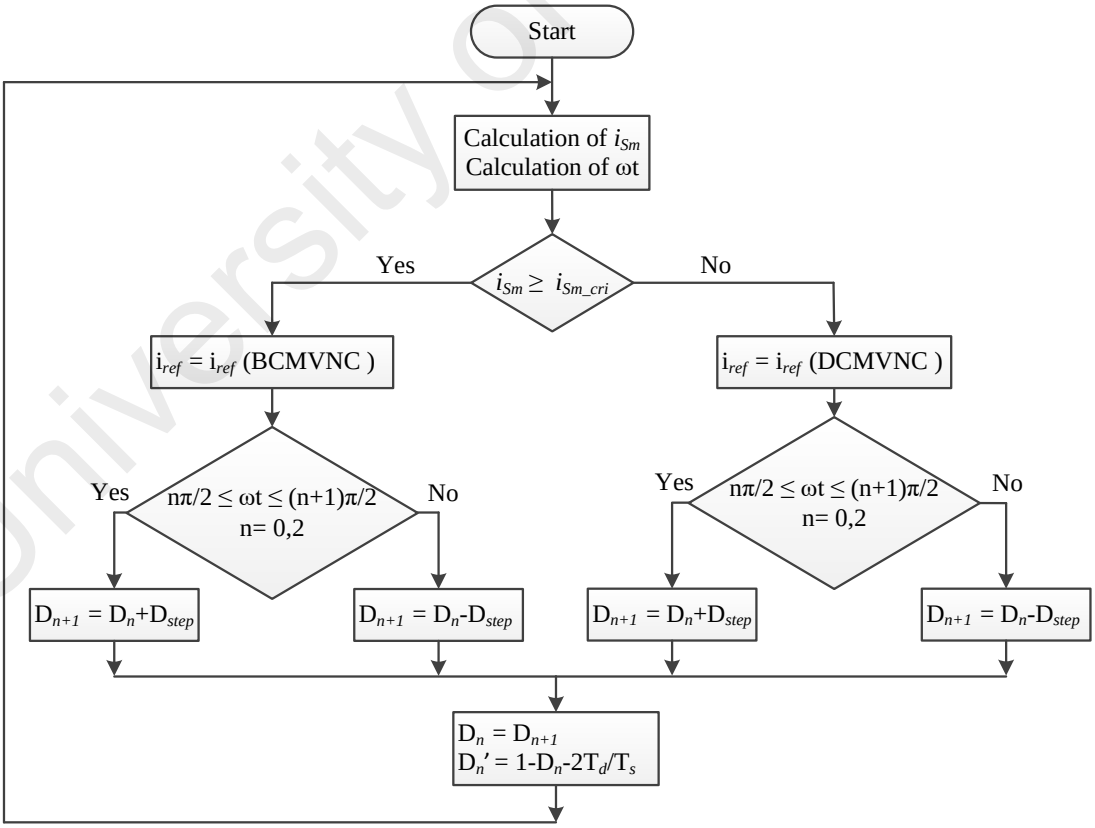

Figure 3.10: Diagram of duty cycle control of hybrid operation

3.2.5 Loss Analysis

The analysis of the various losses in the flyback converter and power devices of the proposed microinverter provides acuity in measuring the efficiency. The loss components for a 250 W microinverter can be calculated as follows.

3.2.5.1 Core and copper losses of flyback converter

A PQ32/30 ferrite core is chosen to build the flyback converter. The core loss of the converter can be approximately expressed as [86]

$$P_{core} = \left[K_{fe}(\Delta B)^{\beta} A_c l_m\right] = \left[K_{fe}\left(\frac{V_{PV} D_{max} T_s}{2N_p A_c}\right)^{\beta} (A_c l_m)\right] = 2.1\ W \tag{3.31}$$

The rated current, I_{rms} through the flyback converter is 5.7 A and the winding resistance R_{wire} is 0.01 ohm. Hence, the copper loss of the winding is

$$P_{copper} = {I_{rms}}^2 R_{wire} = 0.33\ W \tag{3.32}$$

3.2.5.2 Switching and conduction losses of power semiconductor devices

The switching losses are mainly occurring due to the high switching frequency in the primary side main and auxiliary switches. The switching losses in the secondary switches are negligible. Due to ZVS operation in the primary side switches, the turn ON loss are insignificant. Hence, the switching losses of the main and auxiliary switches take place because of the turn OFF losses of the MOSFET, which is approximately given as

$$P_{sw,Sm} = V_{ds,Sm} I_{Sm} \left(\frac{t_{d\_off} + t_f}{2T_s}\right) = 0.36\ W \tag{3.33}$$

$$P_{sw,Sc} \approx= V_{ds,Sc} I_{Sc} \left(\frac{t_{d\_off} + t_f}{2T_s}\right) = \ 0.47\ W \tag{3.34}$$

where, $V_{ds,Sm}$ = $V_{ds,Sm}$ = 60 V, I_{Sm} = 5.7 A, I_{Sc} = 6 A, t_{d_off} = 23 ns and t_f = 6 ns.

The conduction losses occur in both primary and secondary side switches, which is expressed as

$$P_{cond\_Sm} = \frac{1}{3} R_{ds\_on} . {i_{sm\_pk}}^2 . D = 0.68\ W \quad (3.35)$$

$$P_{cond\_Sc} = \frac{1}{3} R_{ds\_on} . {i_{sc\_pk}}^2 = 0.95\ W \quad (3.36)$$

$$P_{cond\_Ss1} \approx P_{cond\_Ss2} = \frac{1}{2} R_{ds\_on} . {i_{sec\_rms}}^2 = 0.21\ W \quad (3.37)$$

where, R_{ds_on} = 0.02 ohm, i_{sm_pk} = 14.3 A, i_{sc_pk} = 16 A and i_{sec_rms} = 2.3 A

Total losses of switches can be found as

$$P_{total} = P_{sw} + P_{cond} = 2.67\ W \quad (3.38)$$

3.3 Double-Stage Microinverter

Figure 3.11 shows the circuit configuration of the proposed resonant flyback microinverter. The circuit is composed of a resonant active-clamp flyback converter in the DC-DC stage and a resonant full-bridge inverter in the DC-AC stage. The DC link capacitor is placed at the output of DC-DC converter. The output voltage and current are taken from the inverter and connected with the grid. The details operations of the two stages are described in the following.

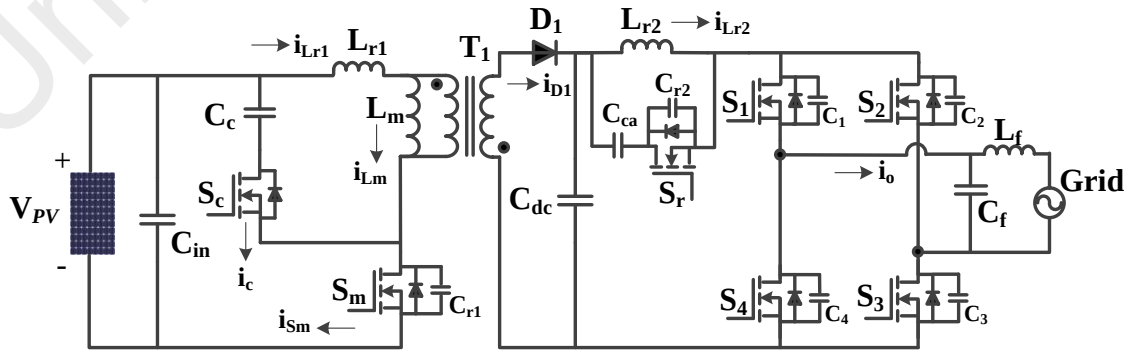

Figure 3.11: Circuit diagram of the proposed microinverter

3.3.1 Resonant flyback DC-DC converter

The DC-DC converter consists of an active-clamp resonant circuit with the flyback converter. The resonant inductance L_{r1} is the sum of transformer leakage inductance and external inductance added to form the resonant circuit. C_{r1} is the parallel combination of an additional capacitor and MOSFET parasitic capacitor. The clamp-switch S_c with a clamp-capacitor C_c forms an active-clamp circuit that limits the voltage stress of the switches and assists to achieve ZVS operation for both main switch S_m and clamp-switch S_c. The rectifier diode D_1 is placed in the secondary of the transformer T_1. The diode is turned on at zero current switching (ZCS) while the main switch is turned off. The operating modes and associated key waveforms in a single switching cycle of the flyback converter are represented in Figure 3.12 and Figure 3.13, respectively. The steady state analysis of the modes of operation is described in the following.

Mode 1 (t_0-t_1): In this mode, the main switch S_m is remaining on and the clamp-switch S_c is remaining off. The input PV voltage is applied to the flyback converter, and the energy is stored in the primary winding of the transformer. The primary side current increases until the end of this mode and is expressed as following:

$$i_{Sm}(t) = i_{Lr1}(t) = i_{Lm}(t) = \frac{V_{PV}}{L_m + L_{r1}}(t - t_0) \tag{3.39}$$

The primary magnetizing current keeps ramping up until the main switch is turned off at $t = t_1$. The peak value of the primary side current is given as

$$i_{Sm\_pk} = i_{Lr1\_pk} = i_{Lm\_pk} = \frac{V_{PV}}{L_m + L_{r1}}(t_1 - t_0) = \frac{V_{PV}}{L_m + L_{r1}}(DT_s) \tag{3.40}$$

This mode ends when the main switch current reaches to its peak value and the switch is turned off at zero voltage condition of the drain-source voltage. The rectifier

diode D_1 is remaining off, and the inverter is fed from the output capacitor. The DC current that flows from the photovoltaic module is expressed as

$$I_{PV} = \frac{(L_m + L_{r1})}{2V_{PV}T_s} (i_{Sm\_pk})^2 \quad (3.41)$$

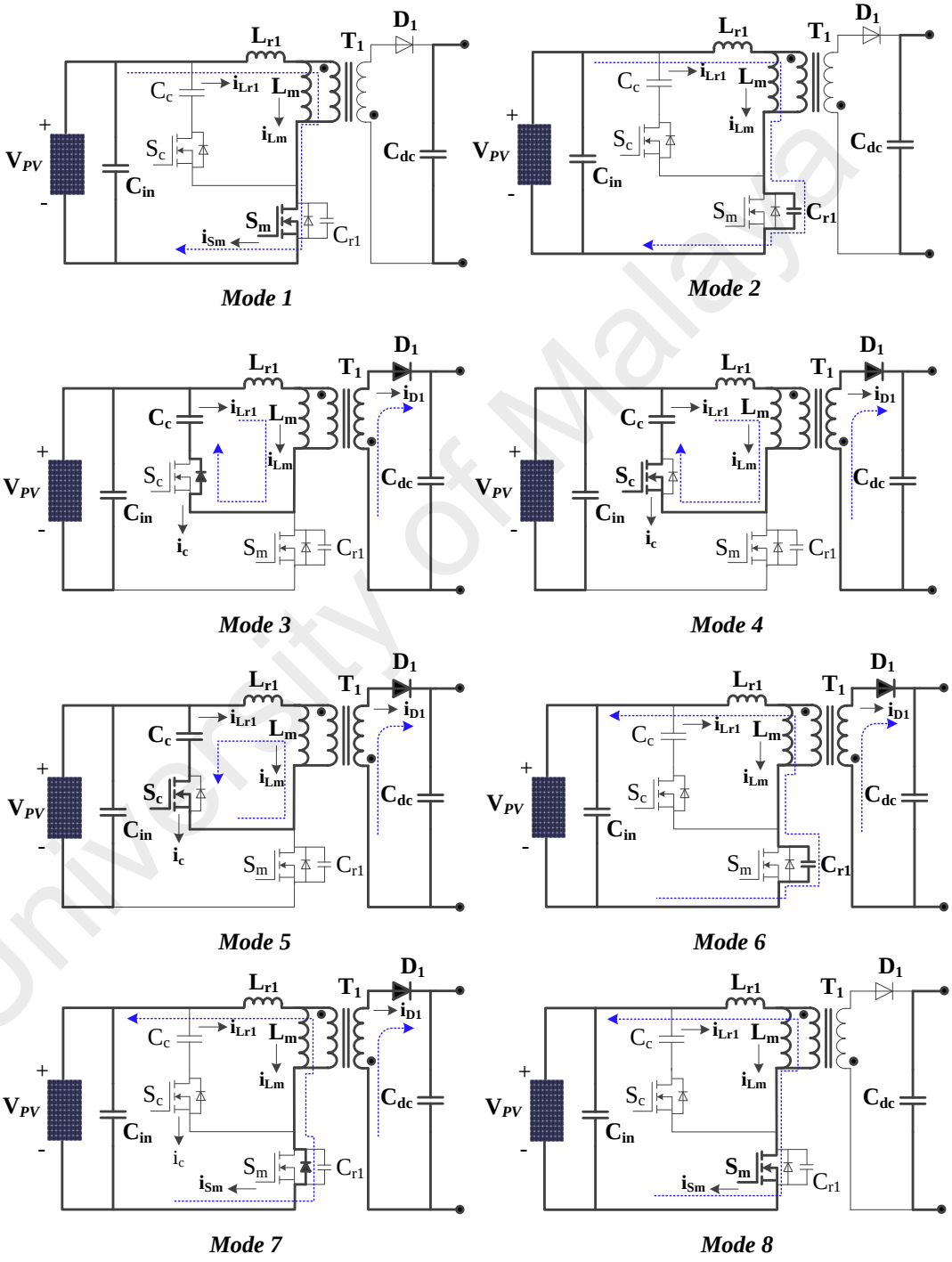

Figure 3.12: Operating modes of the proposed double-stage flyback converter

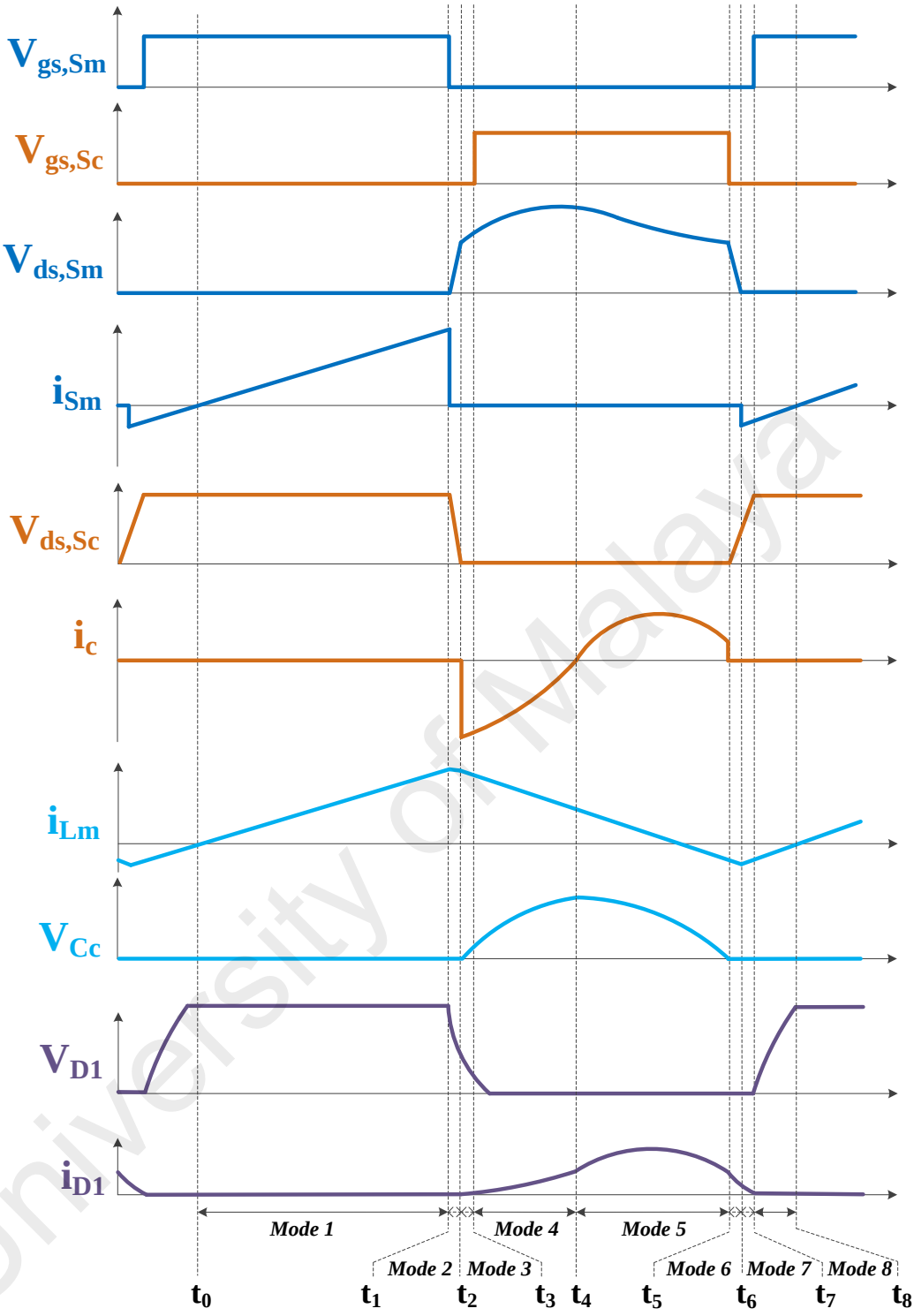

Figure 3.13: Key waveforms of the flyback converter in a single switching cycle

Mode 2 (t_1-t_2): This mode starts at time t_1 when the main switch S_m is turned off. The magnetizing current flowing through the primary side of the converter charges the resonant capacitor C_{r1}. The drain-source voltage $V_{ds,Sm}$ of the main switch rises slowly due to the charging of the resonant capacitor. The circuit composed of L_{r1}, L_m and C_{r1}

forms a LLC resonant tank. The voltage across the resonant capacitor and the current through the LLC tank circuit are expressed as

$$V_{Cr1}(t) = V_{ds,Sm}(t) = V_{PV}(1 - \cos(\omega_{r1}(t - t_1))) + i_{Lr1}(t_1)Z_{i1}\sin(\omega_{r1}(t - t_1)) \quad (3.42)$$

$$i_{Lr1}(t) = i_{Lm}(t) = i_{Lm}(t_1)\cos(\omega_{r1}(t - t_1)) + \frac{V_{PV}}{Z_{i1}}\sin(\omega_{r1}(t - t_1)) \quad (3.43)$$

where, resonant frequency, $\omega_{r1} = 1/\sqrt{C_{r1}(L_m + L_{r1})}$, and characteristic impedance, $Z_{i1} = \sqrt{(L_m + L_{r1})/C_{r1}}$

Since the resonant capacitor, C_{r1} is very small; it is charged quickly and the time interval is very short. The output diode is remaining off during the mode. This mode ends at time t_2, when the voltage across the main switch equals the PV voltage and clamp capacitor voltage, i.e. $V_{ds,Sm} = V_{PV} + V_{dc}/n$.

Mode 3 (t_2-t_3): This mode starts when the voltage $V_{ds,Sm}$ reaches $(V_{PV} + V_{dc}/n)$ and the antiparallel diode of the clamp-switch S_c turns on. The rectifier diode D_1 is turned on and the energy stored in the magnetizing inductor starts releasing and is delivered to the output. The clamp-capacitor C_c, resonant inductor L_{r1} and magnetizing inductor L_m are resonant in this interval. The resonant inductor current i_{Lr1} passes through the antiparallel diode of the clamp-switch and charges the clamp-capacitor C_c. The current i_{Lr1} and the clamp-capacitor voltage V_{Cc} are expressed as

$$i_{Lr1}(t) = -i_c(t) = i_{Lr1}(t_2)\cos(\omega_{r2}(t - t_2)) - \frac{V_{dc}/n}{Z_{i2}}\sin(\omega_{r2}(t - t_2)) \quad (3.44)$$

$$V_{Cc}(t) = \frac{V_{dc}}{n}\cos(\omega_{r2}(t - t_2)) + i_{Lr}(t_2)Z_{i2}\sin(\omega_{r2}(t - t_2)) \quad (3.45)$$

where $\omega_{r2} = 1/\sqrt{C_c(L_m + L_{r1})}$ and $Z_{i2} = \sqrt{(L_m + L_{r1})/C_c}$

Since the interval of this period is very small, i_{Lr1} and V_{Cc} can be expressed as

$$i_{Lr1}(t) = -i_c(t) \approx i_{Lr1}(t_2) - \frac{V_{dc}}{n(L_m + L_{r1})}(t - t_2) \quad (3.46)$$

$$V_{Cc}(t) \approx \frac{V_{dc}}{n} + \frac{i_{Lr1}(t_2)}{C_c}(t - t_2) \quad (3.47)$$

This mode ends at time $t=t_3$ when the voltage of the clamp-capacitor equals $\frac{V_{dc}(L_m + L_{r1})}{nL_m}$.

Mode 4 (t_3-t_4): At time $t=t_3$, the drain-source voltage of the clamp-switch S_c is zero and the clamp-switch is turned on to achieve ZVS. The clamp-capacitor C_c and resonant inductor L_{r1} become resonant in this interval. The magnetizing current is decreasing, and the energy is transferred to the output circuit through the rectifier diode *D*. The resonant current passes through the clamp-switch and is expressed as

$$i_{Lr1}(t) = -i_c(t) = i_{Lr1}(t_3)\cos\big(\omega_{r3}(t - t_3)\big) - \frac{V_{Cc}(t_3) - V_{dc}/n}{Z_{i3}} sin(\omega_{r3}(t - t_3))$$

$$\approx i_{Lr1}(t_3)\cos\big(\omega_{r3}(t - t_3)\big) - \frac{V_{dc}\sqrt{L_{r1}C_c}}{nL_m} sin(\omega_{r3}(t - t_3)) \quad (3.48)$$

where $\omega_{r3} = 1/\sqrt{C_c L_{r1})}$ and $Z_{i3} = \sqrt{L_{r1}/C_c}$

This interval ends when the resonant current is decreased to zero.

Mode 5 (t_4-t_5): At time $t=t_4$, the magnetizing current continues decreasing and the resonant current passing through the clamp-switch is reversed. The resonant current can be expressed as

$$i_{Lr1}(t) = i_c(t) \approx \frac{V_{dc}\sqrt{L_{r1}C_c}}{nL_m} sin(\omega_{r4}(t - t_4)) \quad (3.49)$$

where $\omega_{r4} = \omega_{r3} = 1/\sqrt{C_c L_{r1})}$

This mode ends when the clamp-switch is turned off and the voltage across the clamp-switch starts to rise. Hence, the ZVS turn-off of the clamp switch is achieved.

Mode 6 (t_5-t_6): At the beginning of this interval, the clamp-switch S_c is turned off and the resonant circuit is formed by the resonant inductance L_{r1} and capacitance C_{r1}. The resonant capacitance C_{r1} across the main switch starts to discharge by the negative resonant current i_{Lr1} and the voltage across the main switch is decreasing. The resonant capacitor voltage V_{Cr1} and resonant inductor current i_{Lr1} are expressed as

$$V_{Cr1}(t) = V_{ds,Sm}(t) = V_{PV} + V_{dc}/n + (V_{Cr1}(t_5) - V_{PV} - V_{dc}/n)\, cos(\omega_{r5}(t - t_5)) + i_{Lr1}(t_5) Z_{i5} \sin(\omega_{r5}(t - t_5)) \quad (3.50)$$

$$i_{Lr1}(t) = i_{Lr1}(t_5) \cos\big(\omega_{r5}(t - t_5)\big) + \frac{(V_{Cr1}(t_5) - V_{PV} - V_{dc}/n)}{Z_{i5}} sin(\omega_{r5}(t - t_5)) \quad (3.51)$$

where $\omega_{r5} = 1/\sqrt{C_{r1}L_{r1})}$ and $Z_{i5} = \sqrt{L_{r1}/C_{r1}}$

Due to the small value of the resonant capacitor C_{r1}, the time interval of this stage is very small. Therefore, the voltage and current can be expressed as

$$V_{Cr1}(t) = V_{ds,Sm}(t) \approx V_{Cr1}(t_5) + \frac{i_{Lr1}(t_5)}{C_{r1}}(t - t_5)) \quad (3.52)$$

$$i_{Lr1}(t) \approx i_{Lr1}(t_5) - \frac{V_{Cr1}(t_5) - (V_{PV} + V_{dc}/n)}{L_{r1}}(t - t_5) \quad (3.53)$$

The voltage V_{Cr1} should reach zero at the end of this stage to ensure the ZVS turn-on of the main switch S_m at the next mode. Therefore, the energy stored in the resonant capacitor C_{r1} must be less than the energy stored in resonant inductor $L_{r1,}$ i.e. $\frac{1}{2}C_{r1}(V_{PV} + V_{dc}/n)^2 \leq \frac{1}{2}{i_{Lm\_pk}}^2 L_{r1}$. This interval ends when $V_{Cr1} = 0$. The output diode current is abruptly decreased in this stage.

Mode 7 (t_6-t_7): At $t=t_6$, the resonant capacitor voltage V_{Cr1} becomes zero and the resonant inductor current conducts through the antiparallel diode of the main switch S_m. The current is continuously decreasing and can be expressed as

$$i_{Lr1}(t) = -i_{Sm}(t) = i_{Lr1}(t_6) + \frac{V_{PV}+V_{dc}/n}{L_{r1}}\,(t - t_6) \tag{3.54}$$

The main switch S_m should be turned on before the resonant current i_{Lr1} changes its direction to ensure the ZVS of the switch. This mode ends when the main switch is turned on.

Mode 8 (t_7-t_8): At $t=t_7$, the drain-source voltage of the main-switch $V_{ds,Sm}$ is zero and the ZVS turn-on of the main switch S_m is achieved. The resonant inductor current i_{Lr1} passing through the main switch continue decreasing and become zero at the end of this stage.

3.3.2 Resonant H-Bridge inverter

The DC-AC stage consists of a resonant auxiliary branch with an H-Bridge inverter. The auxiliary branch is composed of a resonant switch S_r, resonant capacitor C_{r2}, auxiliary clamp-capacitor C_{ca}, and a resonant inductor L_{r2}. The capacitors C_1-C_4 are the parallel combination of additionally added very small capacitors with the parasitic capacitors of the switches. The resonant switch is turned off at the transitions of the switches of H-Bridge inverter. Hence, the voltage across the phase leg is resonated to zero and the switches achieve ZVS turn-on. The resonant switch also turned on at ZVS and therefore no switching losses occur due to the auxiliary circuit. During the turn-off period of the resonant switch, a short circuit pulse is provided to all of the main switches to charge the resonant inductor of the auxiliary branch. The key waveforms in a switching cycle of the inverter are presented in Figure 3.14.

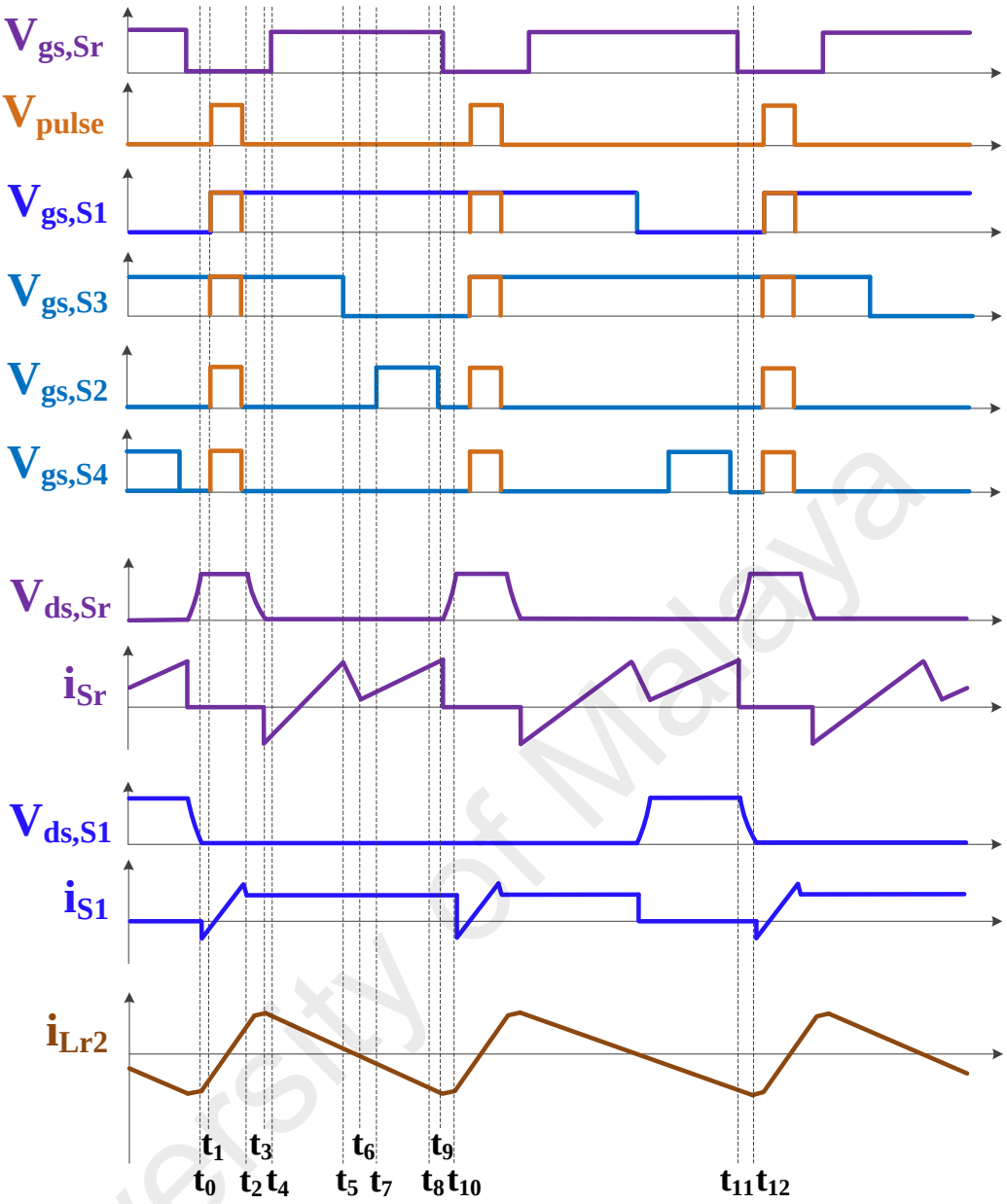

Figure 3.14: Key waveforms of the resonant inverter in a switching cycle

The key operation of the H-Bridge inverter can be divided as charging and resonant modes. The charging modes of the resonant inductor and the ZVS operation of the switches in resonant modes are described in the following.

Charging Modes (t_0-t_1 & t_1-t_2): The resonant inductor L_{r2} is charged by two stages. Firstly, the resonant current passes through the anti-parallel diode of the switches from the time $t=t_0$ to $t=t_1$, as shown in Figure 3.15(a). Secondly, a short-circuit pulse is applied to all of the switches from the time $t=t_1$ to $t=t_2$, as shown in Figure 3.15(b). The

voltage across the inductor is $V_{dc,Lr2}$. The rate of the increasing of the resonant current can be expressed as:

$$\frac{d}{dt}(i_{Lr2}) = \frac{V_{dc,Lr2}}{L_{r2}} \tag{3.55}$$

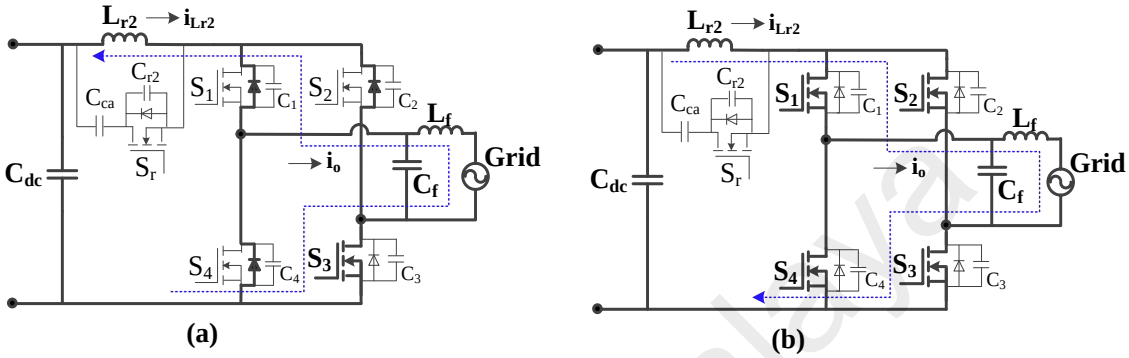

Figure 3.15: Charging modes of the resonant inductor (a) t_0-t_1 (b) t_1-t_2

Resonant Modes (t_2-t_3, t_9-t_{10} & t_{11}-t_{12}): There are three resonant modes in the circuit operation. The first one starts at $t=t_2$ after the short-circuit pulse operation in the switches. The switch S_1 and S_3 are remaining on while the S_2 and S_4 are turned off, as shown in Figure 3.16(a). The resonant capacitor C_{r2} is discharged through the resonant inductor and the switch capacitors C_2 and C_4 are being charged. Hence, the drain-source voltage of S_2 and S_4 cannot rise immediately due to the capacitor charging and the switches achieve ZVS turn-off. The resonant capacitor is fully discharged at $t=t_3$ and the resonant switch S_r has ZVS turn-on at $t=t_4$.

The second resonant mode starts at $t=t_9$, when the resonant switch is turned off and the switch S_1 is remaining on as shown in Figure 3.16(b). The resonant inductor L_{r2} charges the resonant capacitor C_{r2} and the drain-source voltage of S_r starts to rise gradually. Hence, the resonant switch is turned off at zero voltage condition. The switch S_2 has also ZVS turn-off due to the charging operation of C_2 in this mode.

The third resonant mode starts at $t=t_{11}$, when the resonant switch S_r is turned off and the switch S_3 is remaining on as shown in Figure 3.16(c). The resonant capacitor C_{r2} is charged by the resonant inductor L_{r2} and the switch capacitors C_1 and C_2 are being discharged. Therefore, the resonant switch achieves ZVS turn-off.

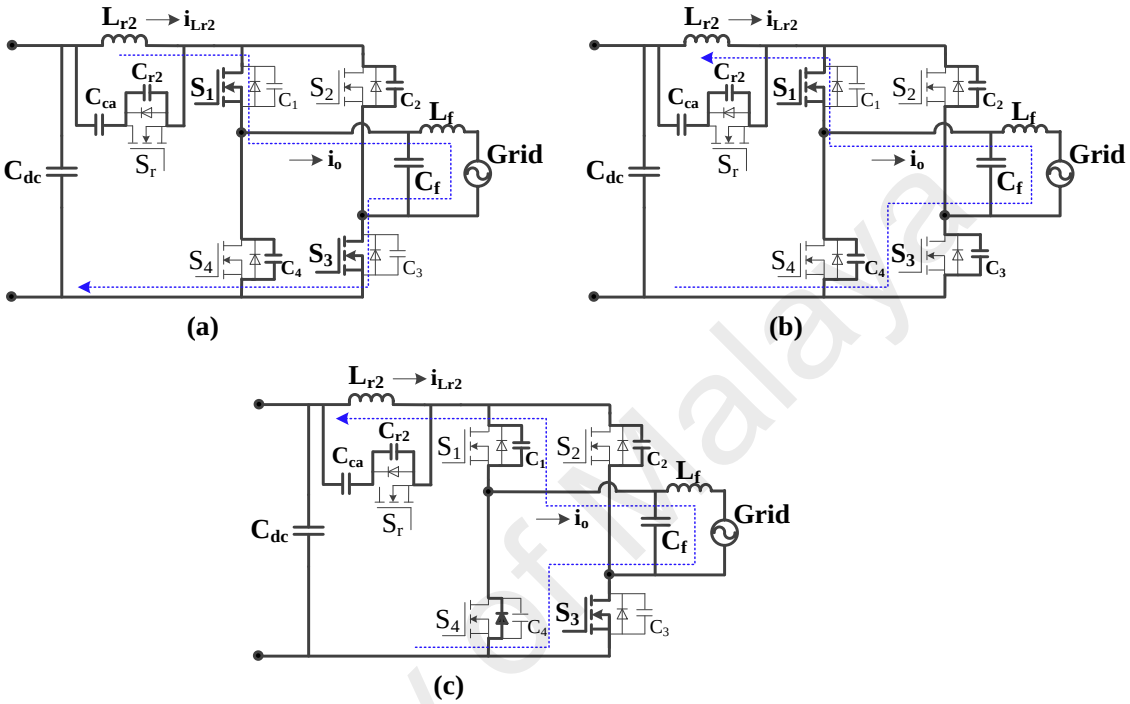

Figure 3.16: Resonant modes of the circuit operation (a) t_2-t_3 (b) t_9-t_{10} (c) t_{11}-t_{12}

3.3.3 Design consideration

This section provides the guidelines based on the analysis of the steady state operation to make the design procedure clearer. The design equations of the active-clamp resonant DC-DC flyback converter and the resonant full-bridge inverter are presented to achieve a highly efficient microinverter for PV application.

The power transfer capability of a flyback converter in a certain operating frequency depends on the value of the magnetizing inductance L_m. In the proposed DC-DC operation, the magnetizing current i_{Lm} becomes zero within each switching period T_s,

and the transformer is completely demagnetized. During the ON time of primary switch S_m, the energy E_{Lm} is stored in the magnetizing inductance and is expressed as

$$E_{Lm} = \frac{1}{2} L_m (i_{Lm\_pk})^2 = \frac{1}{2} L_m \left(\frac{V_{PV}}{L_m + L_{r1}} (DT_s) \right)^2 \tag{3.56}$$

For a lossless system, the averaged input power of the PV is equal to the averaged DC output power i.e. $P_{PV} = P_{dc}$.

$$V_{PV} I_{PV} = \frac{{V_{dc}}^2}{R} \tag{3.57}$$

The averaged input DC photovoltaic current can be obtained as

$$I_{PV} = \frac{1}{2} \left(\frac{V_{PV}}{L_m + L_{r1}} (DT_s) \right) (DT_s) \left(\frac{1}{T_s} \right) \tag{3.58}$$

Now equating the PV power with the output DC power

$$V_{PV} I_{PV} = \frac{1}{2} \left(\frac{{V_{PV}}^2}{L_m + L_{r1}} (D^2 T_s) - DV_{PV} \right) = \frac{{V_{dc}}^2}{R} \tag{3.59}$$

$$\frac{{V_{PV}}^2}{L_m + L_{r1}} = \frac{DV_{PV} + 2{V_{dc}}^2/R}{D^2 T_s} \tag{3.60}$$

$$L_m \geq \frac{{V_{PV}}^2 D^2 T_s}{DV_{PV} + 2{V_{dc}}^2/R} - L_{r1} \tag{3.61}$$

From the expression of the magnetizing inductance of the flyback converter, it is shown that the inductance value depends on the PV voltage, maximum duty cycle and switching frequency of the flyback converter. The switching frequency is obtained from the operating modes of the flyback converter and can be expressed as:

$$f_{sw} = \frac{1}{T_s} = \frac{1}{t_{01} + t_{12} + t_{23} + t_{34} + t_{45} + t_{56} + t_{67} + t_{78}} \tag{3.62}$$

From the equation (3.62), the switching frequency can be found and is optimized with the magnetizing inductance expressed in equation (3.61). The switching frequency of the proposed flyback DC-DC converter is chosen as 50 kHz.

The maximum duty cycle of the flyback converter operated in proposed mode can be obtained as

$$D_{max} = \frac{V_{dc}(1-D_w)}{V_{PV\_min}+V_{dc}} \tag{3.63}$$

where, D_w is the dwell time duty ratio of the DC-DC converter.

The selection of the magnetizing inductance with the different levels of PV voltage and duty ratio is shown in Figure 3.17. The magnetizing inductance is chosen as 6.6µH with duty cycle D=0.40 and PV input voltage of 45 V.

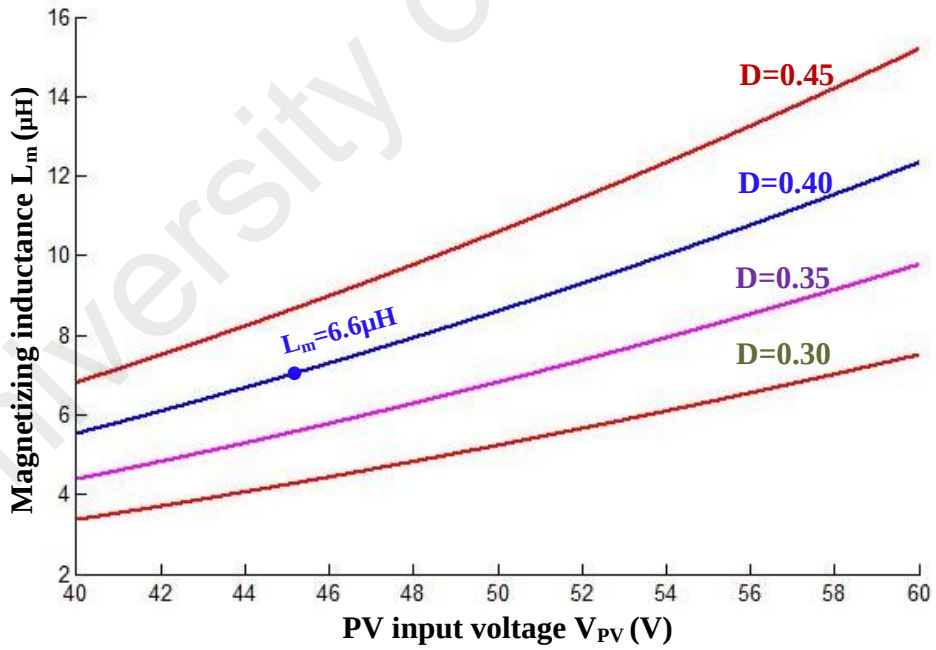

Figure 3.17: Selection of the magnetizing inductance, L_m

In *Mode 4 & 5* of the DC-DC converter, the energy of resonant inductor L_{r1} is absorbed in the clamp-capacitor C_c. The clamp capacitor C_c and resonant inductor L_{r1} are resonant about one-half of the resonant period. This resonant period is approximately

equal to the maximum turn off time of the main switch. Therefore, neglecting the switching transient period, the resonant period $T_{resonant}$ (L_r, C_{clamp}) can be expressed as follows:

$$T_{resonant}\,(L_{r1}, C_c) = \pi\sqrt{L_{r1}C_c} \approx (1-D)T_s \tag{3.64}$$

The average voltage of the capacitor can be found based on the charge balance of the clamp-capacitor and is expressed as

$$V_{Cc} = \frac{V_{PV}DT_S}{\pi\sqrt{L_{r1}C_c}} \tag{3.65}$$

The resonant current i_{Lr1} charge the clamp-capacitor C_c during the transient period in *Mode 3* and the energy is stored in the clamp-capacitor. This stored energy circulates through the clamp circuit, and is transferred to the output circuit, is expressed as

$$E_{clamp} = \frac{1}{2L_{r1}}\left(\frac{V_{PV}DT_S}{\pi}\right)^2 \tag{3.66}$$

To ensure the ZVS operation of the main switch, the energy stored in the parasitic capacitance must be dissipated through the resonant circuit formed by L_{r1} and C_{r1}. Hence, the resonant inductance L_{r1} can be obtained from the energy equation described in *Mode 6*, and is expressed as

$$L_{r1} > \frac{C_{r1}(V_{PV}+V_{dc}/n)^2}{{i_{Lm\_pk}}^2} \tag{3.67}$$

The selection of the resonant inductance with respect to PV voltage level and different turn ratio is shown in Figure 3.18. The resonant inductor is chosen as 2.1µH with a flyback converter turn's ratio n=3.

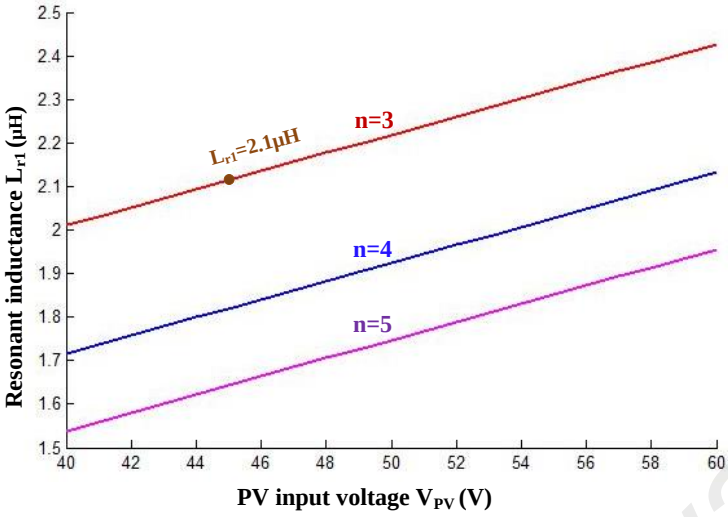

Figure 3.18: Selection of the resonant inductance, L_{r1}

In order to discharge the resonant capacitor properly, the required dead time T_d between the transitions must be equal or greater to the quarter of the resonant period generated by L_{r1} and C_{r1} and is found as

$$T_d \geq \frac{\pi\sqrt{L_{r1}C_{r1}}}{2} \tag{3.68}$$

Therefore, the selection of the resonant capacitor C_{r1} depends on the value of resonant inductor L_{r1} and dead time allowed, as shown in Figure 3.19.

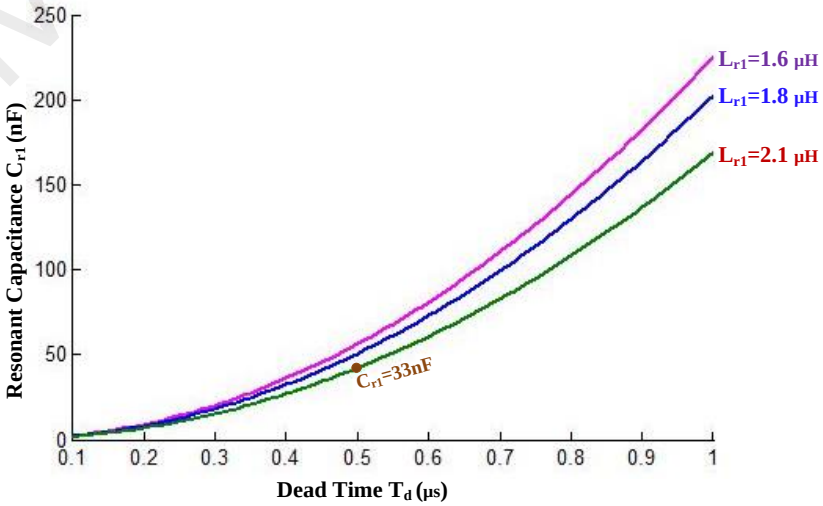

Figure 3.19: Selection of the resonant capacitance, C_{r1}

The resonant inductor L_{r2} used in the auxiliary branch of DC-AC inverter can be obtained from the charging modes and is expressed as

$$L_{r2} \geq \frac{V_{dc}}{\frac{d}{dt}(i_{Lr2})} \tag{3.69}$$

The auxiliary clamp-capacitor C_{ca} is found allowing a voltage ripple Δv_{Cc} from the time $t=t_3$ to $t=t_9$.

$$C_{ca} = \frac{1}{\Delta v_{Cc}}\left(\int_{t_3}^{t_6}(|i_0| - i_{Lr})\,dt + \int_{t_6}^{t_9}(-i_{Lr})\,dt\right) \tag{3.70}$$

3.3.4 Proposed Control for double-stage microinverter

The control technique of a double-stage microinverter is quite different from a single-stage one. Two PWM blocks are dedicated to control the DC-DC flyback converter and DC-AC full bridge inverter, as shown in Figure 3.20. The flyback PWM generates the switching signal for main-and clamp switch of the flyback converter considering the MPPT operation of PV and DC-link voltage. The inverter SPWM generates the switching signal for the resonant H-bridge inverter. The double-frequency sinusoidal PWM generates the gate signal for the bridge switches and resonant-switch comparing the grid current with the reference current.

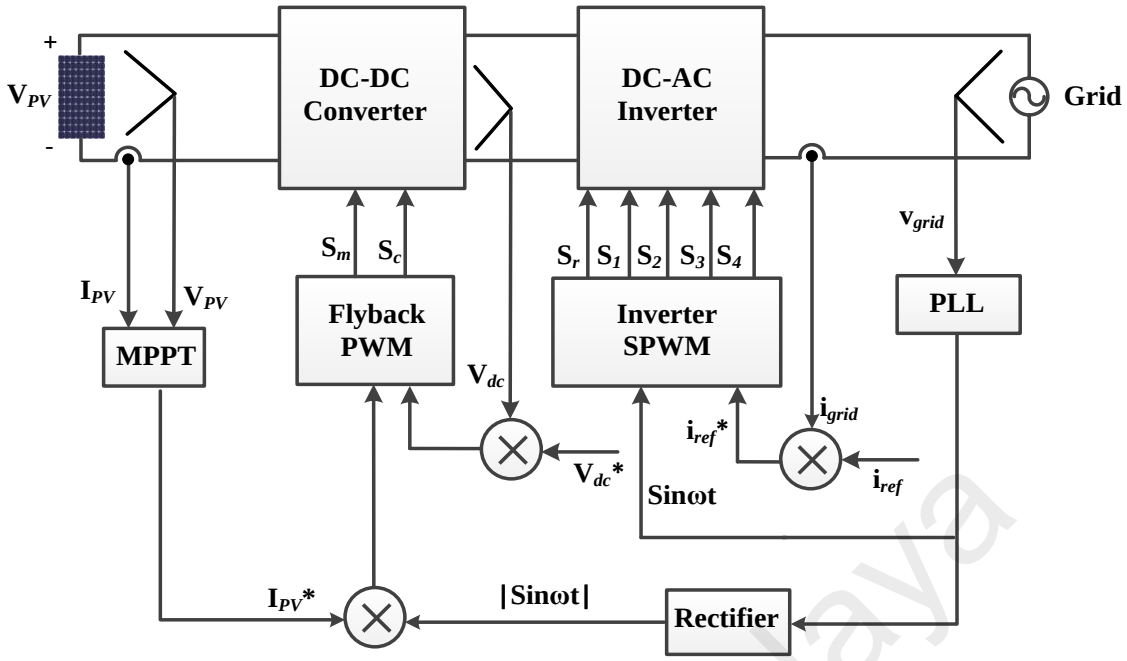

Figure 3.20: Control block diagram of the proposed single-stage microinverter

3.4 Summary

This chapter has presented the detail analysis of the system configuration of single-stage and double-stage microinverter. The resonant operations in different modes and the soft switching methods of the proposed topology have been explained. The design consideration for the single-stage flyback converter with unfolding circuit and DC-DC flyback with H-Bridge inverter was explained. The selection of the magnetizing inductance of the flyback converter, resonant components and power semiconductor devices are analyzed mathematically with a view to determine the appropriate value of these parameters. The loss analysis of the circuit components has been presented in this section because efficiency is an important aspect in realizing a grid-tied PV microinverter. Moreover, this chapter also contributes in modelling the control operation for the single-stage and double-stage microinverter.

CHAPTER 4: SIMULATION AND EXPERIMENTAL RESULTS

4.1 Introduction

The chapter presents the simulation results of the proposed microinverter topology that is developed based on the methodology described in the earlier chapter. The simulation study is carried out in MATLAB Simulink for a 250W single-stage flyback microinverter to explore and verify the proposed topology and control schemes. This is followed by the experimental results of single-stage and double-stage microinverter. The efficiency of the microinverter with different loading condition is measured in this chapter. Finally, the breakdown of losses of the components of proposed single-stage and double-stage microinverter is also presented.

4.2 Simulation Results

The MATLAB Simulink software is used to simulate the conventional flyback converter and proposed single-stage flyback microinverter. The key circuit parameters of the proposed topology are listed in Table 4.1.

Table 4.1: Key parameters of the proposed single-stage topology

Parameters	Symbol	Value
Rated Power	P_o	250W
PV voltage	V_{PV}	35-45V DC
Grid Voltage	V_{grid}	110V AC
Switching frequency	f_{sw}	80kHz
DC Link Capacitor	C_{dc}	5mF
Resonant inductance	L_r	2 µH
Resonant capacitance	C_r	10 nF
Flyback Transformer		
Turn's ratio	n (N_p:N_s)	1:3
No. of turns in primary	N_p	10
Magnetizing inductance	L_m	14µH
Leakage inductance	L_k	0.4µH
Air gap length	l_g	1.1mm

In Figure 4.1, the hard switching condition of the primary switch of a conventional flyback microinverter is presented. As the conventional hard-switched microinverter cannot be operated at higher switching frequency due to high switching losses, the switching frequency is taken as 50 kHz. It is observed that a large voltage spike is appeared when the switch is being turned off. Hence, large switching losses occur during the turn-off of the primary switch.

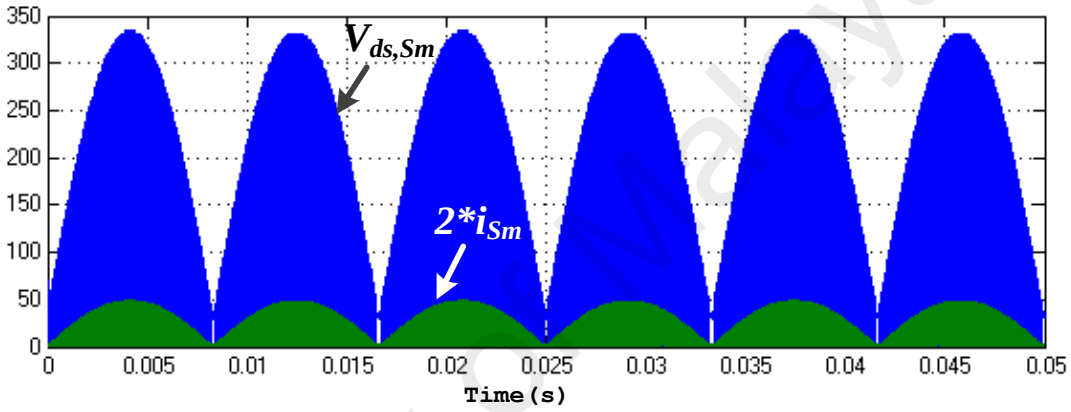

(a)

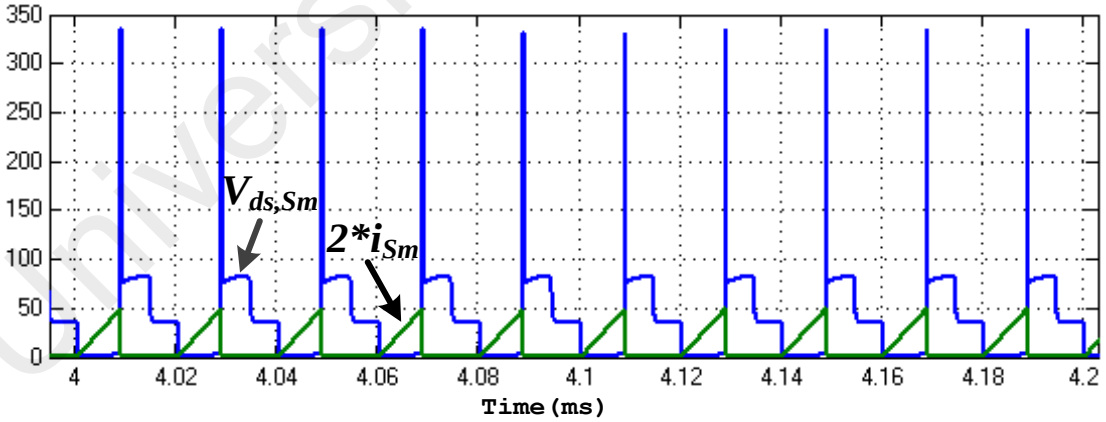

(b)

Figure 4.1: Voltage and current waveforms of the main switch of a conventional flyback microinverter over (a) line cycle, and (b) switching cycle

In Figure 4.2, the current and the drain-source voltage of the main switch of the proposed active-clamp resonant microinverter are presented with a switching frequency of 80 kHz. It is clearly shown that the voltage spike that has been arisen in the hard switching is being completely removed in the proposed microinverter.

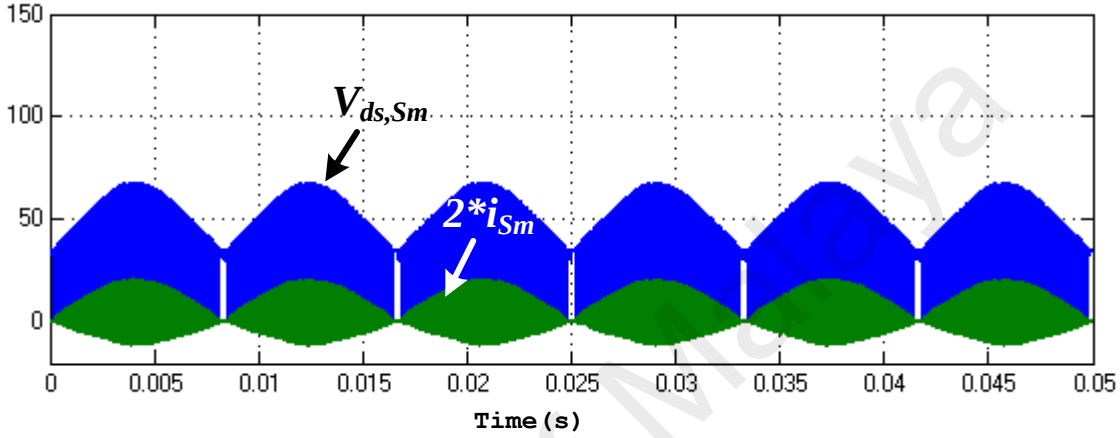

(a)

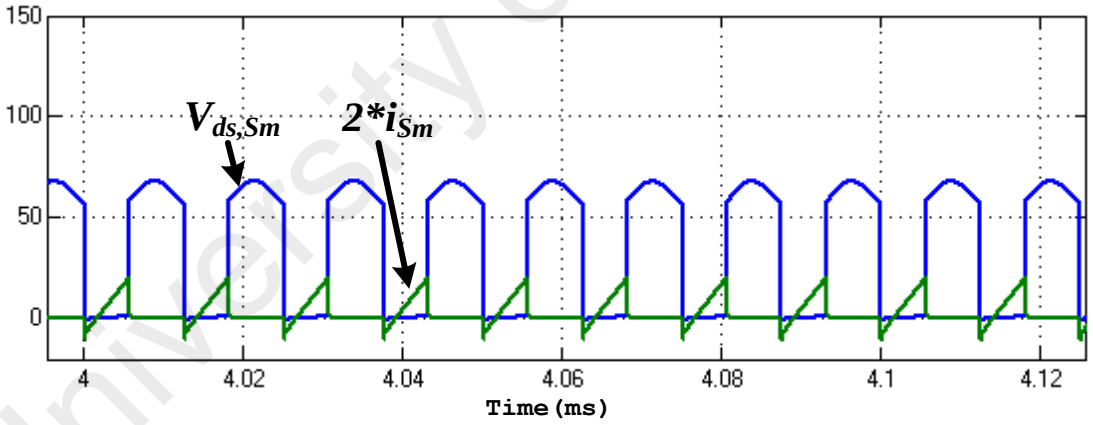

(b)

Figure 4.2: Voltage and current waveforms of the main switch of the proposed resonant flyback microinverter over (a) line cycle, and (b) switching cycle

In Figure 4.3, the magnetizing current of the flyback transformer and the current through the high frequency switches are presented for the different value of resonant inductor L_r. It is shown that the main switch cannot achieve proper soft switching when there is no resonant inductor. The ZVZCS of the main switch is achieved and the current stress of the switches is reduced by inserting a resonant inductor with the proposed hybrid operation. The soft-switching operation of the switches is illustrated in Figure 4.4 and Figure 4.5. The ZVS of main and clamp switch for the DCM region is shown in Figure 4.4. It has been observed that the ZVZCS operation of the main switch is fully achieved with the resonant inductor L_r =2 µH whereas the partial soft switching is attained without resonant inductor. In Figure 4.5, it is clearly shown that main switch attains ZVZCS with the proposed BCMVNC operation whereas the soft switching cannot be achieved without resonant inductor in the conventional BCM operation.

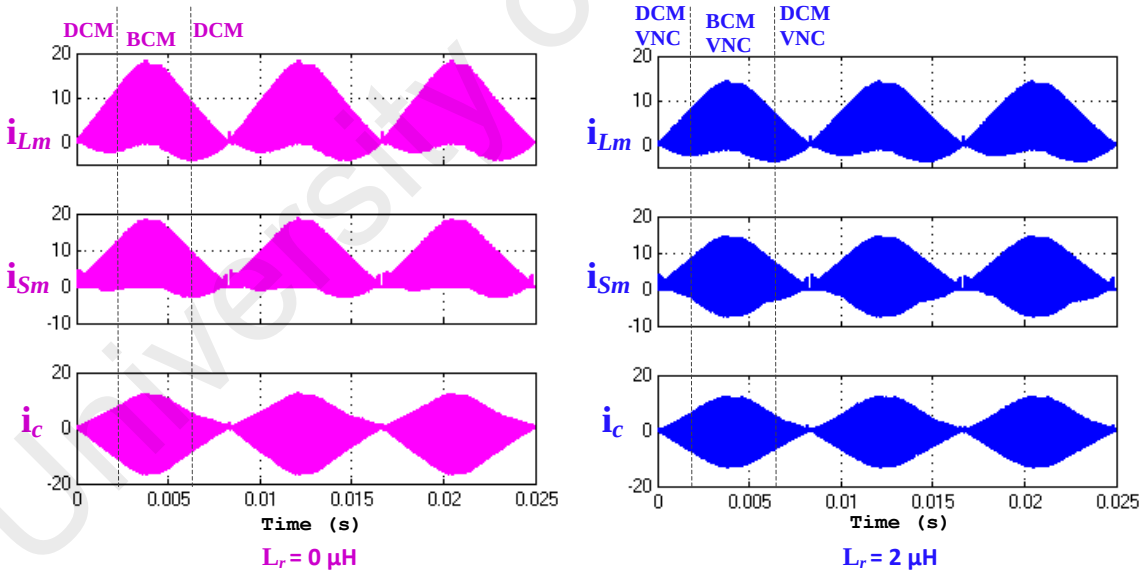

Figure 4.3: Current stress of the switches in line cycle with different value of L_r

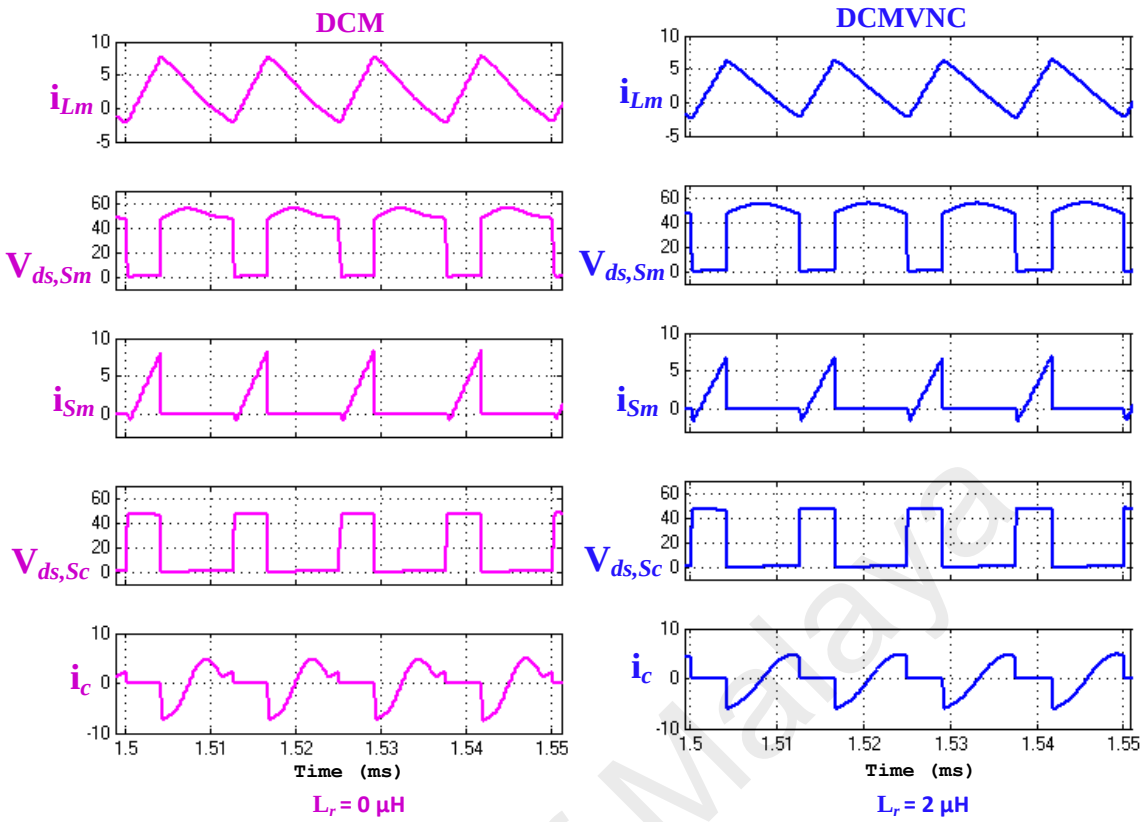

Figure 4.4: ZVS operation of main and clamp switch in DCM region

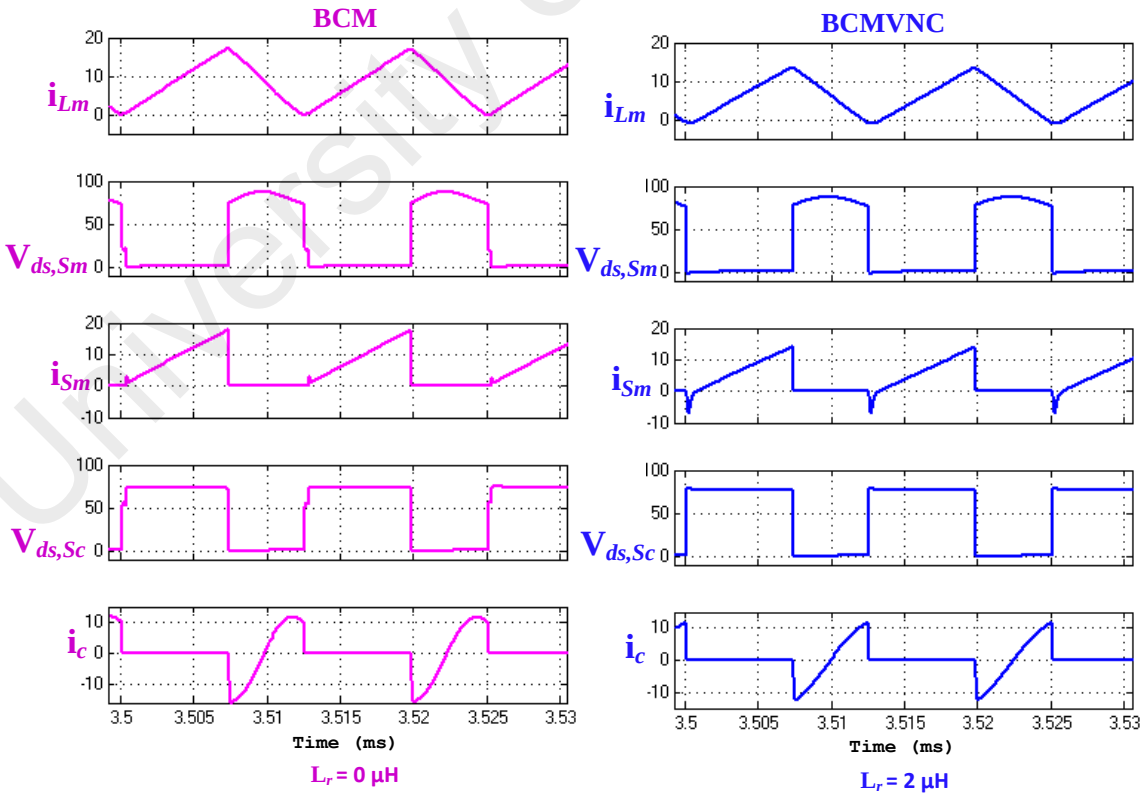

Figure 4.5: ZVS operation of main and clamp switch in BCM region

The output voltage and current of the microinverter are shown in Figure 4.6. It can be observed that the output voltage and current are in phase. The THD of the output voltage is only 2%, shown in Figure 4.7, which is below the maximum limit provided by the grid authorities.

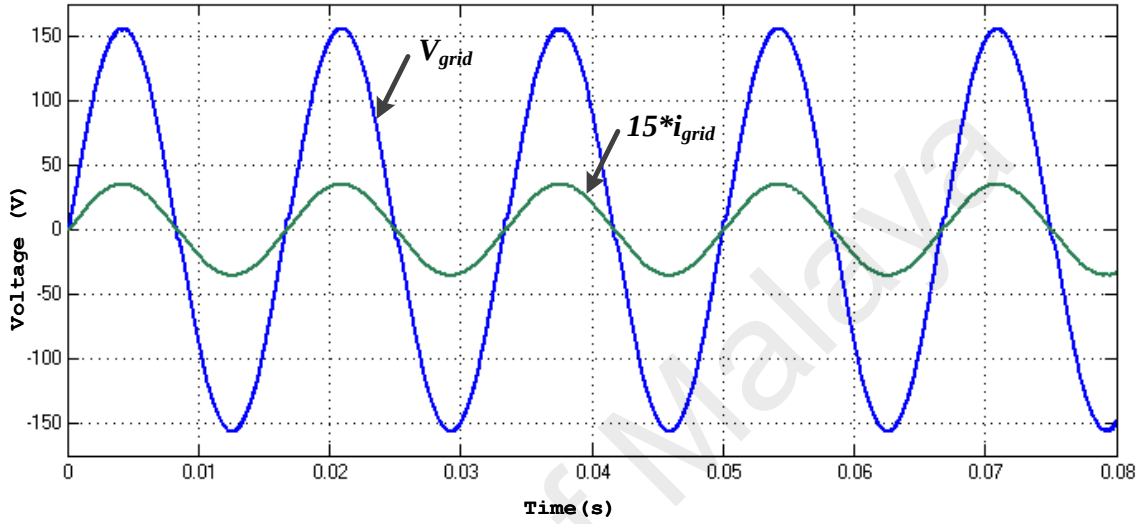

Figure 4.6: Output voltage and current of the microinverter

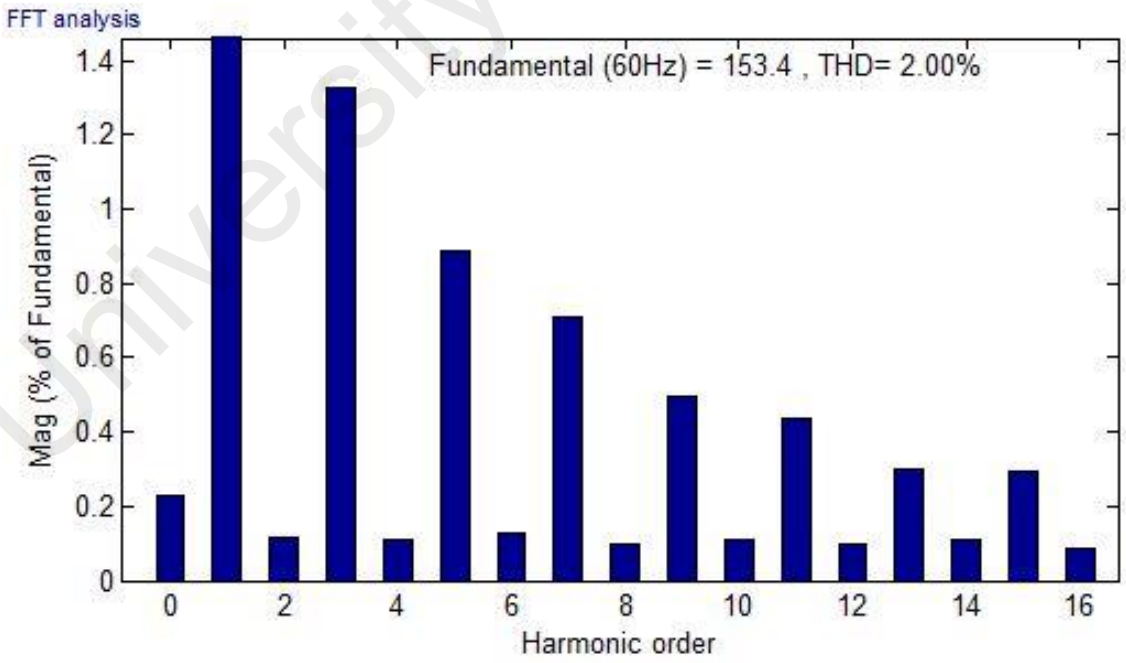

Figure 4.7: THD of output voltage of the microinverter

4.3 Experimental Results

A 250 W laboratory prototype is implemented to verify the validity of the proposed topology of the resonant microinverter, as shown in Figure 4.8. A single-stage and a double-stage microinverter have been built and the results have been recorded. The experimental results are explained in the following.

Figure 4.8: Experimental setup of the microinverter

4.3.1 Single-stage microinverter:

The key parameters of the prototype of a single-stage microinverter have been listed earlier in Table 4.1. The power semiconductor devices are listed in Table 4.2. A low voltage Si power MOSFET with low drain-source resistance is chosen in the high frequency primary side. The ultrafast diodes are selected to reduce the diode switching losses. The dSPACE DS1104 R&D Controller Board was used to drive the switches of the microinverter.

Table 4.2: Power semiconductor devices

Particulars	Symbol	Manufacturers	Package	Product ID
Si Power MOSFET	S_m & S_c	INFINEON	PG-TO220-3	IPP200N15N3G
Si Power MOSFET	S_{s1} & S_{s2}	INFINEON	TO247-3-1	IPW60R045CP
Ultra-fast Diode	D_1 & D_2	VISHAY	TO-247AC	VS-HFA15PB60PbF,-N3

The experimental waveforms present the soft switching of the main switch and clamp switch of the resonant converter. The voltage and current stress of the main switch and the clamp switch through the line cycle is shown in Figure 4.9. The stress on the switches varies with the change of amplitude of the grid current and it is maximum at the peak value of the grid current. In Figure 4.10, the drain-source voltage and current flow of the main switch S_m in DCMVNC and BCMVNC region is presented. It can be observed that the negative current flows due to the clamp circuit and the switch is turned on at zero voltage and zero current condition. The spike of the drain to source voltage during the ON period in a conventional active-clamp is being completely removed in the proposed resonant microinverter. Similarly, the ZVS turn-on of the secondary switch is shown in Figure 4.11. The switch is also turned off at low current value and hence lowering the turn-off loss. The turn-off of the secondary diodes can be observed from Figure 4.12.

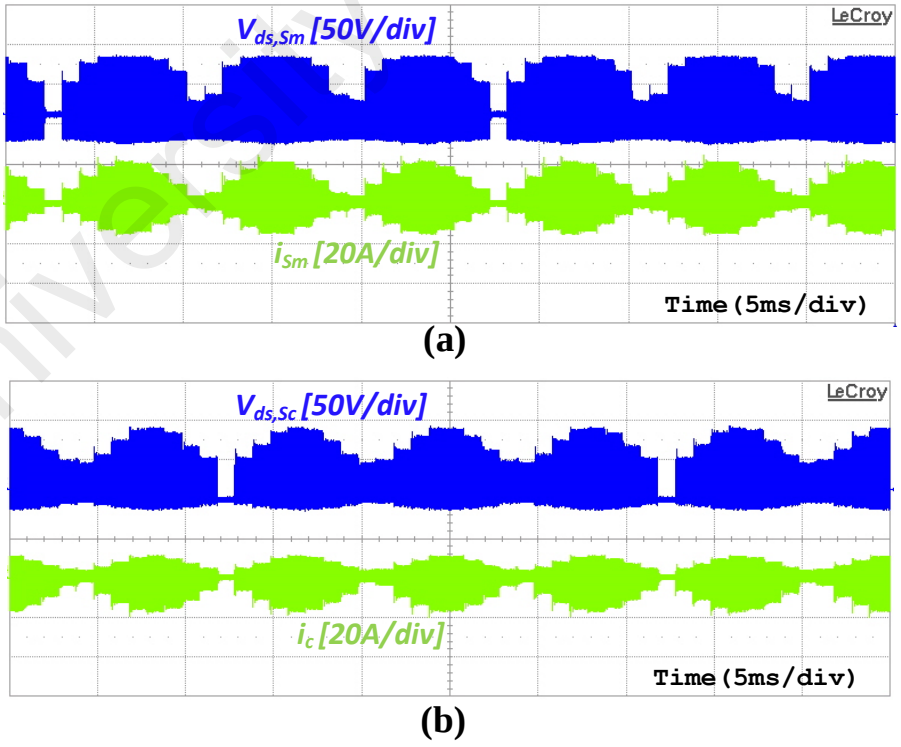

Figure 4.9: Voltage and current stress of the (a) main switch, and (b) clamp switch

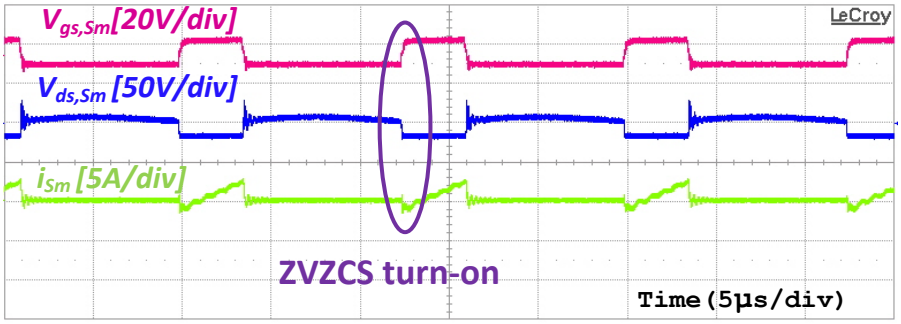

(a)

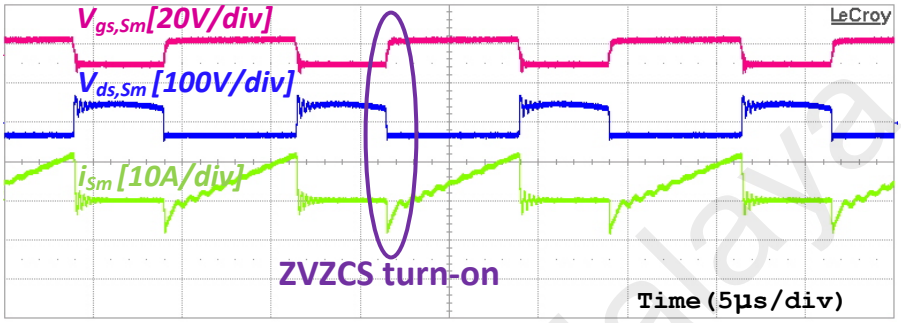

(b)

Figure 4.10: ZVZCS turn-on of the primary switch (a) DCMVNC region (b) BCMVNC region

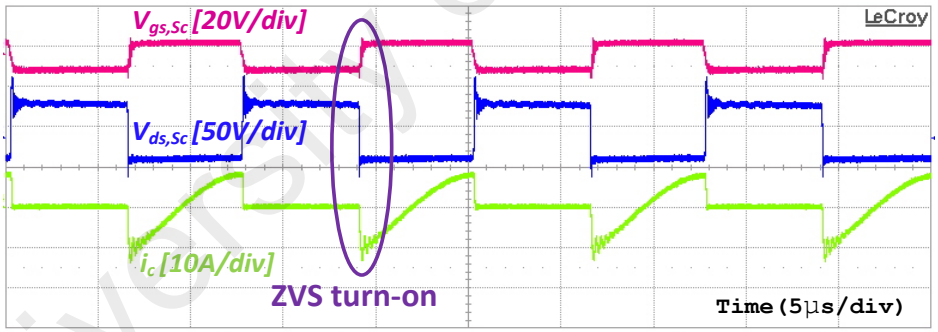

Figure 4.11: ZVS turn-on of the clamp switch

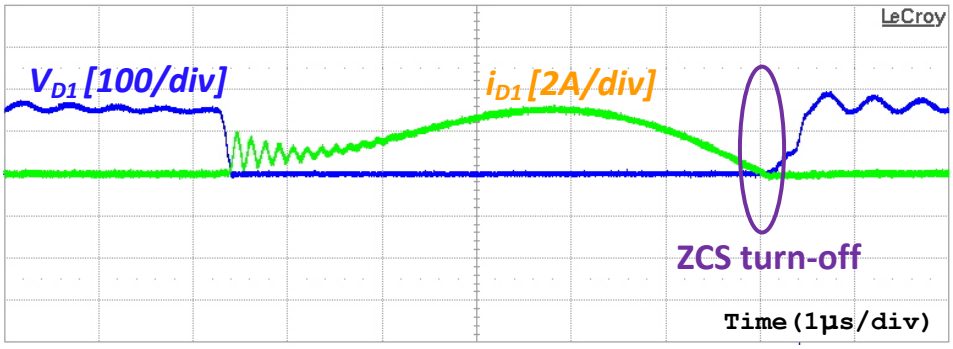

Figure 4.12: ZCS operation in output diodes

The output voltage and current of the proposed resonant microinverter is presented in Figure 4.13. The THD of the output current is measured by the power analyzer (Yokogawa WT1800) and found to be only 3.69%, as shown in Figure 4.14, which is within the limit set by the international grid authorities. The experimental results confirm the validity of the proposed topology and its capability in achieving zero voltage switching and reducing voltage and current stresses maintaining a good power quality.

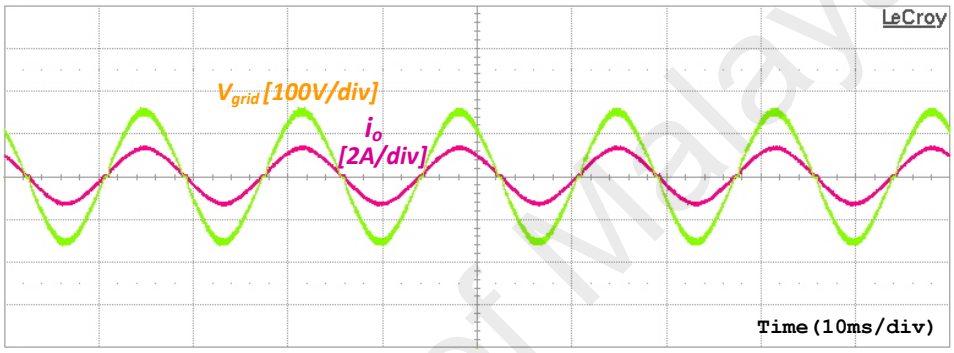

Figure 4.13: Output voltage and current of the proposed resonant microinverter

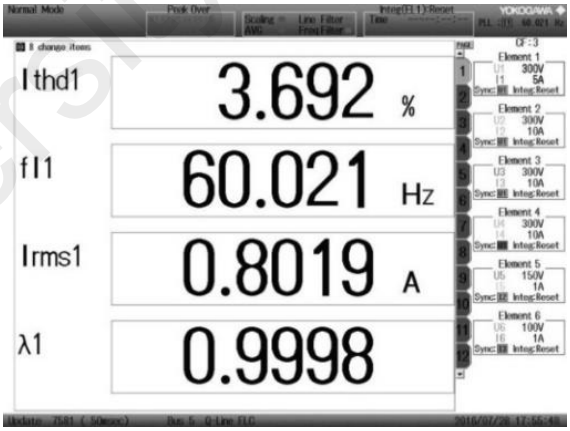

Figure 4.14: THD of the proposed resonant microinverter

The dynamic response of the proposed hybrid mode operation of the resonant microinverter is demonstrated in Figure 4.15, where the input PV voltage is abruptly changed from 35V to 12V. It can be observed that the circuit has a wide input voltage range with a fast transient response and the output current changes accordingly to

balance with the input power. In Figure 4.16, the sudden changing of output load is being shown, the output current is increased from 0.7 A to 1.4 A, whereas the input PV voltage is constant. The input PV current also increased to meet up the additional power of the load and there is no overshoot on input DC ripple current or output ac current.

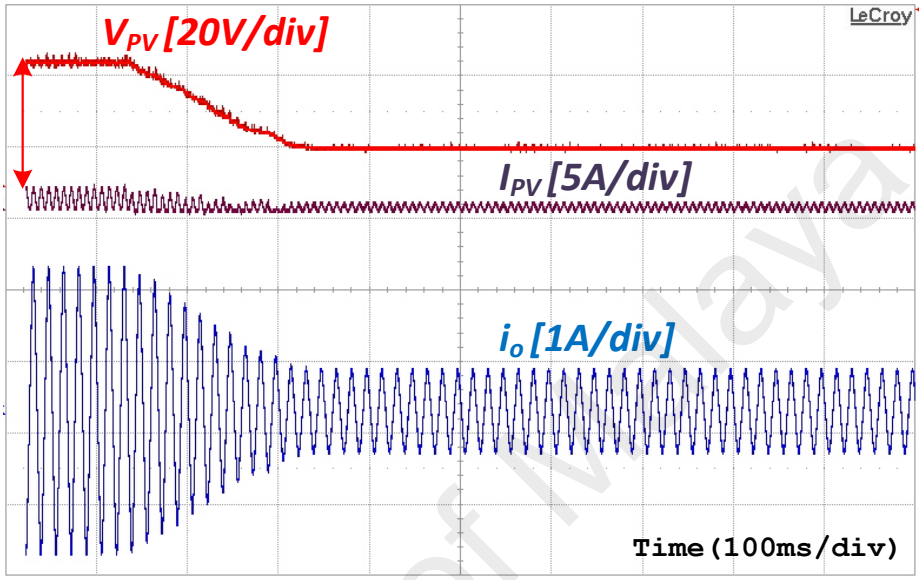

Figure 4.15: Dynamic responses during input voltage stepping

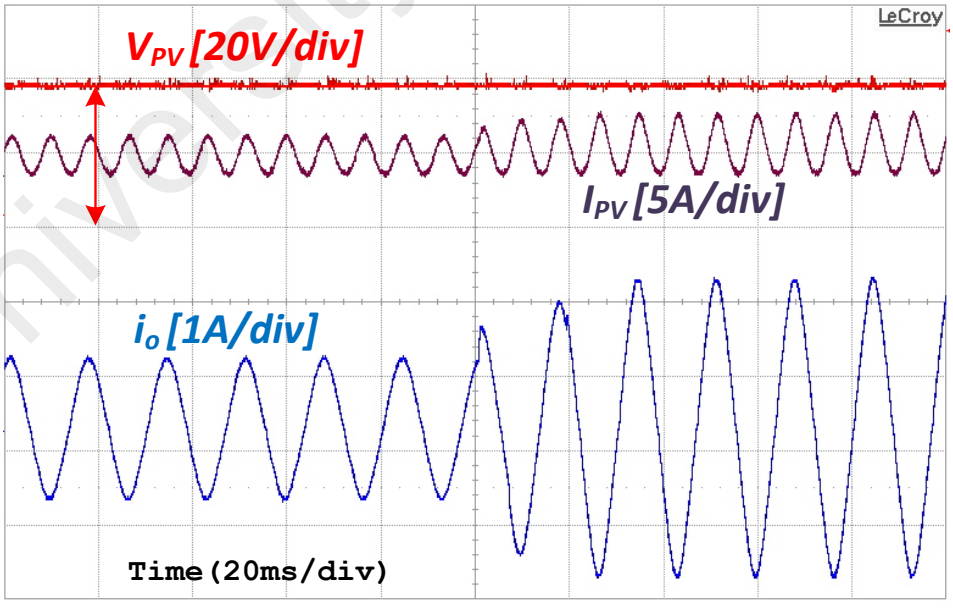

Figure 4.16: Dynamic responses during output load stepping

The efficiency of the 250 W microinverter with proposed hybrid operation for the different loads is presented in Figure 4.17. It can be observed that the peak efficiency reaches up to 97.1% at 70% of load and high efficiency is achieved through 30% to 100% of PV power condition. The California Energy Commission (CEC) efficiency is found to be 96.7%. The efficiency of the microinverter is also measured for the conventional DCM-BCM hybrid operation without resonant inductor and compared with the proposed one as shown in Figure 4.17. The proposed DCMVNC-BCMVNC hybrid operation with resonant inductor shows the superiority over the existing DCM-BCM operation in terms of efficiency in all loading condition. Especially in light load operation, the efficiency of the proposed microinverter is more improved due to the proper soft-switching operation in the extended DCMVNC region.

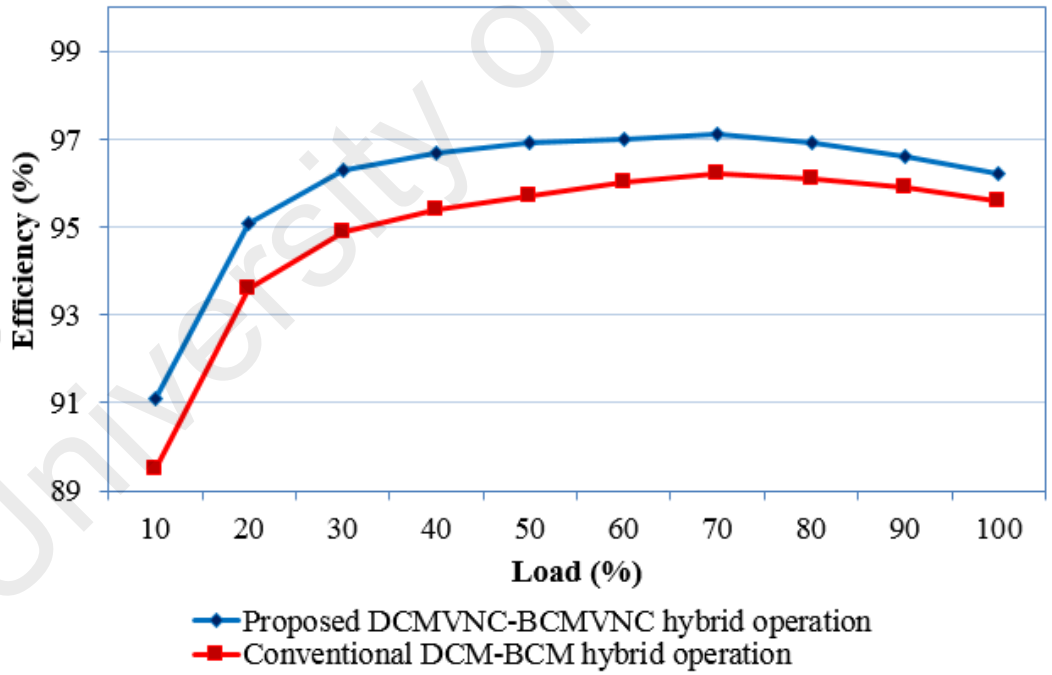

Figure 4.17: Efficiency curve

The breakdown of the losses of the transformer and power semiconductor devices at peak efficiency at 175 W of the proposed microinverter is shown in Figure 4.18. The total loss at is approximately 5.14 W at peak efficiency of 97.1%. Among the losses, it

is shown that the switching losses are quite small relating to others due to the soft-switching operation of the high frequency switches. The conduction losses of the switches are also limited due to the low current operation in the primary side due to the resonant inductor. The core losses in the transformer are the major contributors in decreasing the efficiency. An optimal design of the transformer can help to reduce the overall losses and hence improve the efficiency.

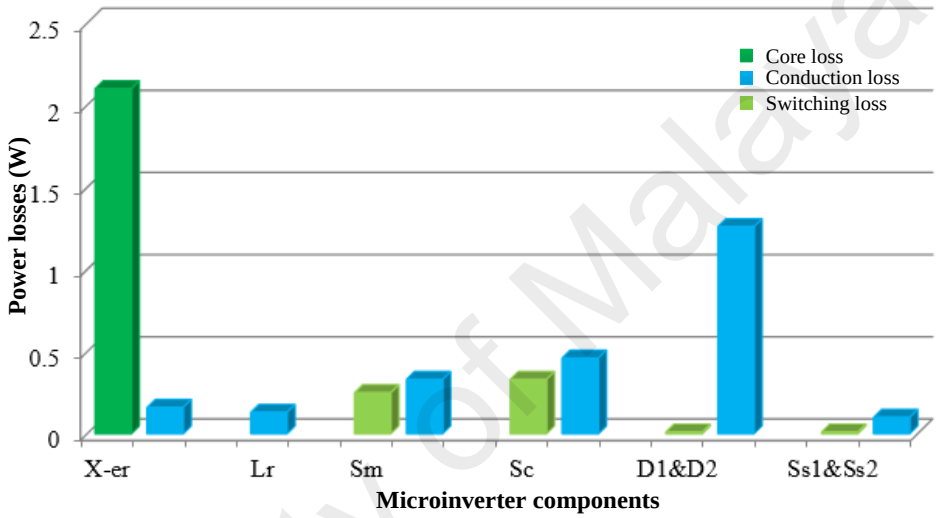

Figure 4.18: Breakdown of the losses

4.3.2 Double-stage Microinverter

A hardware prototype of a 250 W double-stage flyback microinverter has been built and the experimental results are taken to verify the aforementioned theoretical analysis. The modelling of the proposed converter is performed for a PV input of 40V-60V and grid output of 110V. The switching frequency of the DC-DC flyback converter is 50 kHz. The component values obtained from the design procedure are listed in Table 4.3. The duty cycle D is taken as 0.4 with a dead time of 0.5 µs.

Table 4.3: Key parameters of the proposed double-stage microinverter

Parameters	Label	Value
DC-DC Flyback Converter		
Magnetizing inductance	L_m	6.6µH
Resonant inductance	L_{r1}	2.1µH
Resonant capacitance	C_{r1}	33nF
Clamp capacitor	C_c	1.8µF
DC-DC output capacitor	C_o	15µF
Switching frequency	f_{sw}	50kHz
Resonant Inverter		
Inverter resonant inductor	L_{r2}	2.2uF
Inverter resonant capacitor	C_{r2}	1.2nF
Switch capacitors	C_1-C_4	1.2nF
Inverter filter inductor	L_f	2.5µH
Inverter filter capacitor	C_f	2.2µF

Figure 4.19 to Figure 4.24 represent the experimental waveforms of the proposed converter. Figure 4.19 illustrates the voltage and current waveform of the main switch S_m of the DC-DC converter with respect to the gate-driving signal. It is observed that the main-switch current i_{Sm} starts to increase when the drain to source voltage is zero. Hence, ZVS is achieved for the main switch of the flyback converter. As shown in Figure 4.19, both the ZVS turn-on and turn-off is achieved for the resonant capacitor C_{r1}=33nF whereas only the ZVS turn-on is achieved for C_{r1}=2.2nF. The ZVS operation of the clamp-switch is shown in Figure 4.20. It is observed that the clamp switch also achieve ZVS turn-on and turn-off, hence no switching losses for the clamp circuit.

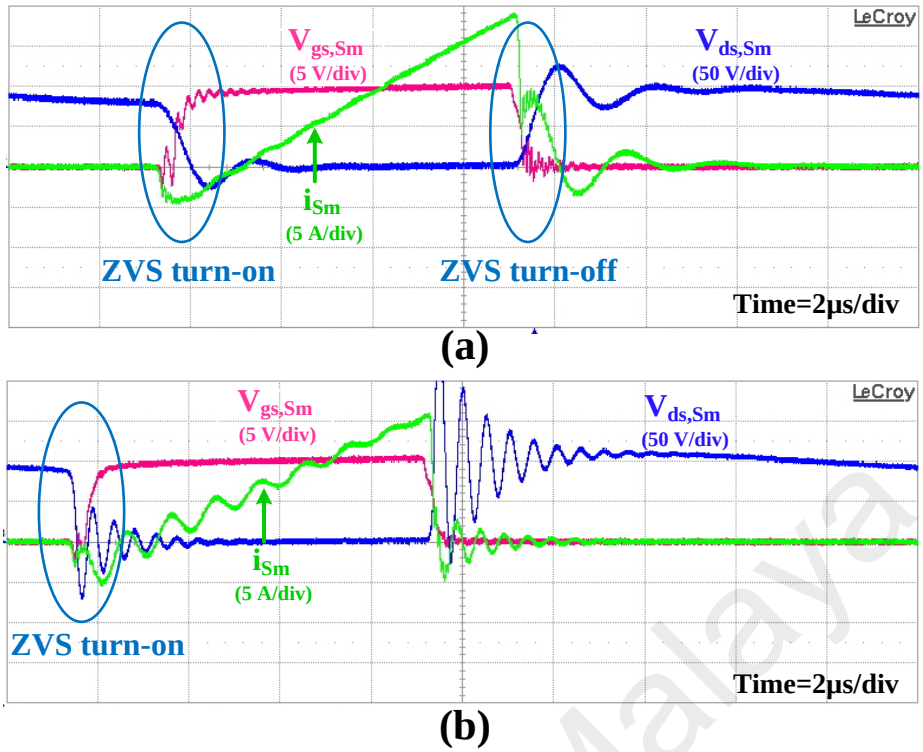

Figure 4.19: ZVS operation of the main switch with resonant capacitor (a) C_{r1}= 33nF (b) C_{r1}= 2.2nF

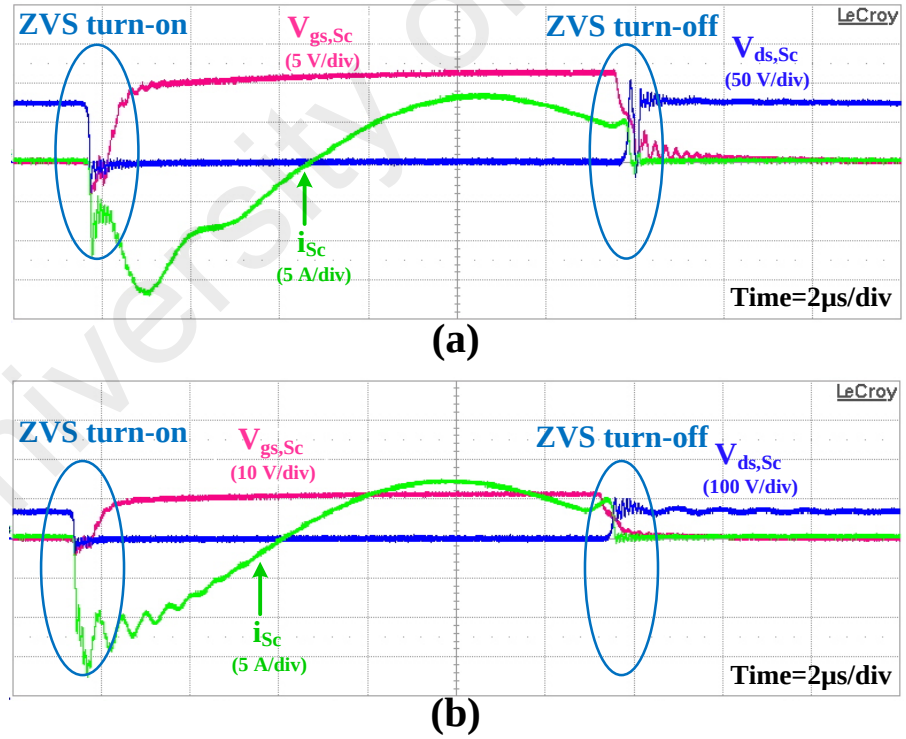

Figure 4.20: ZVS operation of the clamp-switch with resonant capacitor (a) C_{r1}= 33nF (b) C_{r1}= 2.2nF

Figure 4.21 shows the resonant current i_{Lr1} of the DC-DC flyback converter. In Figure 4.22, the ZCS turn-off of the rectifier diode of the flyback converter is presented. The soft switching of the flyback converter is still obtainable for the light load operation of the converter as shown in Figure 4.23. The output voltage and current of the proposed microinverter is shown in Figure 4.24. The total harmonic distortion of the output current is measured as 3.71% at the grid frequency of 60 Hz.

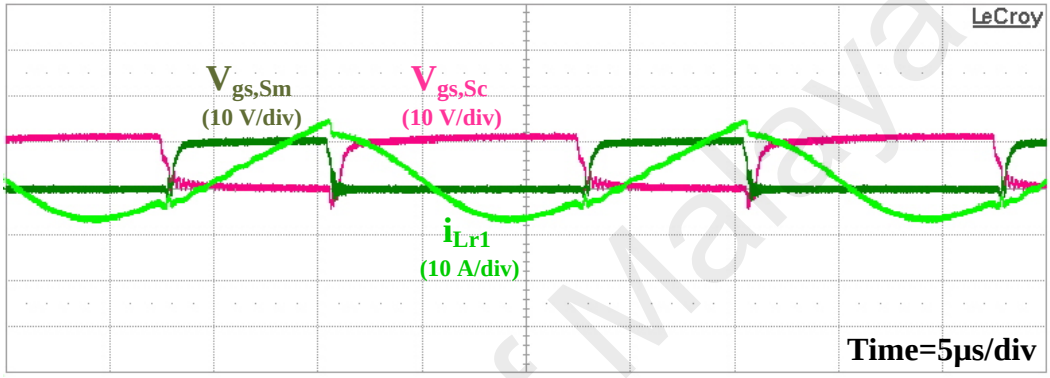

Figure 4.21: Resonant current of the DC-DC flyback converter

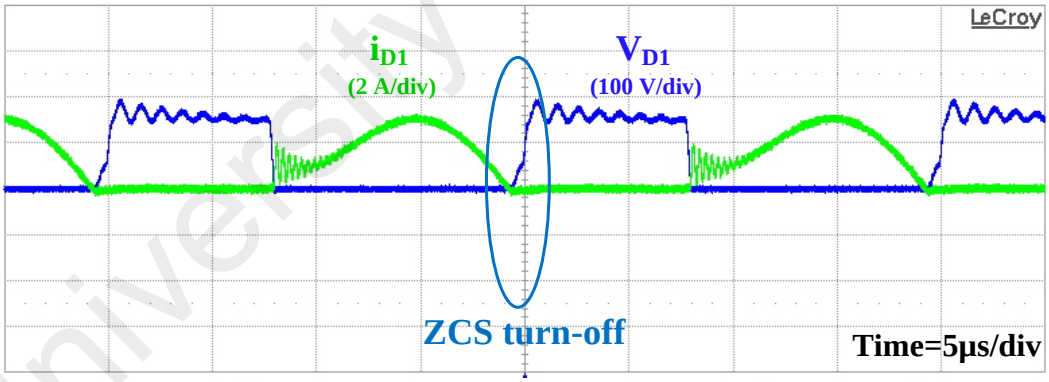

Figure 4.22: ZCS turn-off of the rectifier diode of the DC-DC converter

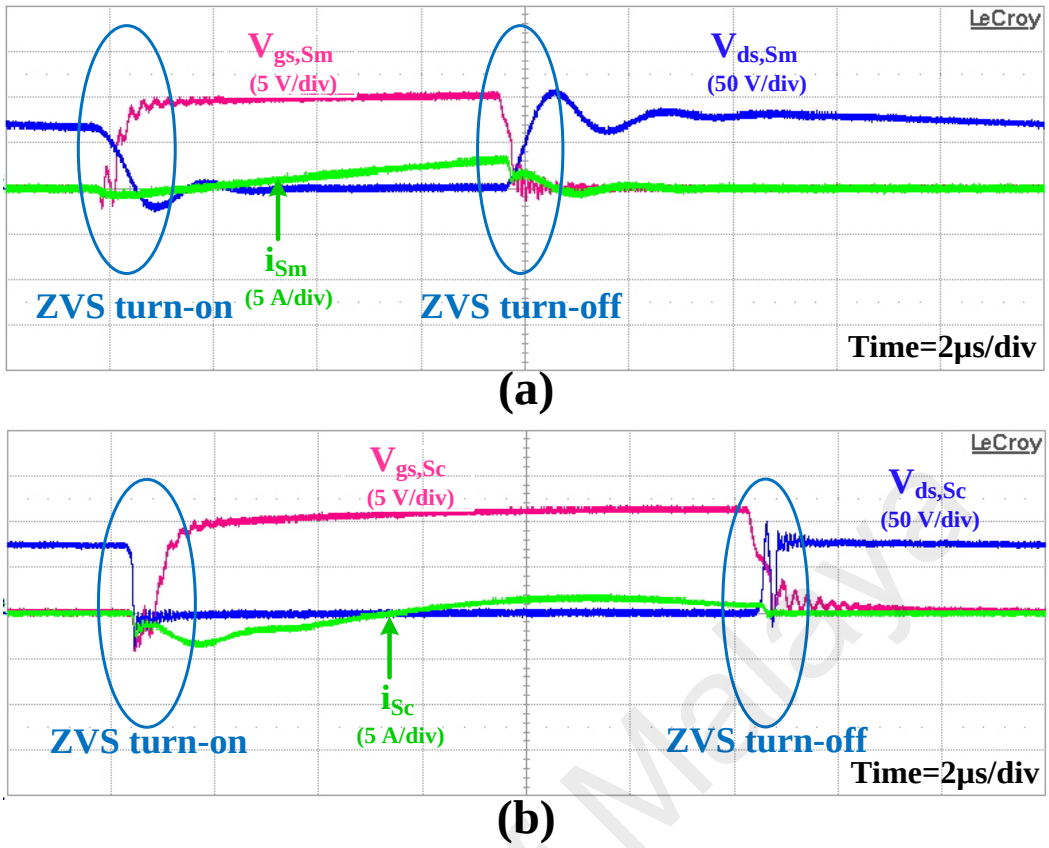

Figure 4.23: The soft-switching operation of the DC-DC converter for light load operation (a) ZVS of main-switch (b) ZVS of clamp-switch

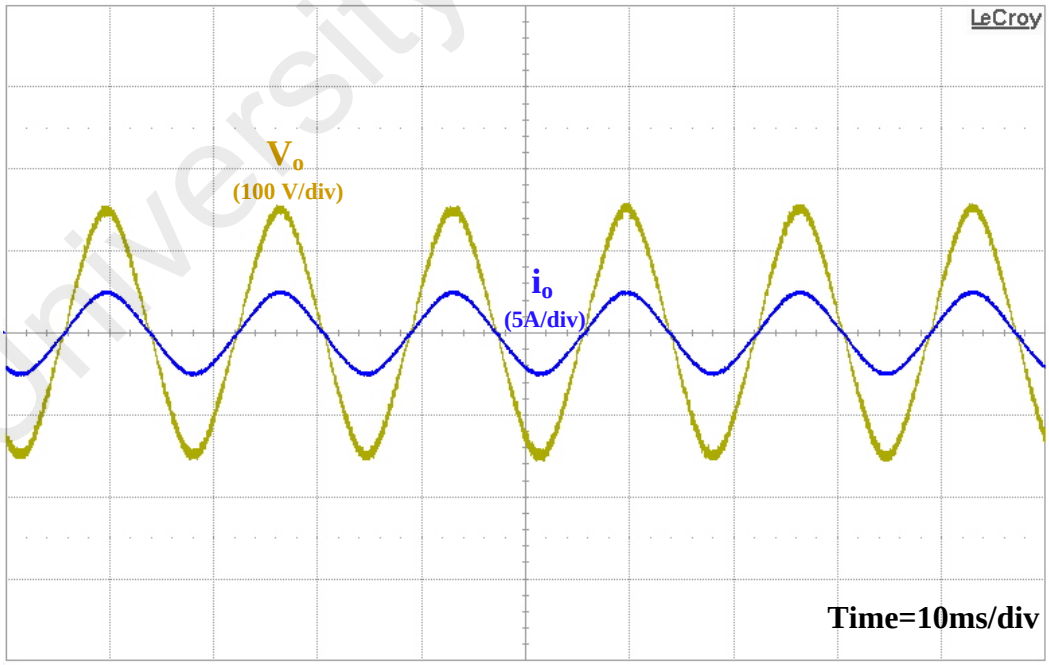

Figure 4.24: Output voltage and current of the proposed microinverter

In Figure 4.25, the efficiency of the DC-DC stage of proposed active-clamp flyback converter is presented for the different power output of the microinverter. The power efficiency of the proposed converter is then compared with a forward DC-DC converter and it is shown that the proposed one is more improved at light load condition, as shown in Figure 4.25. To verify the overall efficiency improvement, a microinverter using conventional full-bridge inverter is built with the same DC-DC converter. The efficiency comparison between the proposed microinverter with the resonant switch in inverter stage and the microinverter using conventional full-bridge is presented in Figure 4.26. The power efficiency of the proposed microinverter shows a distinct improvement over microinverter using the conventional full bridge in inverter stage. The maximum efficiency of the proposed microinverter is achieved 96.5% at 175W, and the California Energy Commission (CEC) efficiency is 95.9%. Figure 4.27 shows that the efficiency of the proposed microinverter is also high at full load operation for a wide range of input voltage of the PV modules. In Figure 4.28, the loss-breakdown of main components of the proposed microinverter is presented for the maximum efficiency at 175W. It is clearly observed from the loss analysis that the switching losses are relatively minor due to the soft-switching operation of the power semiconductor devices.

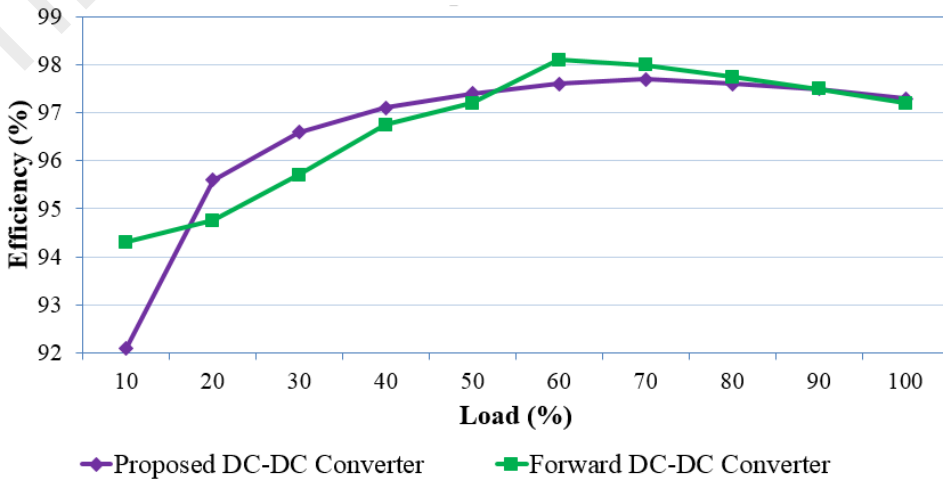

Figure 4.25: Efficiency curve of DC-DC stage of the converter

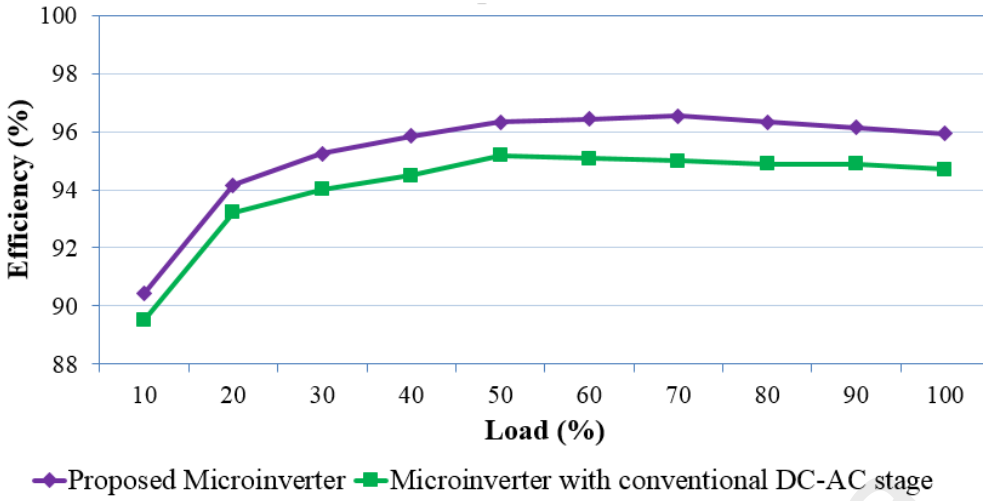

Figure 4.26: Efficiency curve of the overall microinverter

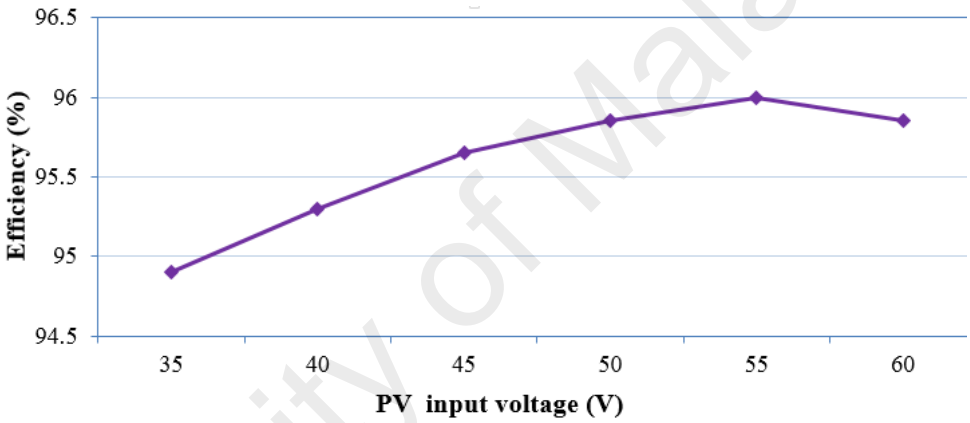

Figure 4.27: Efficiency curve of the microinverter with different PV input voltage

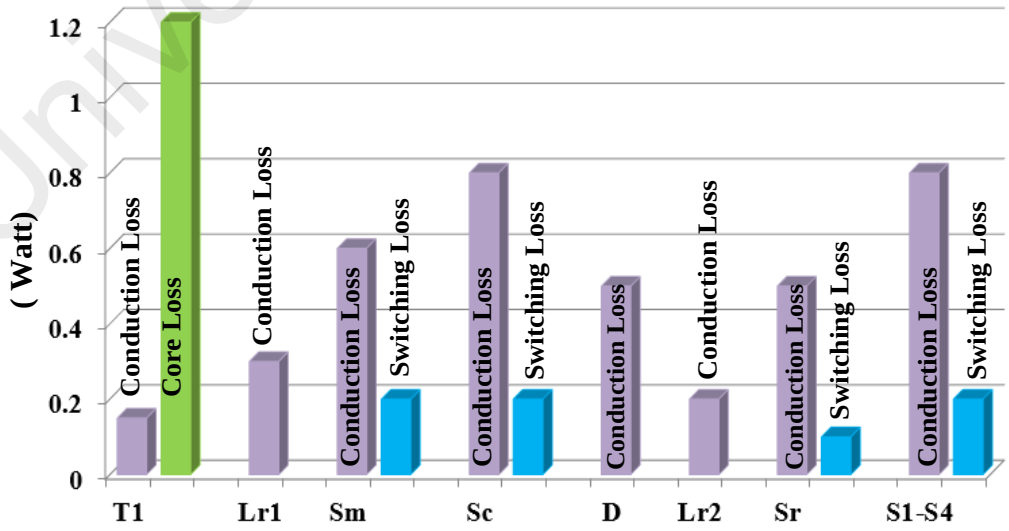

Figure 4.28: Loss-breakdown of main components of the microinverter

4.4 Summary

In this chapter, the results of various sections of the study analyzed earlier in the previous chapters are presented and discussed. Foremost in this chapter is the simulation results of a single-stage active-clamp resonant microinverter. The soft-switching operation in the high frequency switches with the proposed hybrid mode control proves its acceptability from low voltage and current operation of the switches. The effect of the resonant inductor has been presented and compared with the conventional hybrid operation.

In the experimental result, the ZVZCS operation of the proposed single-stage microinverter in different region has been presented and the peak efficiency is found to be 97.1% with a THD of 3.69% for a 250 W prototype. The dynamic response indicates the verification of the hybrid control with the proposed topology. Furthermore, the breakdown of the losses shows the reduction of the switching losses in power semiconductor devices. In case of double-stage microinverter, the DC-DC converter has a peak efficiency of approximately 97.8% and the peak overall efficiency has achieved as 96.5%. Moreover, the proposed topologies show a distinct improvement compare with other topologies, especially in case of low power operation.

CHAPTER 5: CONCLUSION AND FUTURE WORK

5.1 Conclusion

Grid-connected isolated microinverter topology has already been proven as a potential candidate among the different types of PV converter topologies because of providing higher power quality and addressing the safety issues. A variety of research works has been proposed in the recent publications to improve the efficiency, reliability, cost, and compactness. Various types of microinverter topologies and their control techniques has been reviewed in the literature. Among all of these microinverter topologies, the flyback-type power converter has been considered superior in terms of compactness, and cost effectiveness. The switching losses of the flyback converter can be minimized by active-clamp technique and resonant operation. The hybrid operation of DCM and BCM with active clamp technique has been considered as the optimized solution regarding efficiency, cost and compactness.

In spite of having many advantages in conventional hybrid operation with active-clamp flyback converter, the DCM operation cannot attain soft switching properly. Hence, the switching losses occur with the increase of DCM region when the PV power level is decreasing. As a result, the modification of active-clamp technique with control operation is required to minimize the losses in both DCM and BCM region.

In this dissertation, a hybrid operation is proposed to achieve soft switching in single-stage active-clamp flyback type resonant microinverter for the PV AC module. The active-clamp circuit achieves the soft switching by recycling the energy stored in the leakage inductance of the transformer and reduces the voltage stress by clamping the voltage spike across the primary switches. The circuit operation in resonant mode confirms the ZVZCS turn-on of the main switch and ZVS turn-on of the clamp switch. Hence, the proposed microinverter shows much higher level of efficiency and reliability

compared to the conventional flyback topology. The double-stage microinverter operation is performed with an active-clamp resonant flyback DC-DC converter and a resonant full-bridge inverter. The performance of the proposed microinverter topology and control strategy is verified with a simulation in MATLAB Simulink. A 250 W prototype of the microinverter has been implemented to check the validity of the single- and double-stage microinverter.

The most important outcomes of this investigation associated with the hybrid control operation based active-clamp flyback microinverter are as follows:

- The proposed active-clamp flyback microinverter operated in proposed DCMVNC and BCMVNC hybrid operation shows a distinct improvement in reducing the losses and increasing efficiency.
- The single-stage microinverter reaches a peak efficiency up to 97.1% and the California Energy Commission (CEC) efficiency is about 96.7%. The THD of the output current is found to be only 3.69% at a grid frequency of 60 Hz.
- In the double-stage microinverter, the DC-DC converter has a peak efficiency of approximately 97.8%. The peak overall efficiency has achieved as 96.5% and The California Energy Commission (CEC) efficiency is 95.9%. The THD of the output current is measured as 3.71%.

The proposed hybrid operation of the active-clamp flyback topology not only increases the efficiency of the flyback converter but also reduces the cost in single-stage microinverter and improves the lifetime in double-stage microinverter. Hence, the proposed active-clamp center-tapped flyback converter with unfolding bridge and active-clamp DC-DC flyback converter with H-bridge topology are suitable for grid-connected PV application.

5.2 Recommended future research

Although the proposed active-clamp flyback microinverter with hybrid operation for single-stage and double-stage topology meets the research objectives, several issues require further investigation. The suggested recommendations for future work are summarized in the following point:

- The proposed active-clamp flyback microinverter can be interleaved two or more and operated with the developed hybrid mode. This will increase the power level of microinverter with a high efficiency.
- The electrolytic capacitor of the proposed single-stage microinverter can be replaced with a film capacitor using a decoupling circuit. This will increase the cost a little bit but the lifespan of the microinverter will be improved compare to the PV panel.
- The full-bridge inverter of the proposed double-stage microinverter can be replaced with a half bridge inverter with a slight change of control operation. Thus it will appear with a more cost-effective microinverter topology.

REFERENCES

[1] J. Tollefson, "Energy: Islands of light," *Nature,* vol. 507, pp. 154-156, 2014.

[2] R. Detchon and R. Van Leeuwen, "Policy: Bring sustainable energy to the developing world," *Nature,* vol. 508, pp. 309-311, 2014.

[3] D. Lindley, "Smart grids: The energy storage problem," *Nature News,* vol. 463, pp. 18-20, 2010.

[4] Q. Schiermeier, "Renewable power: Germany's energy gamble," *Nature,* vol. 496, pp. 156-158, 2013.

[5] Y. Gogotsi, "Materials science: Energy storage wrapped up," *Nature,* vol. 509, pp. 568-570, 2014.

[6] U.S. Energy Information Administration (EIA), Annual Energy Outlook 2014 (AEO2014) [Online]. Available: http://www.eia.gov

[7] S. B. Kjaer, J. K. Pedersen, and F. Blaabjerg, "A review of single-phase grid-connected inverters for photovoltaic modules," *IEEE Trans Ind Appl,* vol. 41, pp. 1292-1306, 2005.

[8] R. Van Noorden, "Cheap solar cells tempt businesses," *Nature,* vol. 513, pp. 470-470, 2014.

[9] M. C. Beard, J. M. Luther, and A. J. Nozik, "The promise and challenge of nanostructured solar cells," *Nature nanotechnology,* vol. 9, pp. 951-954, 2014.

[10] F. Priolo, T. Gregorkiewicz, M. Galli, and T. F. Krauss, "Silicon nanostructures for photonics and photovoltaics," *Nature nanotechnology,* vol. 9, pp. 19-32, 2014.

[11] M. D. McGehee, "Materials science: fast-track solar cells," *Nature,* vol. 501, pp. 323-325, 2013.

[12] M. Grätzel, "The light and shade of perovskite solar cells," *Nature materials,* vol. 13, pp. 838-842, 2014.

[13] K. Leo, "Perovskite photovoltaics: Signs of stability," *Nature nanotechnology,* vol. 10, pp. 574-575, 2015.

[14] A. El Fathi, L. Nkhaili, A. Bennouna, and A. Outzourhit, "Performance parameters of a standalone PV plant," *Energy Convers Manage,* vol. 86, pp. 490-495, 2014.

[15] K. Himour, K. Ghedamsi, and E. M. Berkouk, "Supervision and control of grid connected PV-Storage systems with the five level diode clamped inverter," *Energy Convers Manage,* vol. 77, pp. 98-107, 2014.

[16] H. Fathabadi, "Two novel techniques for increasing energy efficiency of photovoltaic-battery systems," *Energy Convers Manage,* vol. 105, pp. 149-166, 2015.

[17] S. Kouro, J. I. Leon, D. Vinnikov, and L. G. Franquelo, "Grid-connected photovoltaic systems: An overview of recent research and emerging PV converter technology," *IEEE Ind Electron Magazine,* vol. 9, pp. 47-61, 2015.

[18] M. A. Eltawil and Z. Zhao, "Grid-connected photovoltaic power systems: Technical and potential problems—A review," *Renew Sustain Energy Rev,* vol. 14, pp. 112-129, 2010.

[19] L. Hassaine, E. OLias, J. Quintero, and V. Salas, "Overview of power inverter topologies and control structures for grid connected photovoltaic systems," *Renew Sustain Energy Rev,* vol. 30, pp. 796-807, 2014.

[20] P. Veena, V. Indragandhi, R. Jeyabharath, and V. Subramaniyaswamy, "Review of grid integration schemes for renewable power generation system," *Renew Sustain Energy Rev,* vol. 34, pp. 628-641, 2014.

[21] *Agua Caliente, World's Largest Solar Photovoltaic Plant; U.S. Energy Department [Online]. Available:* http://energy.gov/articles/agua-caliente-worlds-largest-solar-photovoltaic-plant-helps-advance-americas-solar.

[22] N. Altin and İ. Sefa, "dSPACE based adaptive neuro-fuzzy controller of grid interactive inverter," *Energy Convers Manage,* vol. 56, pp. 130-139, 2012.

[23] N. Altin and S. Ozdemir, "Three-phase three-level grid interactive inverter with fuzzy logic based maximum power point tracking controller," *Energy Convers Manage,* vol. 69, pp. 17-26, 2013.

[24] S. Ozdemir, N. Altin, and I. Sefa, "Single stage three level grid interactive MPPT inverter for PV systems," *Energy Convers Manage*, vol. 80, pp. 561-572, 2014.

[25] D. Meneses, F. Blaabjerg, O. Garcia, and J. A. Cobos, "Review and comparison of step-up transformerless topologies for photovoltaic AC-module application," *IEEE Trans Power Electron*, vol. 28, pp. 2649-2663, 2013.

[26] W. Li, Y. Gu, H. Luo, W. Cui, X. He, and C. Xia, "Topology review and derivation methodology of single-phase transformerless photovoltaic inverters for leakage current suppression," *IEEE Trans Ind Electron*, vol. 62, pp. 4537-4551, 2015.

[27] M. Islam, S. Mekhilef, and M. Hasan, "Single phase transformerless inverter topologies for grid-tied photovoltaic system: A review," *Renew Sustain Energy Rev*, vol. 45, pp. 69-86, 2015.

[28] M. Islam and S. Mekhilef, "An improved transformerless grid connected photovoltaic inverter with reduced leakage current," *Energy Convers Manage*, vol. 88, pp. 854-862, 2014.

[29] W.-J. Cha, K.-T. Kim, Y.-W. Cho, S.-H. Lee, and B.-H. Kwon, "Evaluation and analysis of transformerless photovoltaic inverter topology for efficiency improvement and reduction of leakage current," *IET Power Electron*, vol. 8, pp. 255-267, 2015.

[30] Q. Li and P. Wolfs, "A review of the single phase photovoltaic module integrated converter topologies with three different DC link configurations," *IEEE Trans Power Electron*, vol. 23, pp. 1320-1333, 2008.

[31] H. B. Hu, S. Harb, N. Kutkut, I. Batarseh, and Z. J. Shen, "A Review of Power Decoupling Techniques for Microinverters With Three Different Decoupling Capacitor Locations in PV Systems," *IEEE Trans Power Electron*, vol. 28, pp. 2711-2726, Jun 2013.

[32] T. Shimizu, K. Wada, and N. Nakamura, "Flyback-type single-phase utility interactive inverter with power pulsation decoupling on the DC input for an AC photovoltaic module system," *IEEE Trans Power Electron*, vol. 21, pp. 1264-1272, Sep 2006.

[33] H. B. Hu, S. Harb, X. Fang, D. H. Zhang, Q. Zhang, Z. J. Shen, *et al.*, "A Three-port Flyback for PV Microinverter Applications With Power Pulsation

Decoupling Capability," *IEEE Trans Power Electron,* vol. 27, pp. 3953-3964, Sep 2012.

[34] N. Sukesh, M. Pahlevaninezhad, and P. K. Jain, "Analysis and Implementation of a Single-Stage Flyback PV Microinverter With Soft Switching," *IEEE Trans Ind Electron,* vol. 61, pp. 1819-1833, Apr 2014.

[35] G. C. Christidis, A. C. Nanakos, and E. C. Tatakis, "Hybrid Discontinuous/Boundary Conduction Mode of Flyback Microinverter for AC–PV Modules," *IEEE Trans Power Electron,* vol. 31, pp. 4195-4205, 2016.

[36] H. B. Hu, S. Harb, N. H. Kutkut, Z. J. Shen, and I. Batarseh, "A Single-Stage Microinverter Without Using Eletrolytic Capacitors," *IEEE Trans Power Electron,* vol. 28, pp. 2677-2687, Jun 2013.

[37] Z. L. Zhang, X. F. He, and Y. F. Liu, "An Optimal Control Method for Photovoltaic Grid-Tied-Interleaved Flyback Microinverters to Achieve High Efficiency in Wide Load Range," *IEEE Trans Power Electron,* vol. 28, pp. 5074-5087, Nov 2013.

[38] F. F. Edwin, W. Xiao, and V. Khadkikar, "Dynamic modeling and control of interleaved flyback module-integrated converter for PV power applications," *IEEE Trans Ind Electron*, vol. 61, pp. 1377-1388, 2014.

[39] M. Gao, M. Chen, C. Zhang, and Z. Qian, "Analysis and implementation of an improved flyback inverter for photovoltaic AC module applications," *IEEE Trans Power Electron,* vol. 29, pp. 3428-3444, 2014.

[40] Y.-H. Kim, Y.-H. Ji, J.-G. Kim, Y.-C. Jung, and C.-Y. Won, "A new control strategy for improving weighted efficiency in photovoltaic AC module-type interleaved flyback inverters," *IEEE Trans Power Electron,* vol. 28, pp. 2688-2699, 2013.

[41] B.-R. Lin and F.-Y. Hsieh, "Soft-switching zeta-flyback converter with a buck-boost type of active clamp," *IEEE Trans. Ind. Electron.*, vol. 54, pp. 2813-2822, 2007.

[42] W.-J. Cha, J.-M. Kwon, and B.-H. Kwon, "Highly efficient step-up dc–dc converter for photovoltaic micro-inverter," *Soler Energy,* vol. 135, pp. 14-21, 2016.

[43] W. J. Cha, Y. W. Cho, J. M. Kwon, and B. H. Kwon, "Highly Efficient Microinverter With Soft-Switching Step-Up Converter and Single-Switch-Modulation Inverter," *IEEE Trans Ind Electron,* vol. 62, pp. 3516-3523, Jun 2015.

[44] Z. Zhang, M. Chen, W. Chen, C. Jiang, and Z. Qian, "Analysis and implementation of phase synchronization control strategies for bcm interleaved flyback microinverters," *IEEE Trans Power Electron,* vol. 29, pp. 5921-5932, 2014.

[45] M. A. Rezaei, K.-J. Lee, and A. Q. Huang, "A High-Efficiency Flyback Micro-inverter With a New Adaptive Snubber for Photovoltaic Applications," *IEEE Trans Power Electron,* vol. 31, pp. 318-327, 2016.

[46] S.-H. Lee, W.-J. Cha, J.-M. Kwon, and B.-H. Kwon, "Control Strategy of Flyback Microinverter With Hybrid Mode for PV AC Modules," *IEEE Trans Ind Electron,* vol. 63, pp. 995-1002, 2016.

[47] F. L. Alvarado and A. H. Eltimsahy, "Direct Coupling of Solar Cell Arrays to Electric Power Networks," *IEEE Trans Ind Appl,* pp. 90-97, 1976.

[48] G. Campen, "An analysis of the harmonics and power factor effects at a utility intertied photovoltaic system," *IEEE Trans Power Appar Syst,* pp. 4632-4639, 1982.

[49] A. G. Potter, "Analysis of a Series Capacitor-Commutated Inverter Designed to Interface Solar Electric Sources with Electric Power Systems," *IEEE Trans Ind Electron Control Instrument,* vol. 1, pp. 10-16, 1981.

[50] G. T. Chinery and J. M. Wood, "Tva's photovoltaic activities," *IEEE Trans Power Appar Syst,* pp. 1998-2005, 1985.

[51] W. T. Jewell, "Electric utility experience with solar photovoltaic generation," *IEEE Power Eng Rev,* vol. 6, pp. 40-41, 1989.

[52] Y. Bae and R.-Y. Kim, "Suppression of common-mode voltage using a multicentral photovoltaic inverter topology with synchronized PWM," *IEEE Trans Ind Electron,* vol. 61, pp. 4722-4733, 2014.

[53] M. Díez-Mediavilla, M. Dieste-Velasco, M. Rodríguez-Amigo, T. García-Calderón, and C. Alonso-Tristán, "Performance of grid-tied PV facilities based

on real data in Spain: Central inverter versus string system," *Energy Convers Manage*, vol. 86, pp. 1128-1133, 2014.

[54] S. Silvestre, M. A. da Silva, A. Chouder, D. Guasch, and E. Karatepe, "New procedure for fault detection in grid connected PV systems based on the evaluation of current and voltage indicators," *Energy Convers Manage*, vol. 86, pp. 241-249, 2014.

[55] J. Solórzano and M. Egido, "Automatic fault diagnosis in PV systems with distributed MPPT," *Energy Convers Manage*, vol. 76, pp. 925-934, 2013.

[56] H. Keyhani and H. Toliyat, "Single-Stage Multistring PV Inverter With an Isolated High-Frequency Link and Soft-Switching Operation," *IEEE Trans Power Electron*, vol. 29, pp. 3919-3929, 2014.

[57] S. De Haan, H. Oldenkamp, and E. Wildenbeest, "Test results of a 130 W AC module; a modular solar AC power station," in *IEEE First World Conference on Photovoltaic Energy Conversion, Conference Record of the Twenty Fourth. IEEE Photovoltaic Specialists Conference*, 1994, pp. 925-928.

[58] R. H. Wills, F. E. Hall, S. J. Strong, and J. H. Wohlgemuth, "The AC photovoltaic module," in *Conference Record of the Twenty Fifth IEEE Photovoltaic Specialists Conference*, 1996, pp. 1231-1234.

[59] H. P. Ikkurti and S. Saha, "A comprehensive techno-economic review of microinverters for Building Integrated Photovoltaics (BIPV)," *Renew Sustain Energy Rev*, vol. 47, pp. 997-1006, 2015.

[60] *IEEE Standard for Interconnecting Distributed Resources with Electric Power Systems*, IEEE Std.1547, 2008.

[61] *Photovoltaic (PV) systems –Characteristics of the utility interface, IEC 61727*, Second edition, 2004-12.

[62] *US National Electrical Code (NFPA 70)*, National Fire Protection Association, 2014.

[63] *Automatic disconnection device between a generator and the public low-voltage grid*, DIN VDE 0126-1-1 (VDE V 0126-1-1):2013-08.

[64] L. Schwartfeger and D. Santos-Martin, "Review of Distributed Generation Interconnection Standards," in *EEA Conference & Exhibition* Auckland, 2014.

[65] J. Munoz-Cruzado-Alba, J. Villegas-Nunez, J. A. Vite-Frias, J. M. Carrasco-Solis, and E. Galvan-Diez, "New Low Distortion Qf Droop Plus Correlation Anti-Islanding Detection Method for Power Converters in Distributed Generation Systems," *IEEE Trans Ind Electron,* vol. 62, no. 8, pp. 5072-5081, Aug. 2015.

[66] D. Velasco de la Fuente, C. L. Trujillo Rodriguez, and E. A. Narvaez, "Review of Anti-Islanding Methods: Analysis by Figures of Merit Tools for Controllers Reconfiguration in Microgrids," *IEEE Latin America Transactions, (Revista IEEE America Latina),* vol. 13, pp. 679-686, 2015.

[67] S. Raza, H. Mokhlis, H. Arof, J. Laghari, and L. Wang, "Application of signal processing techniques for islanding detection of distributed generation in distribution network: A review," *Energy Convers Manage,* vol. 96, pp. 613-624, 2015.

[68] E. J. Estébanez, V. M. Moreno, A. Pigazo, and M. Liserre, "Performance evaluation of active islanding-detection algorithms in distributed-generation photovoltaic systems: Two inverters case," *IEEE Trans Ind Electron,* vol. 58, pp. 1185-1193, 2011.

[69] X. Guo, D. Xu, and B. Wu, "Overview of anti-islanding US patents for grid-connected inverters," *Renew Sustain Energy Rev,* vol. 40, pp. 311-317, 2014.

[70] L. Chen, C. Hu, Q. Zhang, K. Zhang, and I. Batarseh, "Modeling and Triple-Loop Control of ZVS Grid-Connected DC/AC Converters for Three-Phase Balanced Microinverter Application," *IEEE Trans Power Electron,* vol. 30, pp. 2010-2023, 2015.

[71] A. C. Nanakos, G. C. Christidis, and E. C. Tatakis, "Weighted Efficiency Optimization of Flyback Microinverter Under Improved Boundary Conduction Mode (i-BCM)," *IEEE Trans Power Electron,* vol. 30, pp. 5548-5564, 2015.

[72] M. I. Hamid and A. Jusoh, "Reduction of waveform distortion in grid-injection current from single-phase utility interactive PV-inverter," *Energy Convers Manage,* vol. 85, pp. 212-226, 2014.

[73] A. M. Amjad and Z. Salam, "A review of soft computing methods for harmonics elimination PWM for inverters in renewable energy conversion systems," *Renew Sustain Energy Rev,* vol. 33, pp. 141-153, 2014.

[74] Y. Hoseynpoor and T. P. Ashraf, "Maximum Power Point Tracking and Reactive Power Control of Single Stage Grid Connected Photovoltaic System," *Research Journal of Applied Sciences, Engineering and Technology*, vol. 3, pp. 1430-1436, 2011.

[75] A. Maknouninejad, N. Kutkut, I. Batarseh, and Z. Qu, "Analysis and control of PV inverters operating in VAR mode at night," in *IEEE PES Innovative Smart Grid Technologies (ISGT)*, 2011, pp. 1-5.

[76] R. Kabiri, D. Holmes, and B. P. McGrath, "The influence of PV inverter reactive power injection on grid voltage regulation," in *IEEE 5th International Symposium on Power Electronics for Distributed Generation Systems (PEDG)*, 2014, pp. 1-8.

[77] B. Chen, B. Gu, L. Zhang, Z. U. Zahid, J.-S. J. Lai, Z. Liao, *et al.*, "A High-Efficiency MOSFET Transformerless Inverter for Nonisolated Microinverter Applications," *IEEE Trans Power Electron*, vol. 30, pp. 3610-3622, 2015.

[78] *Types of Solar Inverter Efficiency [Online]. Available:* http://www.solarselections.co.uk/blog/types-of-solar-inverter-efficiency-peak-vs-euro.

[79] A. Mukherjee, M. Pahlevaninezhad, and G. Moschopoulos, "A novel ZVS resonant-type flyback microinverter with regenerative snubber," in *Twenty-Ninth Annual IEEE Applied Power Electronics Conference and Exposition (APEC)*, 2014, pp. 2958-2964.

[80] Q. Zhang, H. Hu, D. Zhang, X. Fang, Z. J. Shen, and I. Bartarseh, "A controlled-type ZVS technique without auxiliary components for the low power DC/AC inverter," *IEEE Trans Power Electron*, vol. 28, pp. 3287-3296, 2013.

[81] A. Amirahmadi, U. Somani, L. Chen, N. Kutkut, and I. Batarseh, "Variable boundary dual mode current modulation scheme for three-phase micro-inverter," in *Twenty-Ninth Annual IEEE Applied Power Electronics Conference and Exposition (APEC)*, 2014, pp. 650-654.

[82] C.-Y. Lin, Y.-C. Liu, J.-S. Lai, and B. Chen, "High-voltage GaN HEMT evaluation in micro-inverter applications," in *IEEE Applied Power Electronics Conference and Exposition (APEC)*, 2015, pp. 2474-2480.

[83] J. W. McLamara and A. Q. Huang, "GaN HEMT based 250W CCM photovoltaic micro-inverter," in *IEEE Applied Power Electronics Conference and Exposition (APEC)*, 2015, pp. 246-253.

[84] S. Tan, P. Lin, C. Hu, L. Chen, and D. Xu, "Interleaved Flyback Micro-inverter with SiC MOSFET," in *International Electronics and Application Conference and Exposition (PEAC)*, 2014, pp. 285-290.

[85] B. N. Pushpakaran, A. S. Subburaj, S. B. Bayne, and J. Mookken, "Impact of silicon carbide semiconductor technology in Photovoltaic Energy System," *Renew Sustain Energy Rev*, vol. 55, pp. 971–989, 2016.

[86] K. Venkatachalam, C. R. Sullivan, T. Abdallah, and H. Tacca, "Accurate prediction of ferrite core loss with nonsinusoidal waveforms using only Steinmetz parameters," in *IEEE Workshop on Computers in Power Electronics*, 2002, pp. 36-41.

[87] D. Meneses, O. Garcia, P. Alou, J. Oliver, R. Prieto, and J. Cobos, "Forward micro-inverter with primary-parallel secondary-series multicore transformer," in *Twenty-Ninth Annual IEEE Applied Power Electronics Conference and Exposition (APEC)*, 2014, pp. 2965-2971.

[88] W. Bower, R. West, and A. Dickerson, "Innovative PV micro-inverter topology eliminates electrolytic capacitors for longer lifetime," in *Conference Record of the IEEE 4th World Conference on Photovoltaic Energy Conversion*, 2006, pp. 2038-2041.

[89] S. Krauter and J. Bendfeld, "Cost, performance, and yield comparison of eight different micro-inverters," in *IEEE 42nd Photovoltaic Specialist Conference (PVSC)*, 2015, pp. 1-4.

[90] S. Poshtkouhi, M. Fard, H. Hussein, L. M. Dos Santos, O. Trescases, M. Varlan, *et al.*, "A dual-active-bridge based bi-directional micro-inverter with integrated short-term Li-Ion ultra-capacitor storage and active power smoothing for modular PV systems," in *Twenty-Ninth Annual IEEE Applied Power Electronics Conference and Exposition (APEC)*, 2014, pp. 643-649.

[91] Y. Ohnuma, K. Orikawa, and J.-i. Itoh, "A Single-Phase Current-Source PV Inverter With Power Decoupling Capability Using an Active Buffer," *IEEE Trans Ind Appl*, vol. 51, pp. 531-538, 2015.

[92] N. Kasa, T. Iida, and L. Chen, "Flyback inverter controlled by sensorless current MPPT for photovoltaic power system," *IEEE Trans Ind Electron,* vol. 52, pp. 1145-1152, 2005.

[93] D. Meneses, O. Garcia, P. Alou, J. Oliver, and J. Cobos, "Grid-Connected Forward Microinverter With Primary-Parallel Secondary-Series Transformer," *IEEE Trans Power Electron,* vol. 30, pp. 4819-4830, 2015.

[94] G. H. Tan, J. Z. Wang, and Y. C. Ji, "Soft-switching flyback inverter with enhanced power decoupling for photovoltaic applications," *IET Electron Power Appl,* vol. 1, pp. 264-274, Mar 2007.

[95] C. Rodriguez and G. A. Amaratunga, "Long-lifetime power inverter for photovoltaic AC modules," *IEEE Trans Ind Electron,* vol. 55, pp. 2593-2601, 2008.

[96] S. Jiang, D. Cao, Y. Li, and F. Z. Peng, "Grid-Connected Boost-Half-Bridge Photovoltaic Microinverter System Using Repetitive Current Control and Maximum Power Point Tracking," *IEEE Trans Power Electron,* vol. 27, pp. 4711-4722, Nov 2012.

[97] H. J. Chiu, Y. K. Lo, C. Y. Yang, S. J. Cheng, C. M. Huang, C. C. Chuang, *et al.*, "A Module-Integrated Isolated Solar Microinverter," *IEEE Trans Ind Electron,* vol. 60, pp. 781-788, Feb 2013.

[98] Y.-H. Kim, S.-C. Shin, J.-H. Lee, Y.-C. Jung, and C.-Y. Won, "Soft-switching current-fed push–pull converter for 250-W AC module applications," *IEEE Trans Power Electron,* vol. 29, pp. 863-872, 2014.

[99] T. LaBella and J.-S. Lai, "A hybrid resonant converter utilizing a bidirectional GaN AC switch for high-efficiency PV applications," *IEEE Trans Ind Electron,* vol. 50, pp. 3468-3475, 2014.

[100] L. Korosec, T. Konjedic, M. Truntic, M. Rodic, and M. Milanovic, "PDM flyback PV microinverter with HFAC-link and active decoupling circuit," *Electronics Letters,* vol. 51, pp. 516-517, 2015.

[101] L. Chen, A. Amirahmadi, Q. Zhang, N. Kutkut, and I. Batarseh, "Design and implementation of three-phase two-stage grid-connected module integrated converter," *IEEE Trans Power Electron,* vol. 29, pp. 3881-3892, 2014.

[102] A. C. Kyritsis, E. C. Tatakis, and N. P. Papanikolaou, "Optimum design of the current-source flyback inverter for decentralized grid-connected photovoltaic systems," *IEEE Trans Energy Conv*, vol. 23, pp. 281-293, Mar 2008.

[103] A. C. Nanakos, E. C. Tatakis, and N. P. Papanikolaou, "A Weighted-Efficiency-Oriented Design Methodology of Flyback Inverter for AC Photovoltaic Modules," *IEEE Trans Power Electron*, vol. 27, pp. 3221-3233, Jul 2012.

[104] Y. L. Li and R. Oruganti, "A Low Cost High Efficiency Inverter for Photovoltaic AC Module Application," *35th IEEE Photovoltaic Specialists Conference*, pp. 2853-2858, 2010.

[105] Y. L. Li and R. Oruganti, "A Low Cost Flyback CCM Inverter for AC Module Application," *IEEE Trans Power Electron*, vol. 27, pp. 1295-1303, Mar 2012.

[106] Y. Li and R. Oruganti, "A low cost flyback CCM inverter for AC module application," *IEEE Trans Power Electron*, vol. 27, pp. 1295-1303, 2012.

[107] A. Amirahmadi, H. Hu, A. Grishina, Q. Zhang, L. Chen, U. Somani, *et al.*, "Hybrid ZVS BCM current controlled three-phase microinverter," *IEEE Trans Power Electron*, vol. 29, pp. 2124-2134, 2014.

LIST OF PUBLICATIONS AND PAPERS PRESENTED

Journal Articles

1. R. Hasan, S. Mekhilef, M. Seyedmahmoudian, and B. Horan, “Grid-connected isolated PV microinverters: A review,” *Renewable and Sustainable Energy Reviews*, vol. 67, pp. 1065-1080, 2017.

2. R. Hasan and S. Mekhilef, "Highly efficient flyback microinverter for grid-connected rooftop PV system," *Solar Energy*, vol. 146, pp. 511-522, 2017.

3. Rasedul Hasan, Saad Mekhilef, “Soft Switching Hybrid-Mode Resonant Flyback Microinverter for Photovoltaic AC Module Applications,” *IEEE Transactions on Industrial Electronics*. *(Status: Yet to Submit)*

Conference Proceedings

1. R. Hasan and S. Mekhilef, "A resonant double stage flyback microinverter for PV applications," in Proceedings of the *IEEE Applied Power Electronics Conference and Exposition (APEC)*, Florida, USA, 2017, pp. 2051-2056.

2. R. Hasan, S. Mekhilef, M. Nakaoka, and K. Nishida, "Soft-switching active-clamp flyback microinverter for PV applications," in Proceedings of the *IEEE Annual Southern Power Electronics Conference (SPEC)*, Auckland, New Zealand, 2016, pp. 1-6.